NAVAL POSTGRADUATE SCHOOL

MONTEREY, CALIFORNIA

THESIS

AMPÈRE'S LONGITUDINAL FORCES REVISITED

by

Alejandro Drago Alfaro

December 2018

Thesis Advisor: Andres Larraza
Co-Advisor: Benjamin T. McGlasson

THIS PAGE INTENTIONALLY LEFT BLANK

REPORT DOCUMENTATION PAGE	*Form Approved OMB No. 0704-0188*

1. AGENCY USE ONLY *(Leave blank)*	**2. REPORT DATE** December 2018	**3. REPORT TYPE AND DATES COVERED** Master's thesis

4. TITLE AND SUBTITLE AMPÈRE'S LONGITUDINAL FORCES REVISITED	**5. FUNDING NUMBERS**
6. AUTHOR(S) Alejandro Drago Alfaro	
7. PERFORMING ORGANIZATION NAME(S) AND ADDRESS(ES) Naval Postgraduate School Monterey, CA 93943-5000	**8. PERFORMING ORGANIZATION REPORT NUMBER**
9. SPONSORING / MONITORING AGENCY NAME(S) AND ADDRESS(ES) N/A	**10. SPONSORING / MONITORING AGENCY REPORT NUMBER**

11. SUPPLEMENTARY NOTES The views expressed in this thesis are those of the author and do not reflect the official policy or position of the Department of Defense or the U.S. Government.

12a. DISTRIBUTION / AVAILABILITY STATEMENT Approved for public release. Distribution is unlimited.	**12b. DISTRIBUTION CODE** A

13. ABSTRACT (maximum 200 words)

Andre-Marie Ampère and Hermann Grassmann each proved the existence of transversal forces in electrodynamics. Nevertheless, even if they coincided on assuming the presence of forces perpendicular to the direction of current flow, only Ampère predicted also a longitudinal component of force. This fundamental disagreement has resulted in a long-lived discussion among many. The purpose of this thesis is to identify the experiments that account for or against the existence of the longitudinal forces in conductors. In order to achieve this, the effects of current on wires subjected to various strain conditions and material characteristics are explored by using COMSOL Multiphysics software. Also, an experimental set-up to get results using the NPS HCTF (High Current Test Fixture) is proposed.

14. SUBJECT TERMS Ampère 's force law, Grassmann's force law, conductors, longitudinal forces	**15. NUMBER OF PAGES** 123
	16. PRICE CODE

17. SECURITY CLASSIFICATION OF REPORT	**18. SECURITY CLASSIFICATION OF THIS PAGE**	**19. SECURITY CLASSIFICATION OF ABSTRACT**	**20. LIMITATION OF ABSTRACT**
Unclassified	Unclassified	Unclassified	UU

NSN 7540-01-280-5500 Standard Form 298 (Rev. 2-89) Prescribed by ANSI Std. 239-18

THIS PAGE INTENTIONALLY LEFT BLANK

Approved for public release. Distribution is unlimited.

AMPÈRE'S LONGITUDINAL FORCES REVISITED

Alejandro Drago Alfaro
Lieutenant Junior Grade, Peruvian Navy
BS, Accademia Navale di Livorno, 2014

Submitted in partial fulfillment of the
requirements for the degree of

MASTER OF SCIENCE IN APPLIED PHYSICS

from the

NAVAL POSTGRADUATE SCHOOL
December 2018

Approved by: Andres Larraza
Advisor

Benjamin T. McGlasson
Co-Advisor

Kevin B. Smith
Chair, Department of Physics

THIS PAGE INTENTIONALLY LEFT BLANK

ABSTRACT

Andre-Marie Ampère and Hermann Grassmann each proved the existence of transversal forces in electrodynamics. Nevertheless, even if they coincided on assuming the presence of forces perpendicular to the direction of current flow, only Ampère predicted also a longitudinal component of force. This fundamental disagreement has resulted in a long-lived discussion among many. The purpose of this thesis is to identify the experiments that account for or against the existence of the longitudinal forces in conductors. In order to achieve this, the effects of current on wires subjected to various strain conditions and material characteristics are explored by using COMSOL Multiphysics software. Also, an experimental set-up to get results using the NPS HCTF (High Current Test Fixture) is proposed.

THIS PAGE INTENTIONALLY LEFT BLANK

TABLE OF CONTENTS

LIST OF FIGURES

LIST OF TABLES

THIS PAGE INTENTIONALLY LEFT BLANK

ACKNOWLEDGMENTS

I would like to thank my advisor, Professor Andres Larraza, and my co-advisor, Benjamin T. McGlasson, for their patience and guidance throughout this journey. This thesis research would not have been possible without them. Also, I would like to express my gratitude to all the professors and staff of the NPS Physics department for their amazing support during these two years.

I would like to thank the Peruvian Navy for giving me the opportunity to study in this master's program. Lastly, thanks to my beloved ones, family and friends, who always supported me and gave me strength to go through this challenge.

THIS PAGE INTENTIONALLY LEFT BLANK

I. INTRODUCTION

The scientific community is characterized by its relentless search for solutions to unanswered questions. It is the intrinsic human hunger for knowledge that leads researchers and academics to invest a considerable amount of time on theoretical and experimental inquiry. Yet, sometimes the path between the theoretical proposal and the experimental results can create divisions inside the academic world. In some cases, some questions do not get a final answer, or the answers simply do not fulfill the expectations of the scientific community. In other cases, there is more than one answer for the same question, dividing the community into two or more factions.

This last case is the main subject of this thesis. The scientists Andre-Marie Ampère and Hermann Grassmann proved the existence of transversal forces in electrodynamics. Nevertheless, although they both concurred on assuming the presence of forces perpendicular to the direction of current flow, only Ampère predicted a longitudinal component of force as well. This debate has been in the eye of the storm for more than a century. The scientific community ultimately took the side of Grassmann, not only because the existence of longitudinal forces has never been convincingly demonstrated, but also because the celebrated Maxwell's equations for electromagnetic fields came to light using Grassmann's force law.

Since then, many scientists have tried to "row upstream" by working on experimental processes capable of demonstrating in the field the existence of Ampère's longitudinal forces. While results have been interesting in some cases, they have been inconclusive, and the debate is still ongoing.

Modeling some of these experiments using COMSOL can help clarify the nature of the observations and provide arguments that will advance the understanding of the forces due to current. In order to successfully complete this experimentation process, however, it is necessary to understand both theories. It is also necessary to compare these two different mathematical processes and understand the two different physical results.

THIS PAGE INTENTIONALLY LEFT BLANK

II. BACKGROUND

A. AMPÈRE'S FORCE LAW

Scientists achieved significant theoretical and experimental improvement with respect to magnetism and electricity during the 18th and the beginning of the 19th century. Specifically, in 1820, Hans Christian Oersted demonstrated for the first time that these two important physics phenomena, which previously were treated independently, were in fact related to each other (Nicolaide, 2012).

After Oersted's discovery was announced at the French Academy meeting that same year, many scientists started to analyze it. Two Frenchmen, Jean-Baptiste Biot and Felix Savart, reached the first precise conclusion on this matter. They announced that a magnetic pole, located at a point N from a thin slice of an infinitely long conductor carrying a current, would experience a force perpendicular to the plane formed by both the conductor and the point N. Also, its intensity would be inversely proportional to the distance r between them (Blondel & Wolff, 2009b; Whittaker, 1951).

In this context, Ampère started to search for a law that would express the relationship between two different currents. He proposed a very elemental hypothesis, dividing the original current in infinitesimal current elements and studying the interactions between them. In order to do so, he adopted a Newtonian approach, by which every current element would exert an elementary force that had to obey the principle of action and reaction. This assumption supposes also that both current element forces have to be directed on a straight line between them (Blondel & Wolff, 2009b).

After working on his initial set of experiments, Ampère drew some valuable conclusions from observations never made before in this area of study. According to Assis and Chaib (2015), and Whittaker (1951), the most relevant were:

> "The effect of current is reversed when the direction of the current is reversed" (Whittaker, 1951, p. 89);

There is an attraction or repulsion force between two currents carrying parallel conductors;

"Torque [is] exerted by a current-carrying loop and acting on another current-carrying loop" (Assis & Chaib, 2015, p. 72);

A closed circuit A exerts a force on an element of another circuit B. This force is perpendicular to circuit B.

Relying on his results and making some mathematical assumptions, Ampère elaborated a law that described the interaction between two current elements. This way, if somebody wanted to know the total force on one of the electric circuits, it would be possible to sum the contributions of all the current elements (Johansson, 1996).

In 1822, Ampère came up with a final expression for the force between current elements

$$\frac{ii\prime dsds\prime}{r^n}[\cos\alpha\cos\beta\cos\gamma - k\cos\alpha\cos\beta]. \quad (1)$$

Later, in 1826, he updated it as

$$\frac{ii\prime dsds\prime}{r^n}[\cos\varepsilon + h\cos\theta\cos\theta']. \quad (2)$$

For Equations (1) and (2), $n = 2$, $k = -\frac{1}{2}$, and $h = k - 1 = -\frac{3}{2}$, are constants, for which values were obtained empirically. Also, α, β, γ, ε, θ and θ' are the angles (variables) used by Ampère (Ampère, 1826).

Equation (1) underwent a notation change in the following years, as the world adopted different ways to express physical values, especially with the adoption of vector analysis and SI Units notation. Ampère's equation is expressed nowadays as

$$d\vec{F}_{Amp} = \frac{\mu_0 I_1 I_2}{4\pi r_{12}^2}[3(d\vec{l_1}.\hat{r}_{12})(d\vec{l_2}.\hat{r}_{12}) - 2(d\vec{l_1}.d\vec{l_2})]\hat{r}_{12}. \quad (3)$$

For further information about the change of notation between equations (2) and (3), see Appendix A.

As Johansson describes in his work (1996), Equation (3) defines the interaction between current elements $d\overrightarrow{l_1}$ and $d\overrightarrow{l_2}$. More specifically, it calculates the force $d\vec{F}$ that $d\overrightarrow{l_1}$ exerts on $d\overrightarrow{l_2}$. This force depends on constants such as the magnetic permeability μ_0, and on variables such as the electric currents in the circuits 1 and 2 (I_1 and I_2). Another variable is the distance r_{12} between both current elements. Finally, $\hat{r}_{12}$ is the unit vector in the direction between the elements $d\overrightarrow{l_1}$ to $d\overrightarrow{l_2}$. (See Figure 1.)

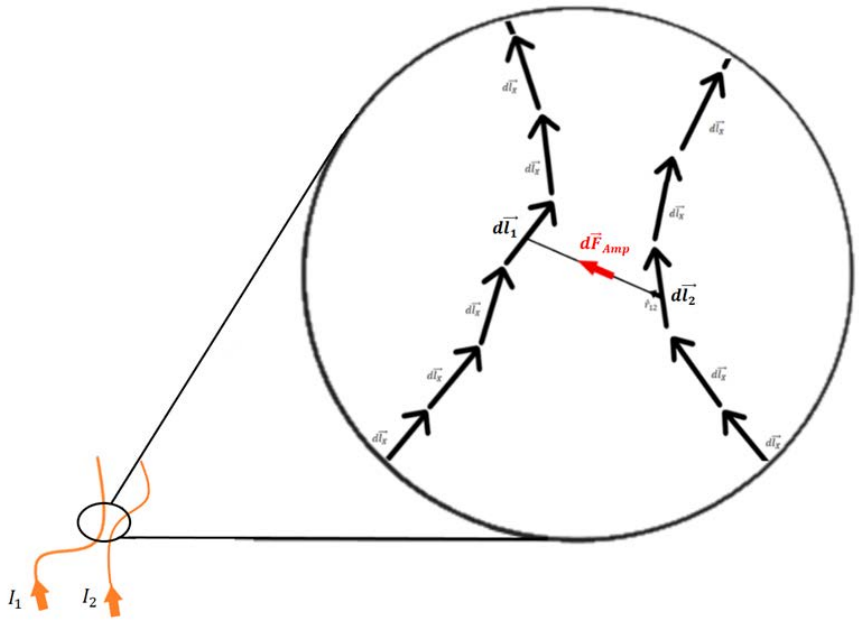

Figure 1. Ampère's force between two current elements on different circuits

This formula was able to predict the force between two current elements. Nonetheless, because of the assumption that these forces are not only equal and opposite but also directed in a straight line between them, it predicts a very controversial longitudinal force between current elements on the same circuit.

B. GRASSMANN'S FORCE LAW

In the years following Ampère's presentation of his work to the world, many scientists remained dubious about it, from both a physical and a mathematical point of

view. Oersted, Biot and Savart, and Faraday had their own objections to Ampère's electromagnetic interpretation (Assis & Chaib, 2015). Yet as Assis and Chaib (2015) describe in their work, the German mathematician Hermann Grassmann published a paper in 1845, where he established a new formula to calculate the force between two current elements as

$$d\vec{F}_{Grass} = id\vec{s} \times \frac{ki_\prime d\vec{s}_\prime \times \hat{r}}{r^2}. \quad (4)$$

It can be expressed in SI units,

$$d\vec{F}_{Grass} = \frac{\mu_0 I_1 I_2}{4\pi r_{12}^2}[d\overrightarrow{l_2} \times (d\overrightarrow{l_1} \times \hat{r}_{12})], \quad (5)$$

as Johansson (1996) did, or rewritten as

$$d\vec{F}_{Grass} = \frac{\mu_0 I_1 I_2}{4\pi r_{12}^2}[(d\overrightarrow{l_2}.\hat{r}_{12})d\overrightarrow{l_1} - (d\overrightarrow{l_1}.d\overrightarrow{l_2})\hat{r}_{12}]. \quad (6)$$

Similarly to what happens with Ampère's law, Equation (6) describes the force $d\vec{F}_{Grass}$ that current element $d\overrightarrow{l_1}$ exerts on current element $d\overrightarrow{l_2}$. Also, $\hat{r}_{12}$ is the unit vector in the direction from $d\overrightarrow{l_1}$ to $d\overrightarrow{l_2}$, with r_{12} being the distance between these two current elements. Again, I_1 and I_2 are the currents' values expressed in Ampère's.

Grassmann was a German high school mathematics teacher who never taught at a university. He did not have higher-level education in physics or mathematics. Despite that, in 1844, he published a book (with a second and more complete version published in 1862) where he developed a new and important mathematical theory. Grassmann defined, for the first time, the modern scalar and vector products, which he then used as the basis of his electrodynamics statements (Assis, 1994).

Grassmann observed two particular problems in Ampère's force law. The first one was that attraction and repulsion were arbitrary assumptions. With this in mind, he raised the fact that current elements, having both magnitude and direction, were actually vectors (Graneau & Graneau, 1996). Therefore, there was no valid reason to assume they had to behave as gravitating and charged particles, which are scalar quantities (Tricker, 1962).

The second statement that concerned Grassmann about Ampère's force law, and about which he was suspicious, was that "electric currents react on each other as if each element of one circuit reacted with each element of the other according to certain rule" (Tricker, 1962, p. 462).

Basically, as shown in Figure 2, a current element $d\vec{l_1}$ is fixed at the center while a second current element $d\vec{l_2}$ rotates around it, holding always its original orientation (parallel to itself). Distance r is held constant, and the arrows around the circle represent the force that $d\vec{l_1}$ exerts on $d\vec{l_2}$. It can be seen that, for each quadrant, there exists an angular position by which the force goes to zero and oscillates between attraction and repulsion. According to Graneau and Graneau (1996), however, it was the behavior of Ampère's force at the cardinal points that aroused suspicions in Grassmann. When $d\vec{l_2}$ is placed at α = 90° or 270° from $d\vec{l_1}$, the force takes two units of force of arbitrary magnitude. On the other hand, when $d\vec{l_2}$ is located at α = 0° or 180° from $d\vec{l_1}$, the force takes just one arbitrary unit of force of magnitude. As Graneau and Graneau conclude, "Grassmann did not like this unexpected variation of the elemental force with angular position, but was unable to provide an argument which proved Ampère's force law to be wrong" (p. 32).

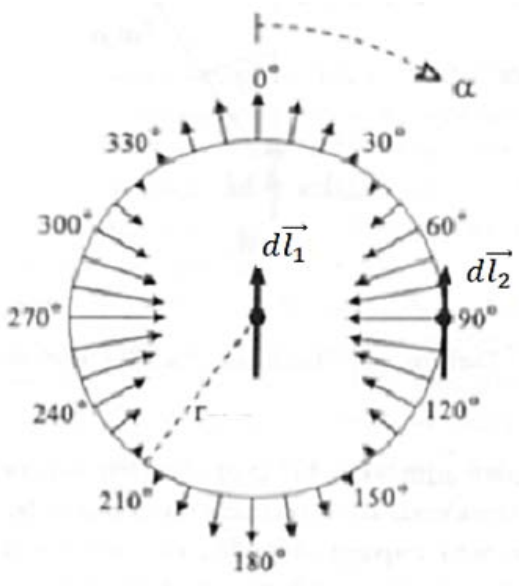

Figure 2. Ampère's force between two parallel elements at constant distance. Adapted from Graneau and Graneau (1996).

C. CONTROVERSY ARISING FROM THE TWO THEORIES

The "crucial point of controversy" as described by Cavalleri (1996, p. 205), is that Ampère's force law stated in Equation (1) obeys Newton's third law, while Grassmann's force law in Equation (4) does not. (See Figure 3.)

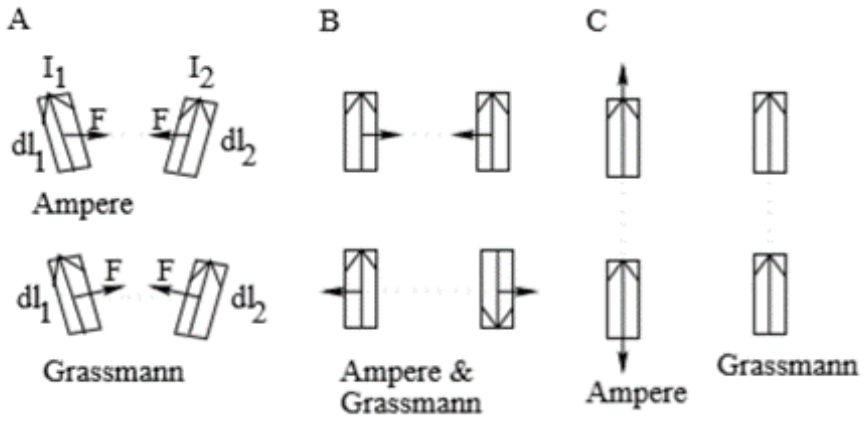

(A) Forces between current elements. (B) Transverse forces between parallel elements. (C) Longitudinal forces between co-linear elements.

Figure 3. Ampère's and Grassmann's force differences. Adapted from Johansson (1996).

From Figure 3 it is possible to see the difference between these two laws in terms of Newton's third law, also known as the action and reaction principle. This law can be used to analyze the interaction between two particles (Taylor, 2005). Accordingly, if one object exerts a force A on another object B, then object B will "react," exerting the same amount of force back onto object A. One important factor is that the "reaction" force has to be equal and opposite to the "action" force. According to Taylor (2005), if the action and reaction force act along the imaginary line that connects both particles, these are called "central forces." By contrast, "the third law does not actually require that the forces be central" (p. 18). This last statement means that it is possible to satisfy Newton's third law even if the forces are not directed in the same line.

Also, when central forces are applied, some authors such as Assis and Chaib (2015), call the action and reaction principle "the strong form of Newton's third law." If not, it is called "the weak form of Newton's third law."

Figure 3 shows that Ampère's force always follows the strong form of Newton's third law, meaning that it is directed along the imaginary line that connects both current elements. Conversely, in most of the cases, Grassmann's force does not. Therefore, $d\vec{F}_{Grass}$ exerted by current element $d\overrightarrow{l_1}$ on current element $d\overrightarrow{l_2}$ will not be equal and opposite to the force that $d\overrightarrow{l_2}$ exerts on $d\overrightarrow{l_1}$. Still, even if most of the time Grassmann's force is not a central force, "in some particular configurations it will follow the principle of action and reaction in the weak form" (Assis & Chaib, 2015, p. 219).

From a mathematical point of view, if $\hat{r}_{12}$ is used on $d\vec{F}_{Amp}$, and $\hat{r}_{21}$ is used on $d\vec{F}'_{Amp}$, then

$$d\vec{F}_{Amp} = -d\vec{F}'_{Amp} \tag{7}$$

and this will be true always.

On the other hand, if the same assumption is given for $d\vec{F}_{Grass}$ and $d\vec{F}'_{Grass}$, the action and reaction principle will be violated due to the fact that $d\vec{F}_{Grass}$ is often different from $-d\vec{F}'_{Grass}$. Only in some special cases, Grassmann's force law will actually satisfy this principle.

Cornille (1989) supports this statement mathematically as follows. Knowing that

$$d\overrightarrow{l_2} \times \left(d\overrightarrow{l_1} \times \hat{r}_{12}\right) = \left(d\overrightarrow{l_2}.\hat{r}_{12}\right)d\overrightarrow{l_1} - (d\overrightarrow{l_2}.d\overrightarrow{l_1})\hat{r}_{12}, \tag{8}$$

and

$$d\overrightarrow{l_1} \times \left(d\overrightarrow{l_2} \times \hat{r}_{21}\right) = \left(d\overrightarrow{l_1}.\hat{r}_{21}\right)d\overrightarrow{l_2} - (d\overrightarrow{l_1}.d\overrightarrow{l_2})\hat{r}_{21}, \tag{9}$$

if, as seen in Equations (8) and (9), $d\overrightarrow{l_1}$ and $d\overrightarrow{l_2}$ change positions, the results will change. This makes these equations non-symmetric and, by definition, $d\vec{F}_{Grass}$ and $-d\vec{F}'_{Grass}$ will not be the same under the conditions presented before.

Figures 4 and 5 show two cases where a graphical explanation of this main difference between the two formulas can be made. This explanation also gives a more practical description of what it actually means to obey or violate Newton's action and reaction principle.

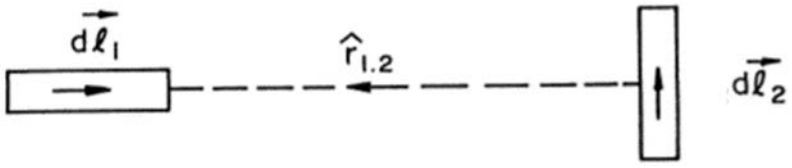

Figure 4. Two current elements perpendicular to each other. Adapted from Assis (1994).

Figure 4, as explained by Assis (1994), shows two different current elements that are perpendicular to each other. Applying both Ampère's and Grassmann's formula to this particular case will yield different results. For Ampère's force law, $\hat{r}_{12}$ is used on $d\vec{F}_{Amp}$ and $\hat{r}_{21}$ is used on $d\vec{F}'_{Amp}$

$$d\vec{F}_{Amp} = d\vec{F}'_{Amp} = 0. \tag{10}$$

For Grassmann's force law, $\hat{r}_{12}$ is used on dF_{Grass} , and $\hat{r}_{21}$ is used on dF'_{Grass}, so

$$d\vec{F}_{Grass} = 0, \tag{11}$$

and

$$d\vec{F}'_{Grass} = \frac{\mu_0 I_1 I_2}{4\pi r_{12}^2} d\overrightarrow{l_1} d\overrightarrow{l_2}. \tag{12}$$

As is evident, when current element $d\overrightarrow{l_2}$ exerts a force on current element $d\overrightarrow{l_1}$, Grassmann's law gives a force different from zero. This means that Newton's third law does not seem to apply, not even in its weak form.

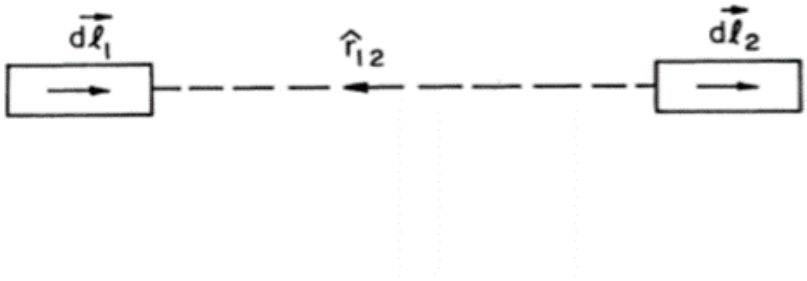

Figure 5. Two current elements parallel and collinear to each other. Adapted from Assis (1994).

In the same way, Figure 5 shows two different current elements that are parallel and collinear to each other. If both Ampère's and Grassmann's force laws are applied to this particular case, and under the same conditions stated before (Ampère's force law: $\hat{r}_{12}$ is used on dF_{Amp} and $\hat{r}_{21}$ is used on dF'_{Amp}; Grassmann's force law: $\hat{r}_{12}$ is used on dF_{Grass}, and $\hat{r}_{21}$ is used on dF'_{Grass}), the respective results will be

$$d\vec{F}_{Amp} = \frac{\mu_0 I_1 I_2}{4\pi r_{12}^2} d\overrightarrow{l_1} d\overrightarrow{l_2} = -d\vec{F}'_{Amp}, \tag{13}$$

and

$$d\vec{F}_{Grass} = 0 = d\vec{F}'_{Grass}. \tag{14}$$

As can be seen in Equation (14), in this particular case, Grassmann's force law will follow Newton's third law, such that the net force in both cases is zero. On the other hand, Equation (13) shows Ampère's force law results. Once again, the action and reaction principle is followed. However, in this case, the result is a repulsive force between parallel and collinear current elements. This result is at the center of this thesis, because it explains why Ampère's force law predicts a longitudinal force, while Grassmann's force law does not (Assis, 1994).

It is important to note where the controversy is specifically pointing. In his analysis of the discussion about which formula was the correct one, Johansson (1996) affirms that,

when integrated around a circuit, “both formulas yielded the same result: Neumann force law for two circuits” (p. 3), as shown in Equation (15).

$$d\vec{F}_{Neum} = -\frac{\mu_0 I_1 I_2}{4\pi} \oint\oint \frac{d\vec{l_1} d\vec{l_2}}{r_{12}^2} \hat{r}_{12} \tag{15}$$

This brings the discussion to only one case: the force generated between two parts of the same circuit. In other words, the force produced by current elements of the same circuit.

During the years that followed Ampère’s force law presentation, some physicists like Weber, Hering, and Neumann developed an electrodynamic theory based on it. Weber created a whole new method to study electromagnetic phenomena based on elementary forces among electric charges. His theory was based on three different terms based on one charge’s acceleration, velocity, and distance with respect to another charge. One of these terms would eventually become Coulomb’s law, while the other two would take into account induction and Ampère’s formula. Many scientists believe in Weber’s electrodynamics as a valid substitute for Maxwell’s construction, among which the most renowned are Assis (Weber’s electrodynamics) and Graneau (Newtonian electrodynamics) (Blondel and Wolff, 2009a).

Nevertheless, as Blondel and Wolff (2009a) describe in their work, after the Lorentz force was defined, and Maxwell's theory came to light, Ampère’s force law disappeared from the books. This happened mainly because Grassmann’s force law “fits perfectly into the Maxwellian framework” (Blondel & Wolff, 2009a). This last statement can be easily observed in Appendix B of this work, where it is demonstrated how Grassmann’s law can be derived directly from Lorentz’s force law and the Biot-Savart law.

Finally, even Graneau (1987) accepted the fact that Lorentz force has worked efficiently in explaining many different physics phenomena to which Ampère’s theory does not apply, such as electron beams, charges convecting in vacuum or dielectric fluids. Further discussion on this topic will be elaborated in the next chapters.

III. POSSIBLE EXPERIMENTAL SUPPORT OF LONGITUDINAL FORCES

In this chapter we provide a description of several experiments that seem to support Ampère's longitudinal forces and the physical arguments that refute this conclusion. To clear the controversy, scientists have conducted many experiments to prove or disprove the existence of longitudinal forces. The results of these experiments have been discussed by different scientists, and various theories about the outcome of these experiments have been made.

A. EXPERIMENTS THAT SEEMINGLY SUPPORT AMPÈRE'S TENSION

The following are the most important experiments created by Ampère and other scientists over the last two centuries attempting to prove Ampère's force law formula.

In this context it is important to name two main contributors to the study of this controversy, Peter Graneau and Polish scientist Jan Nasilowski. Their work revived the discussion on Ampère's longitudinal forces.

1. Ampère's Hairpin Experiment

With the aim to demonstrate the validity of his formula and the existence of longitudinal forces, Ampère elaborated an experiment commonly known as the hairpin experiment, using floating conductors (Blondel & Wolff, 2009b).

As shown in Figure 6, a circular receptacle was filled with liquid mercury. This receptacle was divided into two independent compartments by an insulated partition; each of these compartments had a conducting cable submerged in the mercury on one side and attached to an external battery on the other side. A metal wire in the form of a hairpin and insulated all over, except for the bare ends A and E, floats with one branch on each side of the receptacle.

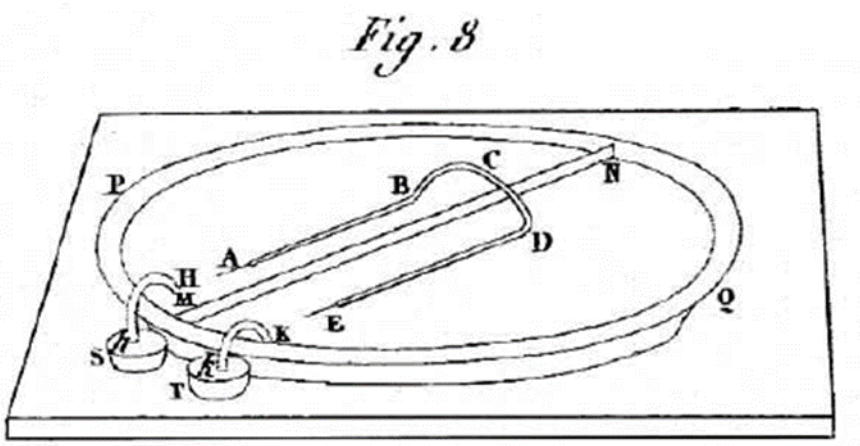

Figure 6. The floating conductor experiment (hairpin experiment).
Source: Assis and Chaib (2015).

By applying a current from the battery through H and K, two currents will be established in the mercury at the same time.

> Whatever the direction of the current, you can always see the two wires AB and ED moving parallel to the barrier MN, away from the points H and K, which indicates a repulsion for each wire between the current established in the mercury and its extension in the wire itself. (Ampère, 1826, p. 211–212)

This, in Ampère's conclusion, proved the existence of longitudinal forces in conductors.

Other scientists have repeated this experiment over the years. Figure 7 shows Blondel's version of the experiment, which obtained the same outcome. Graneau and Graneau (1996), elaborated a new version of Ampère's hairpin obtaining the same result. Additionally, they observed that when the hairpin motion was purposely obstructed by any object "strong jets of liquid mercury could be seen to emanate from the hairpin ends [A and E in Figure 6]" (Graneau & Graneau, 1996, p. 62).

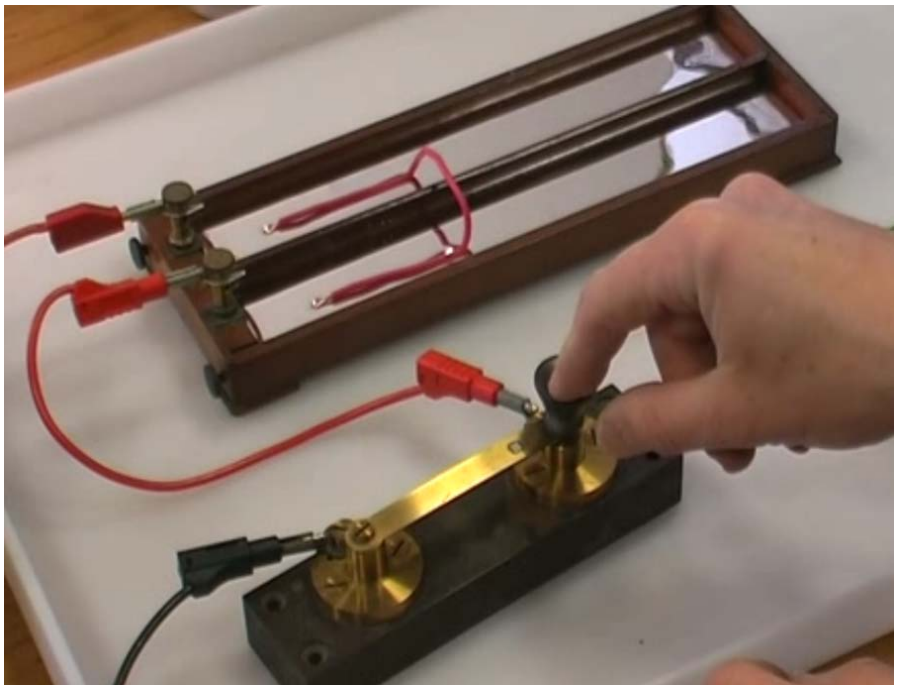

Figure 7. Blondel's version of Ampère's hairpin experiment. Source: Blondel and Wolff (2009a).

On the other hand, many contradictory interpretations have been made about this experiment. "In fact, the different variations of Ampère's hairpin experiment are interpreted in the context of modern physics by using the Laplace force, and therefore the elemental force of Grassmann" (Blondel & Wolff, 2009a). There is a striking resemblance between the current path in this experiment and the current path of an electromagnetic railgun. The location where the wire crosses over the insulating divider between the two pools would be called the armature in the railgun circuit. The armature is the part that slides along the barrel and pushes the projectile up to high speed. There should be a similar "launch force" in the hairpin crossover, which Ampere may not have appreciated. The observation of liquid mercury jetting by Graneau and Graneau, though, is still a mystery.

2. Other Liquid Conductor Experiments

Other similar experiments were developed using liquid metals. A long and narrow container with copper bars at the ends was filled with mercury and a current of hundreds of Amperes was passed through the liquid metal. The outcome was the creation of waves

on the mercury that pushed the mercury away from the copper and into the center of the trough (Johansson, 1996).

This phenomenon was repeated in another experiment carried out by Graneau and Graneau in Massachusetts Institute of Technology's (MIT) laboratory, called “The liquid mercury fountain.” As described by the authors (1996), this time a copper ring electrode was partly flooded on a dielectric cup filled with mercury. From the bottom of the cup, a conductor made of copper would get excited with a 500–1000 A DC current. The current would flow between the rod and the copper ring ends. As shown in Figure 8, mercury would get pushed straight up from the cup forming a “conical fountain head on the free surface of the liquid metal” (p. 78). At the same time, mercury would stream down the perimeter of the cone. Finally, as long as the current continued to flow, the mercury circulation movement remained constant.

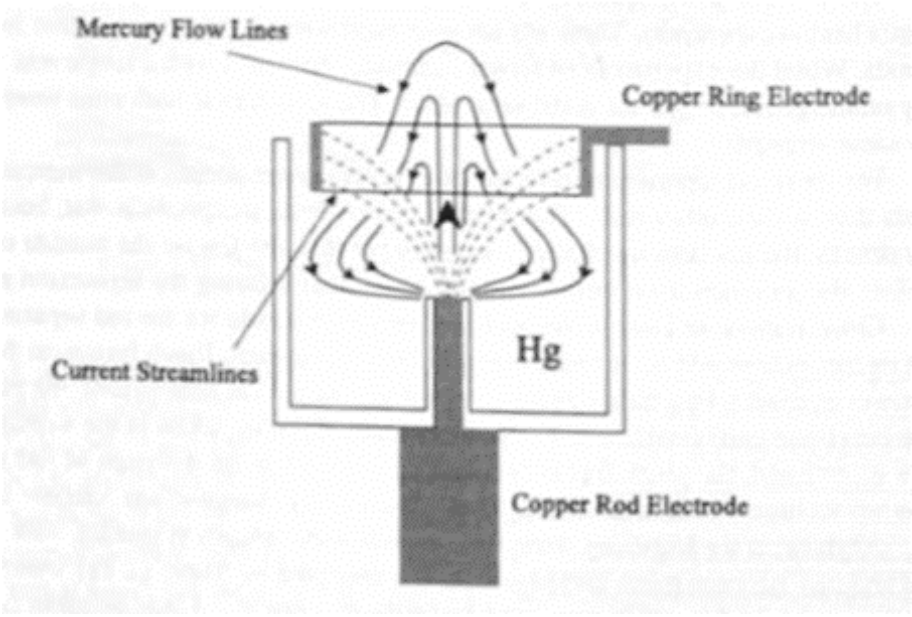

Figure 8. Graneau’s liquid mercury fountain.
Source: Graneau and Graneau (1996).

Once again, many different opinions have been raised about the liquid conductor experiments, and the debate is still open. One explanation is that Lorentz force is highest near the copper rod electrode and pointed mostly upward. This pushes the mercury up with

higher force than occurs near the copper ring electrode, resulting in the “fountain” circulation pattern seen in the experiment.

3. Nasilowski’s Wire Fragmentation

An important breakthrough occurred when Polish scientist Jan Nasilowski performed an experiment on longitudinal forces, for the first time, without using liquid metal in 1964. As Graneau and Graneau (1996) describe in their book, Nasilowski was conducting experiments to study the performance of copper fuse wires when exposed to a quick and strong current pulse. Nasilowski’s wires were 1.5 meter (m) long and had a diameter of 1 mm. The current applied to the wires had an amplitude of 2000 A and a duration of up to 50 ms, which is relatively long. The experiment’s setup consisted of a simple circuit that connected a DC generator to a wire in a closed short circuit. The outcome of the experiment was the fragmentation of the wire into about 100 pieces with varying lengths between 0.3 cm to 3 cm (Graneau, 1984b). (See Figure 9.)

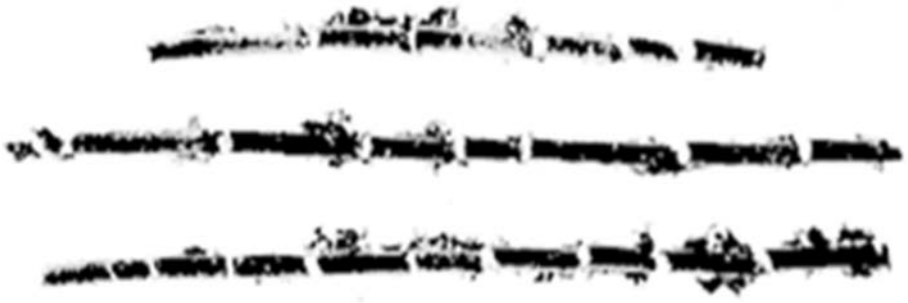

Figure 9. Nasilowski’s wire fragmentation. Source: Nasilowski (1964).

When fractures occurred, the current continued to flow because of the formation of electric arcs through the air between the pieces, as shown in Figure 10.

Graneau and Graneau (1996) explain Nasilowski’s results on the wire fragments through metallurgical examinations. The disintegration of the wires occurred in the solid state. Also, the results showed that the wire fragments had suffered brittle fractures with propagation direction perpendicular to the wire axis, as shown in Figure 11. These two

conditions, in Graneau and Granueau's (1996) opinion, proved the fact that the rupture was due to tensile forces.

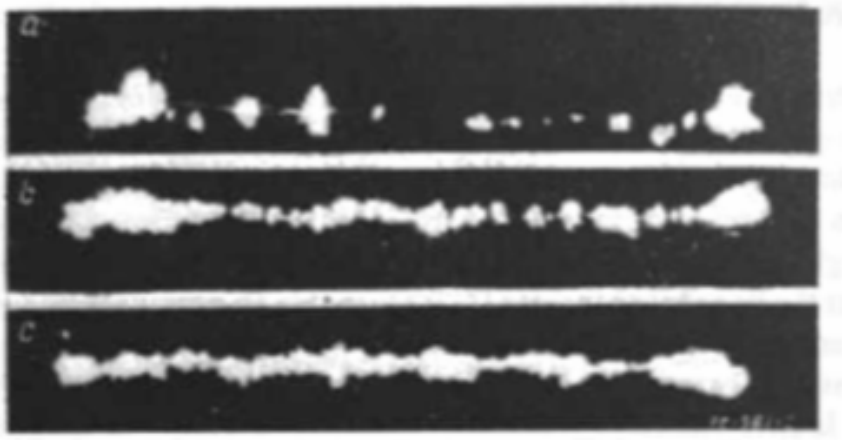

Figure 10. Electric arcs in Nasilowski's experiment. Source: Nasilowski (1964).

Additionally, after sectioning the wire along its longitudinal axis, further microscopic evidence was taken by Nasilowski, showing that the wire presented some transverse cracks that would have caused more fragments if the current would have continued. Finally, microscopic analysis of the cracks showed that "atomic bonds had ruptured in tension before melting had taken place" (Graneau & Graneau, 1996, p. 52).

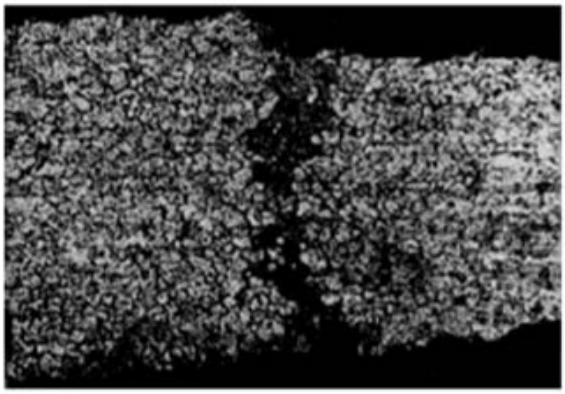

Figure 11. Fractures due to tensile forces. Source: Nasilowski (1964).

4. Graneau's Follow-Up Experiments

In 1982, Graneau and Graneau repeated, in more than one modified version, Nasilowski's experiment at MIT. First, they modified the original straight wire fragmentation experiment. This time, they used a current of magnitudes of 5000 to 7000 A and a period that varied from five milliseconds to ten milliseconds. The wires were made of 99 percent aluminum and had a diameter of 1.2 mm. While in Nasilowski's experiment the wires' ends were firmly fixed to a frame at the laboratory (Molokov & Allen, 1997), Graneau and Graneau (1996) performed their own tests with the wires separated 1 cm from the terminations of the circuit that would eventually discharge the current through the wire, as shown in Figure 12. As explained in their book, "the purpose of the arc gaps was to allow distortion free thermal expansion of the wire and mechanical decoupling from the rest of the circuit" (p. 53).

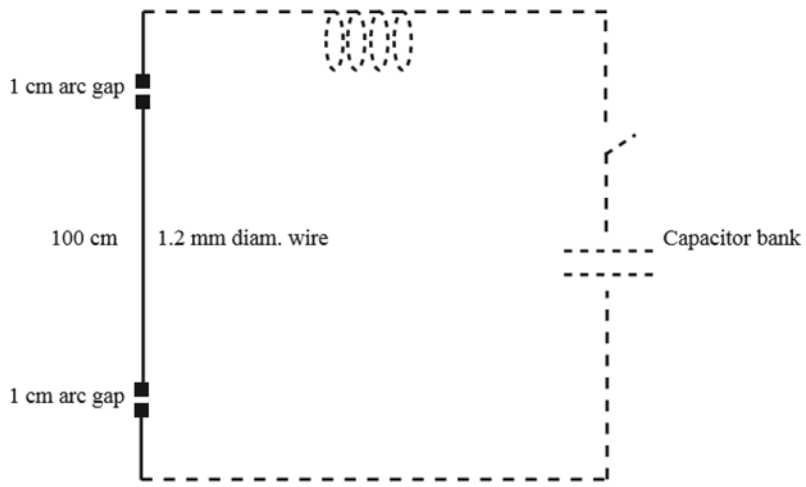

Figure 12. Straight wire fragmentation experiment setup

A 60 kV discharge was distributed along the wire. Several hundreds of Celsius degrees of temperature increase were measured along the aluminum wire, causing a 1 percent thermal expansion of the wire. Electrical potential was increased in steps of 2 kV

each time, until the wire broke into two or more fragments. Finally, at 68 kV, the wire broke into more than 20 pieces (Graneau & Graneau, 1996).

On a second version of his experiment, Graneau (1984b) decided to bend the wire in a semicircular shape. This was done in order to "determine if longitudinal forces might be found in magnet windings" (p. 2598). As shown in Figure 13, the wire was suspended vertically forming a 25 cm radius semicircle. The 1 cm air gaps were maintained for the same reasons explained before. The wire was initially acted with 50 kV of electric potential. This wire suffered an increase in its temperature, but it did not break. After the wire returned to room temperature, the same procedure was repeated. Every time, the electrical potential was increased by 2kV, and the outcome was the same. The wire finally broke into three pieces at 62 kV and 6000 A (Graneau, 1984b). Different wires were subsequently used.

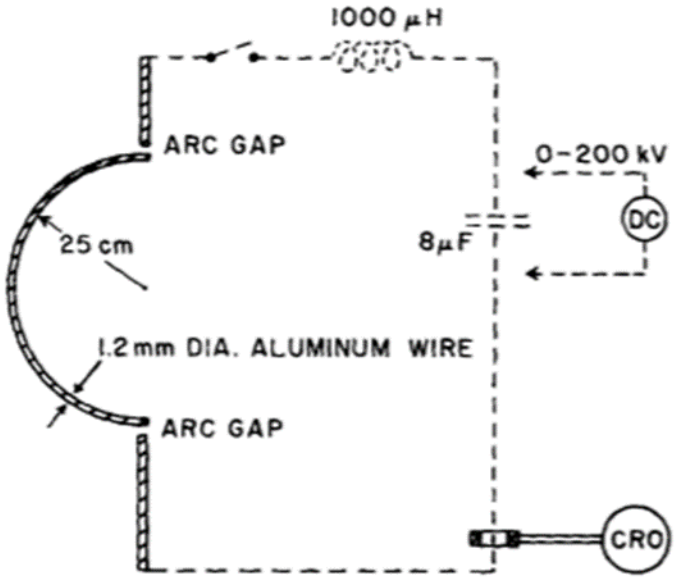

Figure 13. Semicircular wire fragmentation experiment setup. Source: Graneau (1984b).

As Graneau (1984b) explains in his paper, experimentation with different voltage potential increments continued up until, at 68 kV and 6600 A, "the wire would break into

30 to 50 pieces” (p. 2599). At this point, the author explains that further discharge current increments would cause the wires to melt because of the growing temperature.

Both experiments had very similar outcomes. Some of the wire pieces were examined under an electron microscope, as shown in Figure 14. The pieces were clearly fractured due to stress forces and no signs of melting were found, which proves that the breaks happened in the solid state.

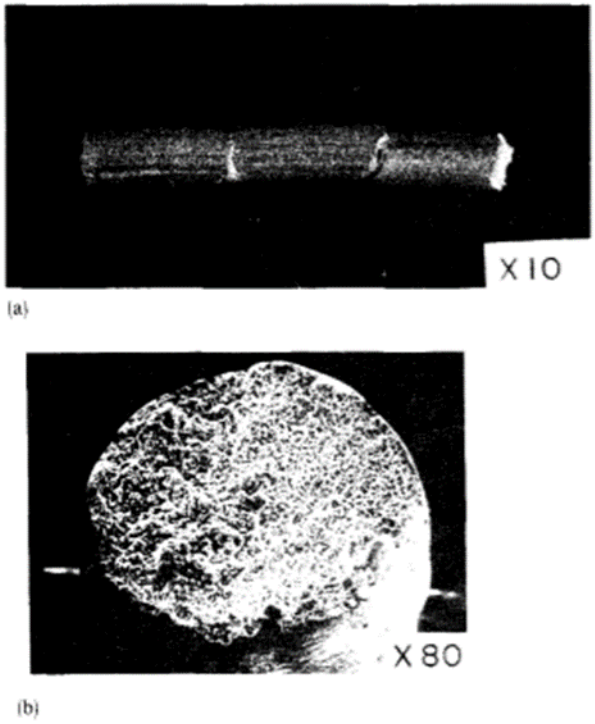

(a) Aluminum wire fragments. (b) Electron micrograph of a fractured wire.

Figure 14. Graneau’s wire fragmentation results.
Source: Graneau (1984b).

Based on the experiment setup, Graneau (1984a) explains that it is impossible for the Lorentz forces to act other than perpendicularly to the wire. Therefore, tensile stress had to be produced by Ampère’s force. This, in his opinion, proves the existence of Ampère’s tension.

5. Railgun Recoil Force

Railguns are a relatively new kind of weapon capable of firing a projectile by using the electromagnetic force created by a current that runs along two parallel conducting rails. Essentially, a high-voltage, high current, produced by a generator or a capacitor bank runs along two parallel conducting rails in contrary directions. The armature, which is placed perpendicular to both rails, closes the circuit and lets the current flow through itself. Once this happens, a magnetic field will be generated around the conductors of the circuit. Because of the Lorentz force, the current along the armature will produce a force that pushes the projectile along the weapon's axis and outside of the magnetic loop.

These forces are always perpendicular to the conductors and have a larger magnitude at the corners, as shown in Figure 15. Conventional wisdom says that normal recoil forces are supposed to react at the breech of the cannon, where the bus work connects perpendicularly to the rails. Yet, Graneau and Graneau (1996) contend that recoil forces along the rails occur as well. They state that "over 70 percent of the recoil force in one strip has its seat in the first ten centimeters behind the armature. This distribution implies that the rail will be susceptible to buckling" (p. 175).

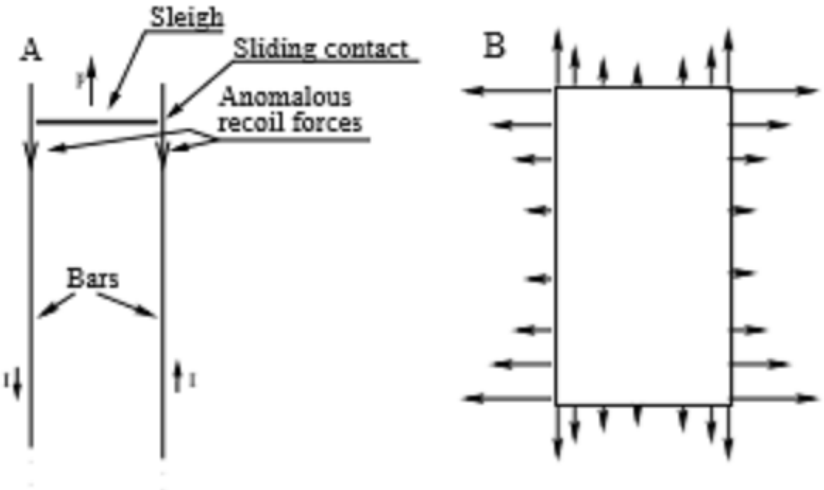

(A) Recoil force position in the rail. (B) Lorentz force distribution on the railgun circuit.

Figure 15. Railgun recoil force. Adapted from Johansson (1996).

In their book, Graneau and Graneau (1996) present a simple experiment to prove railgun recoil force. They prepared a railgun setup with rails made of two different metals. The thinner part of the rails was located in the last 40 cm of the rail, next to the armature. This part was made of aluminum or steel. The copper-made and thicker portion of the rails were located along the first 200 cm. Both parts were in slight contact with each other and they were allowed to move just on the longitudinal axis. This would cause the shorter section to get easily deformed in case of a backward push. When everything was ready, a current pulse was applied to the structure. As a consequence, as shown in Figure 16, the aluminum and stainless steel rails got deformed. The authors concluded by saying that "only the existence of longitudinal Ampère forces can adequately explain the observed rail buckling" (p.177).

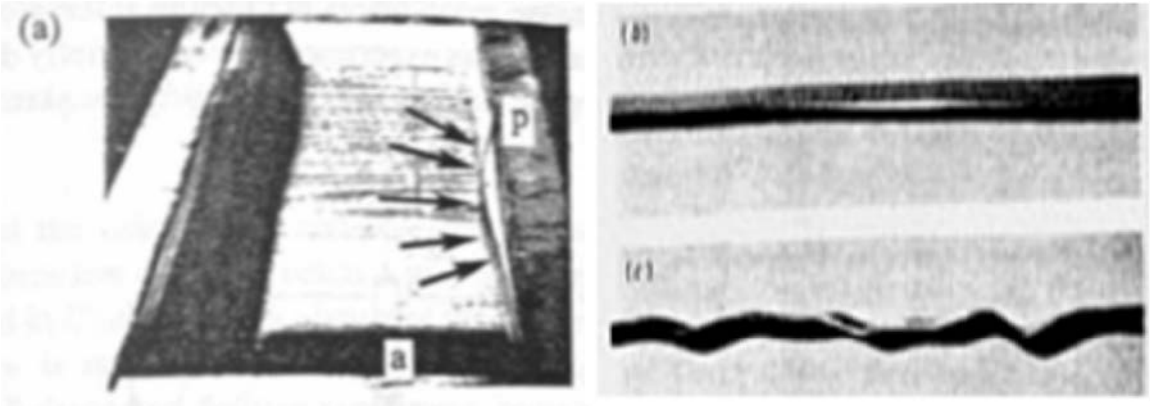

Left: Aluminum rail deflection. Right: Stainless steel rails before and after the experiment.

Figure 16. Rail gun recoil experiment. Adapted from Graneau and Graneau (1996).

B. ALTERNATIVE EXPLANATIONS TO THE EXPERIMENTAL RESULTS

After the experimental results were published, many scientists tried to find an alternative explanation to this phenomenon, other than Ampère's longitudinal forces. For example, the experiments by Graneau and Graneau involving an arc gap could be affected by the plasma pressure at the gap. The most studied case has been the wire fragmentation experiment, which seemed to be at the focal point of the discussion. Also, as Blondel (2009a) explains, it is better not to debate about the liquid metal experiments because they

are very “easily subjected to alternative interpretations” (p. 1). Therefore, most of the discussion around the existence of Ampère’s tension has centered around this particular experiment. Following this trend, this thesis analyzes the main objections that have been proposed to the wire fragmentation experiment.

1. The Pinch Effect

The pinch effect, first introduced by Hering in 1907, consists of a force that attracts a conductor radially to its own center. He was trying to prove that any conducting metal could be kept in its liquid form just by passing a strong enough current constantly through it. As shown in Figure 17, he filled an open channel with molten iron and placed two solid electrodes (E) on both sides of it. The arrows show the direction of the current flow. Nevertheless, what he saw was different, as Carl Hering (1921) describes in his paper “the liquid conductor contracted at one point (always the point of minimum cross section) forming a V-shaped valley” (p. 601). This effect has been widely studied in plasma physics applications and it is easy to observe in liquid metals, but not really common to detect in solid metal studies.

Figure 17. Hering’s observation of Pinch effect. Source: Hering (1921).

Molokov and Allen (1997) studied it on a solid metal conductor. In their work, they used “equations of magneto-thermo-elasticity” (p. 3132) taken from Moon and Maugin in 1984 and 1988, respectively. After some assumptions, they proved that a current running through a finite-length wire creates a purely azimuthal magnetic field. This would generate a radial Lorentz force, directed toward the wire axis, causing the pinch effect. (See Figure 18.)

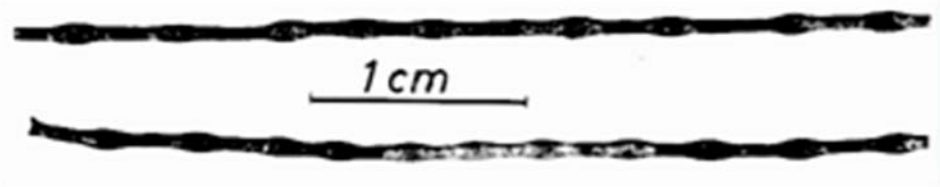

Figure 18. Pinch pressure on cables. Source: Nasilowski (1964).

The pinch effect is not usually strong enough to cause a deformation in metal wires. The current values obtained in these kinds of experiments, however, are so high that a significant rise in temperature in the wire is present, as was seen during the wire fragmentation experiment. Thus, as the metal tends to arrive almost to the melting point, the pinch effect might get strong enough to deform or even fragment the wire.

To disprove this argument, Graneau (1984b) explains that even if the pinch effect is real, and it can be clearly seen on liquid metals, “the wires broke without the formation of necks of reduced diameter” (p. 2599). This, in his opinion, eliminates the pinch effect as a primary reason for wire ruptures. Also, as Molokov and Allen (1997) describe, even if there is uncertainty about the real impact of this effect, evidence of plastic deformations could be observed in several wire fragmentation experiments including those of Graneau, producing permanent deformations in the metals.

2. Material Defects

Another possible reason that can lead to a conductor's fragmentation is the presence of material imperfections such as preformed cracks inside the conductor, or the existence of air in form of bubbles or other inclusions inside the metallic wire. One well-known challenge in welding is “hot cracking” or liquation cracking. This is most common in aluminum with silicon, copper, or magnesium alloying elements that form a eutectic at the grain boundaries and lead to fracture at high temperatures. All of these hypothetical cases could derive in overheating of the material which can cause plastic deformations and rupture of the material. Another consequence could be the deviation of the current flow through the wire, deriving a magnetic flux anomaly.

Once more, Graneau (1984b) defended his position by saying that none of the wires used in his experiments presented any of these defects. Furthermore, some of these wires were analyzed after the tests and no defects were found in the microscopic observations. He also argues that the number of wires used by many different scientists that have tried this same experiment is so high, that statistically speaking, it is very improbable for any mechanical defects to have an influence on the wire fragmentation. Nevertheless, mechanical defects, such as small cracks, sometimes can be imperceptible and even so cause a huge impact on a wire's structural homogeneity. Thus, its influence cannot be totally discarded.

3. Thermal Expansion and Longitudinal Stress Waves

When electric current travels through a conductor, the wire temperature rises because of joule heating. This phenomenon may cause the metal to eventually melt. Furthermore, there is a second effect on the wire, which is thermal expansion. As Molokov and Allen (1997) explain, the expansion of the wire is two percent in the radial direction and more than one percent of the wire's length. They studied the causes and consequences of this phenomenon when the wire ends were fixed and when they were free to move. When the wire is clamped as it was on Nasilowski's experiment, this expansion along with the magnetic force will produce buckling instability. Also, as Lukyanov and Molokov (2001) studied, flexural vibrations can be excited due to this phenomenon. After buckling fracture, all the compressive stress energy is released producing a tensile stress on the wire that leads to additional fractures.

On the other hand, when the conductor is free on its ends, meaning that it is not attached to any structure and restrained only by inertia, thermal expansion will create longitudinal stress waves, as shown in Figure 19 (Molokov & Allen, 1997). This was observed and explained by Ternan (1986), who described how these waves are created due to the resistance of the inertial forces inside the wire to expand as fast as the thermal expansion requires. Following this, if the heating rate is high enough, in a later moment, the elongation velocity of the wire becomes faster than the thermal expansion velocity, causing a tensile stress. This cycle repeats itself more than once, creating longitudinal stress

oscillations with an increase in tension and temperature for each cycle until the wire gets fragmented. In this case, the higher stress was found on the middle of the wire. Following this study, the model was improved by the inclusion of the skin effect, which is the tendency of the alternating current to remain on the surface of the conductor (Wall, Allen, Molokov, & Lukyanov, 2000). After that, as it was mentioned before, a third model was developed by Lukyanov and Molokov (2001), with the objective of explaining the causes and consequences of forces in a conductor with two clamped ends. Finally, Wall, Allen and Molokov (2003) completed the work by studying the continuation of the described phenomena, after the first fragmentation. It is important to specify that all of these studies are correlated among each other, and therefore, the graphics respond to wires of the same characteristics (1.2 mm diameter aluminum).

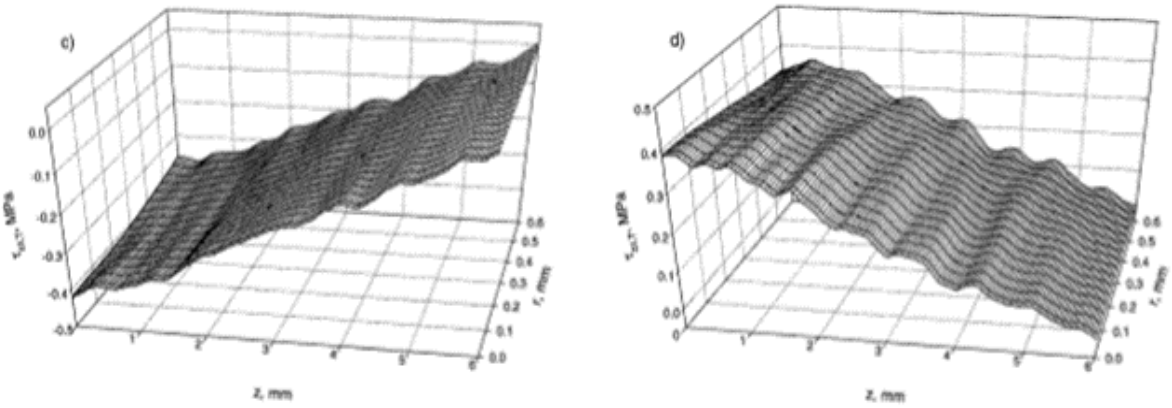

Figure 19. Longitudinal stress due to thermal expansion.
Source: Molokov and Allen (1997).

The most important conclusions at which these complementary studies arrived started with Molokov and Allen (1997), who studied these longitudinal stress waves and their behavior. Their research included the integration of the two main mechanisms that, in their opinion, lead to wire fragmentation. First, the previously mentioned “thermal and elastic or elasto-plastic stress waves caused by joule heating and second, the pinch effect” (Molokov & Allen, 1997, p. 3132). Their conclusion seems to be categorical at least for the first wire break:

> The present investigation has shown that the first fracture in sufficiently long wires with free ends occurs due to thermal standing waves. The second and subsequent fractures supposedly occur due to a combined effect of thermal expansion and unloading waves. This point is being investigated. (Molokov & Allen, 1997, p. 3140)

Along with this conclusion, the authors present a series of interesting results that show not only the thermal stress wave intensity with respect to time as shown in Figure 20, but also the maximum stress intensity and period length with respect to the wire's length as shown in Figure 21. As it can be seen from both images, in the case of the wire with free ends, the ultimate strength U of the wire (see Table 1) is reached easily. For the wire with clamped ends, however, their conclusion is not definite.

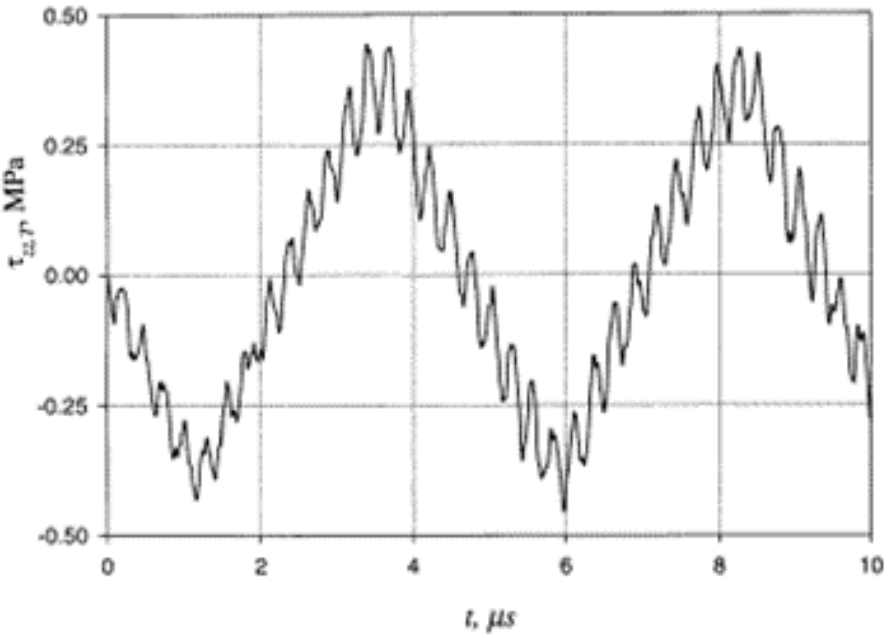

Figure 20. Free end wire thermal stress wave intensity with respect to time. Source: Molokov and Allen (1997).

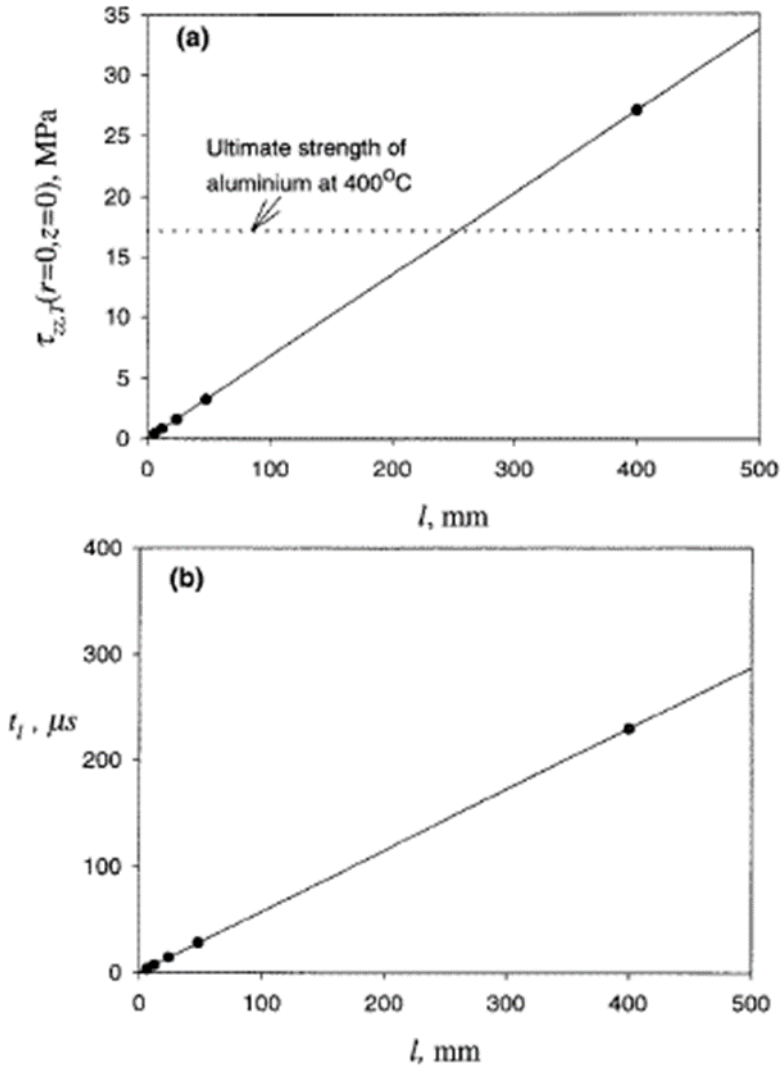

Figure 21. Free end wires max stress intensity and period. Source: Molokov and Allen (1997).

Table 1. Aluminum 99 percent ultimate strength. Source: Brandes and Brook (1998).

T (°C)	U (MPa)
24	90
100	75
148	60
203	40
260	30
316	17
371	14

Studying the case of a wire with free ends (unclamped), the model was updated with the inclusion of the skin effect, which revealed a meaningful difference in the performance of the stress forces along the wire's center (Wall et al., 2000). As the authors conclude, skin effect increases the stress forces that produce wire fragmentation. This is clearly observed in Figure 22.

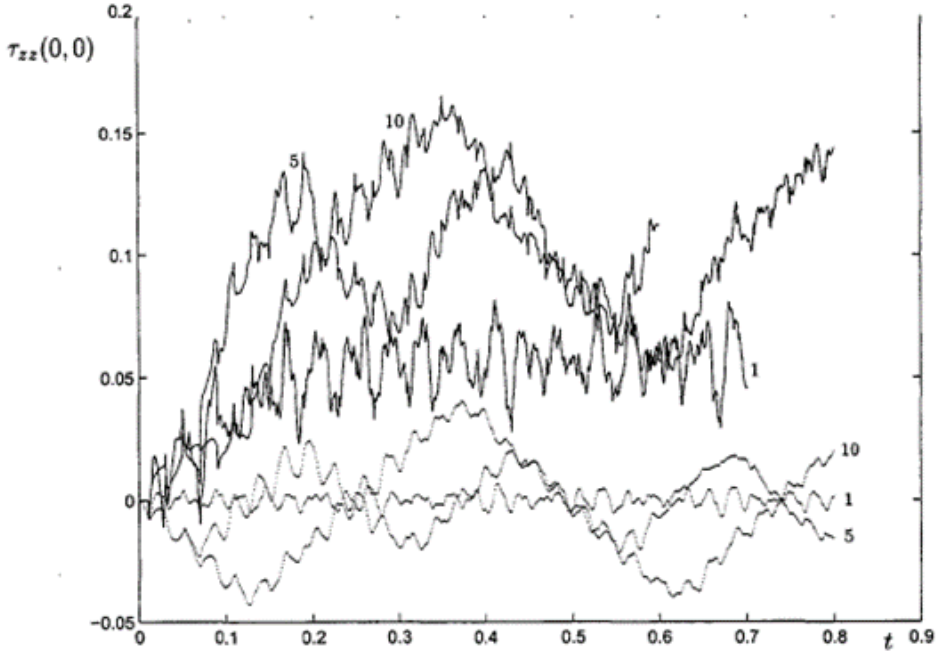

(A) Continuous line: skin effect included. Dotted line: skin effect not included.

Figure 22. Free end wire stress magnitude including skin effect. Source: Wall, Allen, Molokov, and Lukyanov (2000).

In another update of this thermal stress wave model, Lukyanov and Molokov (2001) tried to understand better the causes of wire fragmentation in wires with clamped ends. In order to do so, they took into account the flexural vibrations induced under clamped ends conditions. They elaborated a complementary model in which they studied the forces that generate a deflection X in a wire conducting a high pulse current (see Figure 23), and analyzed the stress force that these deflections would inflict on the wire. To do so, their model took into account the instability that leads to a deflection, that is, the force G applied along the z –axis (wire's longitudinal axis) to the wire ends due to thermal expansion, and

the force F_x created by the magneto-elastic buckling instability (Lorentz force on the x-axis, perpendicular to the wire's longitudinal axis).

As presented in their work, Lukyanov and Molokov (2001) define the force G with respect to time with the equation

$$G = ES\left\{\frac{\tilde{l} - \widetilde{l_0}}{L} - \alpha[T(t) - T_0]\right\}. \tag{16}$$

Here, L is the wire's length, E is the Young's modulus, S is the wire cross section, $\tilde{l} - \widetilde{l_0}$ is the increment of the wire length following thermal expansion, α is the coefficient of linear expansion, and the last term is the temperature difference at a certain time.

Also, the force F_x was calculated, as shown in Equation (17) using both, the Lorentz force formula and the Biot-Savart law, shown in Equations (41) and (42), respectively.

$$F_x = -\frac{\mu_0 I^2}{4\pi}\frac{\partial^2 \mathrm{X}}{\partial \mathrm{z}^2}\{\ln(2/ka) - C - 1/4\} \tag{17}$$

In the previous equation, a is the wire radius, C is Euler's constant, and k an integer depending on the wire's length. It is important to observe that when a perfectly straight wire with no perturbations is considered, the expected value for the force is equal to zero. However, this equation depends on the wire's form along the z-axis, which is never going to be perfectly straight. The authors also point out that this formula does not take into account the magnetic forces created by the geometry of the external circuit that carry the current into the wire, which can be strong if the circuit is not symmetrical.

As Lukyanov and Molokov (2001) describe in their work, "in both cases, the instability has a threshold character. When either the force G or the current I exceed some critical value, new stable states appear" (p. 1546). Solving the fourth order differential equation established by the model, shown in Equation (18), allows them to obtain a useful criterion capable of predicting, using the first eigenmode, when the instability will first appear. Subsequently, using the following eigenmodes, it is possible to predict higher modes as well. This way, it is possible to know when the system becomes unstable, allowing buckling to occur. It is also important to say that, as the authors claim, "the major

contribution [for the instability] is from the thermal expansion effect, while the influence of the magnetic force can be neglected during the initial stage" (p. 1547).

$$EJX^{IV} - GX^{II} - F_x = 0 \tag{18}$$

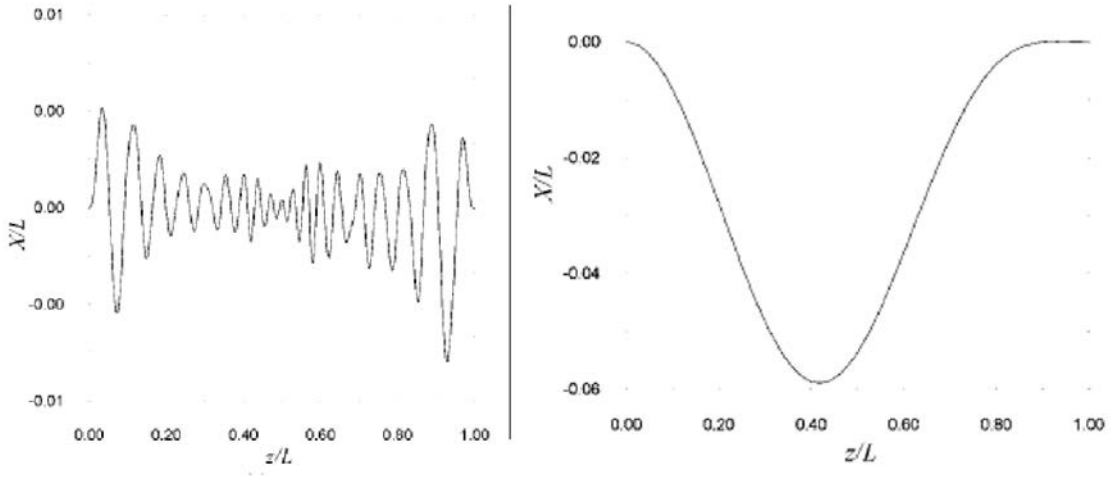

Figure 23. Displacement as a function of length position for a long (left) and a short (right) wire. Source: Lukyanov and Molokov (2001).

The qualitative stress analysis contributes to the observation that "once the instability occurs, all the potential energy within the compressed wire can be quickly released [as a form of stresses]" (Lukyanov & Molokov, 2001, p. 1547). Furthermore, factors such as temperature rise velocity, current amplitude, and material properties are going to affect directly the stress amplitude value. The analysis was made in view of two different conditions. The first one, on a perfectly straight wire, and the second one, considering an initially bent wire.

Finally, Lukyanov and Molokov (2001) present their numerical results for different experimental setups in which they mostly use aluminum wire of different lengths and different current values. As it can be seen in Figure 24, for a 50 mm length with 1.2 mm diameter aluminum wire, the stress values are strong enough to generate tensile ruptures on a conducting wire, especially at the wire ends. This result strongly supports their theory.

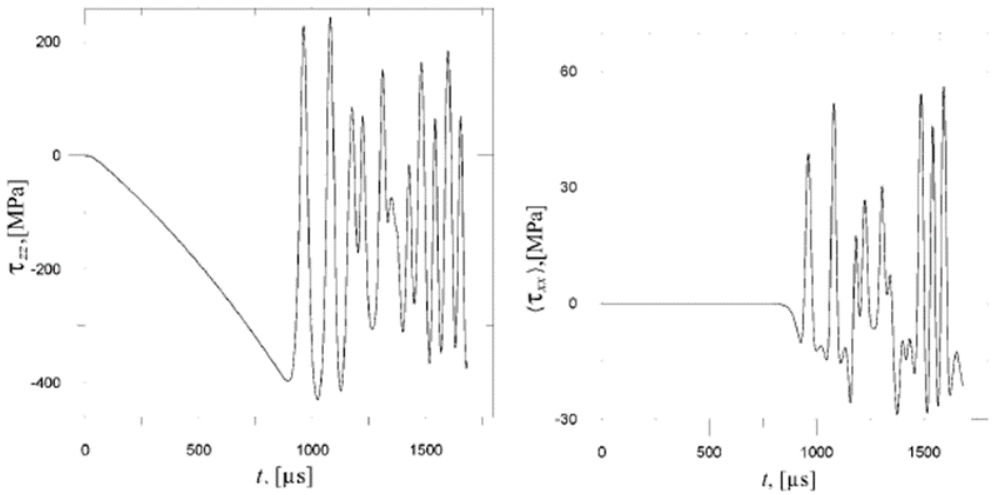

Figure 24. Longitudinal and transverse stress on a 50 mm length aluminum wire. Source: Lukyanov and Molokov (2001).

As mentioned earlier, the authors used a variety of wire properties and experimental conditions, which led them to conclude that the flexural vibrations created by joule heating and electromagnetic force are sufficiently strong to generate high tensile stress on a wire conducting high pulsed current. This tensile stress is high enough to cause a fracture on a wire before it melts. Also, even if the stress forces are lower in the case of a previously bent wire, the buckling instability is still sufficient to generate a fracture in around one millisecond. (See Figure 25.)

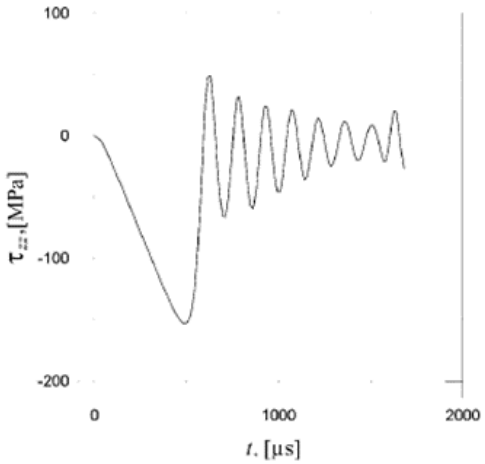

Figure 25. Longitudinal stress with respect to time for an initially bent wire. Source: Lukyanov and Molokov (2001).

In order to complete the study, one more model was presented in 2003. The last important update took into account that the previous research considered forces just until the wires first broke. Consequently, there was the necessity to develop a model that could examine the wire's elastodynamics after the first rupture and explain the multiple fractures observed in previous experiments. Also, the case in which there is one clamped and one free end was considered, as this case had never been studied before (Allen, Wall, & Molokov, 2003).

Following the previous models' trend, the study conducted by Allen, Molokov, and Wall (2003) determined that, when the wire had one clamped and one free end, the longitudinal stresses are higher on the clamped end due to the thermal expansion and the Lorentz force. This result was consistent with the previous models' results.

Perhaps the most important contribution of this particular research, however, are the conclusions about the elastodynamic behavior of the wire after the first rupture. The investigation took into account three typical cases: both clamped ends, both free ends, and one free and one clamped end. The authors introduce a mechanism they call the pre-loading of the wire. This happens when the wire has not yet broken but it starts to accumulate stress due to the previously mentioned thermal and electromagnetic mechanisms. For the first case of both ends clamped, as shown in Figure 26, after the first fracture, tensile stresses actually increase due to the change in boundary conditions. In other words, the pre-loading of the wire has almost no contribution to the successive breaks. Instead, it is the change in boundary conditions due to the first fracture that triggers an increment in the stresses along the wire.

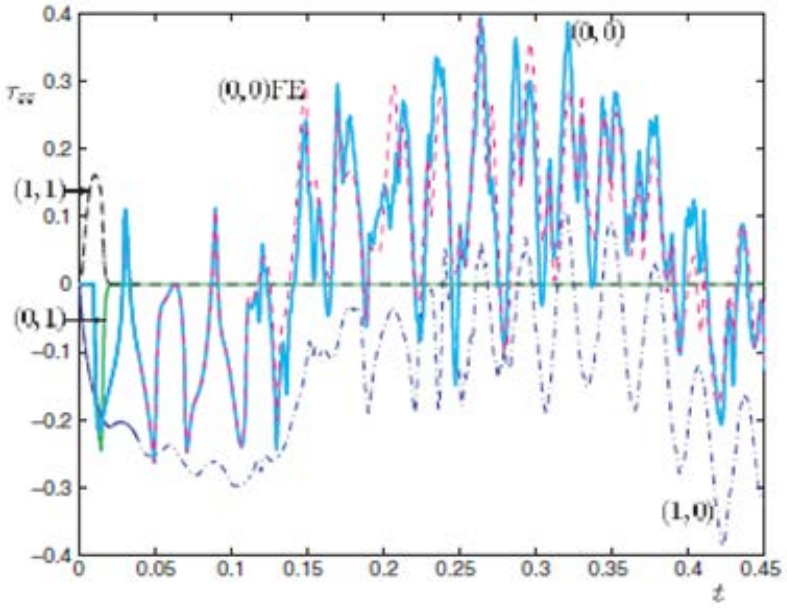

Blue Line: From 0-0.15 seconds the wire is clamped. At 0.15 s, the wire breaks on both ends. Red dashed line: Free end wire.

Figure 26. Longitudinal stress on a clamped end wire after first fracture. Source: Allen, Molokov and Wall (2003).

For the second case of both ends free, as Molokov and Allen (1997) describe in their work, the first fracture happens on the center of the wire due to stress waves created by the thermal mechanism. Hence, the model generated by Allen, Molokov and Wall (2003) uses this as the initial condition from which to study successive fractures. Once again, the model supported the theory. In this case, the pre-loading of the wire is the main reason for the continuous fractures. Therefore, as the authors explain, "the peak post-fracture stress values are approximately the same magnitude as the peak pre-fracture values, and so the fracturing process is expected to continue" (p. 2763). They were able to estimate also the time of the second fracture, which in this case was much lower than the predictions made by Wall et al. (2000). Finally, for the last case in which the wire has one free and one clamped end, the mechanism by which successive fractures occur is mostly the same as discussed for the previous case, where high stress is maintained in the wire due to the pre-loading mechanism that preceded the first fragmentation (Allen et al., 2003). One last important statement made by the authors was that their results "suggest that time

interval between successive fractures will tend to decline as the wire pieces' aspect ratio is reduced" (p. 2766).

During the years after Ternan's theory was published, Graneau (1987) refuted the effect of longitudinal stress waves by presenting a series of arguments. First of all, he claimed that, because the theory is conclusive only for wires that are not constrained in any direction, it fails to explain why Nasilowski observed wire fragmentation in his original experiment. Nevertheless, Lukyanov and Molokov's (2001) results later negated this argument. The second argument used by Graneau is that, using Ternan's mathematical formulas, tensile forces produced by standing stress waves for 5 milliseconds would be insignificant.

The third disproving argument exploits the fact that, from Ternan's theory, length is directly proportional to the tensile forces caused by these waves. On this point, Graneau (1987) explains that observations on wire fragmentation experiments have shown that fractures occur one after the other, not simultaneously. Meanwhile, current arcs between fragments maintain the current flowing along the structure. According to Graneau's interpretation, this fact supposes that Ternan's analysis is inconsistent with reality because "in the latter stages of the process it must be possible to fracture a 2 cm long piece after it has been almost fully expanded by previous heating" (p. 78), which does not make sense since longitudinal stresses should be negligible. Yet, as we have demonstrated in this chapter, in the last few decades plenty of theoretical evidence regarding stress waves in conducting wires has been discovered. For that reason, Graneau recognizes that nowadays, even if the debate over Ampère's longitudinal forces is still open, traveling stress waves and thermal effects are plausible alternative explanations for the wire fragmentation phenomenon (private correspondence, October 3, 2018).

IV. MODELING AND EXPERIMENTAL PROCEDURE

In this chapter, we present two different experiments that may help elucidate the physical mechanisms that lead to wire fracture in the presence of large current pulses. The first experiment was conducted using the High Current Test Fixture (HiCTF) at the Naval Postgraduate School (NPS) Railgun Facility. The tests were recorded with a high-speed camera and the video images were analyzed with Digital Image Correlation and Tracking (DICT) software. The second was a numerical analysis using the COMSOL Multiphysics program. In this chapter, the procedure for both experiments is described.

A. EXPERIMENTAL STUDY DESIGN

From Chapter III we can see that there are two different and competing explanations for wire fragmentation. With the debate still ongoing, many different approaches have been developed and tested on laboratories around the world. Based on Ternan's (1986) initial studies, Molokov and Allen (1997) developed a very convincing theory to explain the phenomenon. Their thermal expansion and longitudinal stress theory was supported by computational models from which they were able to reach very appealing results. The model was complemented by other research studies explained in Chapter III. Later, the elastodynamic properties of the wires were included in the model, expanding the predictions, as Wall (2003) showed in his work. With this result in mind, an experimental setup was prepared in order to replicate the thermal stress wave model and look for empirical evidence to assess its accuracy.

As explained previously, Molokov and Allen (1997) elaborated a numerical model using the magneto-thermo-elasticity equations to study the stress waves created on a metal wire when a high-pulsed current runs through it. From there, they determined the magnitude of tensile stresses and, comparing them to the material’s ultimate strength, shown in Table 1, concluded that for some specific cases, tensile ruptures could be induced. This model, along with three other models based on the same theory, have been described in Chapter III. A 1.2 mm diameter wire was used in all the models. The length varied from 24 mm to 1 m. The metal used was either 99 percent aluminum or copper. They used a

constant 5000 A current (I). The pulse time limit was of 3.1 ms because at that time the wire is supposed to reach its melting point of 660 °C.

The experiment developed for this research used the HiCTF to conduct a high pulse current on straight wires. The pulses were controlled to generate a certain amount of current throughout the conductors. At the same time, a high-speed camera (Phantom 2511) was used to record the events. Afterwards, the recordings were analyzed through a DICT program and the remaining pieces were observed using an optical microscope.

1. High Current Test Fixture (HiCTF)

The HiCTF, shown in Figure 27, consists of a SUNEX H steel structure frame with two sets of conducting cables that carry electricity from the capacitors to the conductive ends through two aluminum arms connected to the structure. It is important to note that the structure is electrically insulated from the cables by electrical insulated G10 blocks. The aluminum arms that carry the current conduct the electricity from both sides of the structure to the test fixture material interface test area. The test area is contained between two large G10 blocks supported by four steel guide rods. The separation between the upper and lower G10 blocks is variable. The current enters the test area symmetrically from both sides following to the upper G10 block through an aluminum bus bar. This bar has a specially designed aluminum cone. The apex cone section, where the sample is attached, has a one-inch diameter. On the lower G10 block, there is another aluminum cone with the same characteristics as the previous one. This cone leads the current through a vertical hole below the main structure and outside of it following the lower aluminum conducting arms.

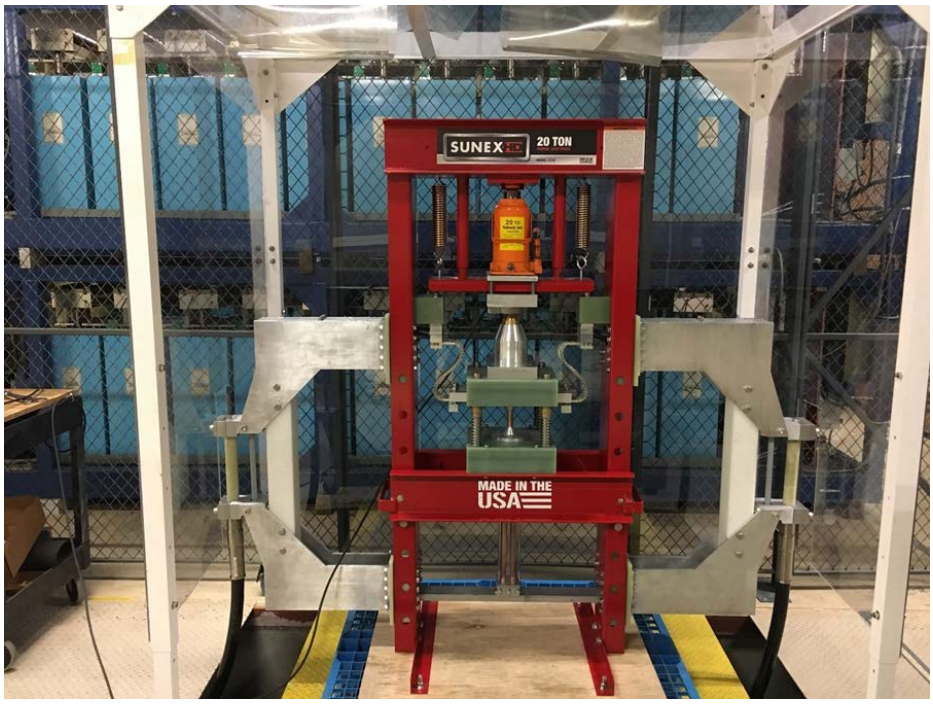

Figure 27. High Current Test Fixture (HiCTF)

The HiCTF also has one hydraulic bottle jack capable of exerting a constant and uniform compressive force on the test area below it. This force can be controlled and modified using a manual lever. For this experiment, however, no pressure was needed and therefore this feature was not used. The pulsed power supplied to the HiCTF is generated by a 22 capacitor bank that is discharged through two counter-wound inductors, with inductance equal to 32 µH. Each capacitor has 826 µF nominal capacitance, with an 11 kV maximum voltage and 50 kJ storage energy at its maximum capacity. In the absence of resistive losses, peak current can be obtained using the balance between capacitive and inductive energy, or

$$I_{Peak} = V\sqrt{\frac{C}{L}}, \tag{19}$$

with L the inductance, C the capacitance, and V the charge voltage to the capacitor bank.

In order to conduct the tests, some mechanical pieces were customized. It is important to remember that the current had to flow symmetrically from top to bottom and the wires had to be straight and perpendicular to the floor. From now on, the wire will be

considered to be parallel to the Z direction, being XY the plane on which the laboratory floor lays. As explained before in this chapter, two different diameter metal wires were used. Therefore, two different pair of mechanical test pieces were made. For the thinner wire, as shown in Figure 31, the pieces used were two aluminum small solid cylinders with a hole in the middle and an aperture along their diameter. A hose clamp permitted the wire to remain attached to the upper and lower pieces. This allowed the test to be made with both ends clamped and with one free end. For the thicker wire, the mechanical pieces consisted of two larger cylinders with a hole surrounded by a particular O-ring made of rubber and covered with a conductor that allowed the current to run through the circuit and at the same time allowed the wire to move longitudinally. We considered this to be a wire with free ends case. Both pieces are shown in Figure 28. Finally, in order to test the long 230 mm wires on the HiCTF apparatus, a special modification was needed as shown in Figure 33. The upper G10 block was removed and replaced by a special metal bus bar designed to increase the test area space available in the z axis. The solid cylinder, on which the wire was clamped, was screwed directly into the new metal bus bar.

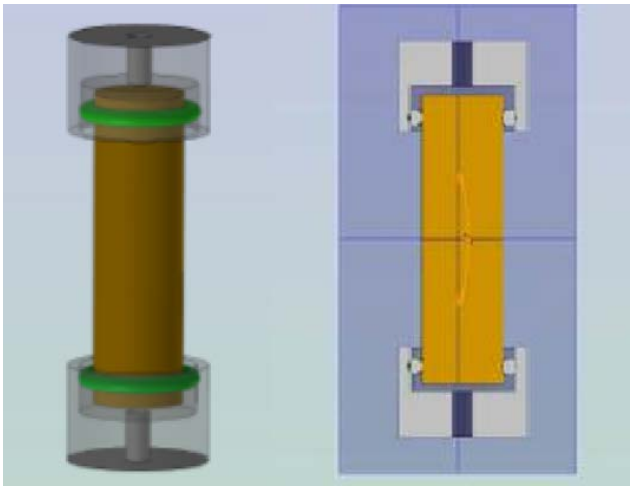

Figure 28. Thicker wire experiment

2. High Speed Camera and DICT

For better analysis of the test results, a Phantom 2511 high-speed camera was used during the experiment. The camera was placed in front of the HiCTF and connected using

an Ethernet cable to a computer placed in the control room from which the Phantom 2511 software was monitored and controlled. We used a 100 mm focal length lens. As seen in Figure 29, lighting was an important factor to be considered for the experiment, which used both incandescent and LED lights. In this case a backlighting technique was used. This was because DICT software needs a clear contrast and intensity level differentiation between the images that are going to be processed. As shown in Figure 32, a Plexiglas piece was placed between the sample and the camera to protect it from any possible explosions.

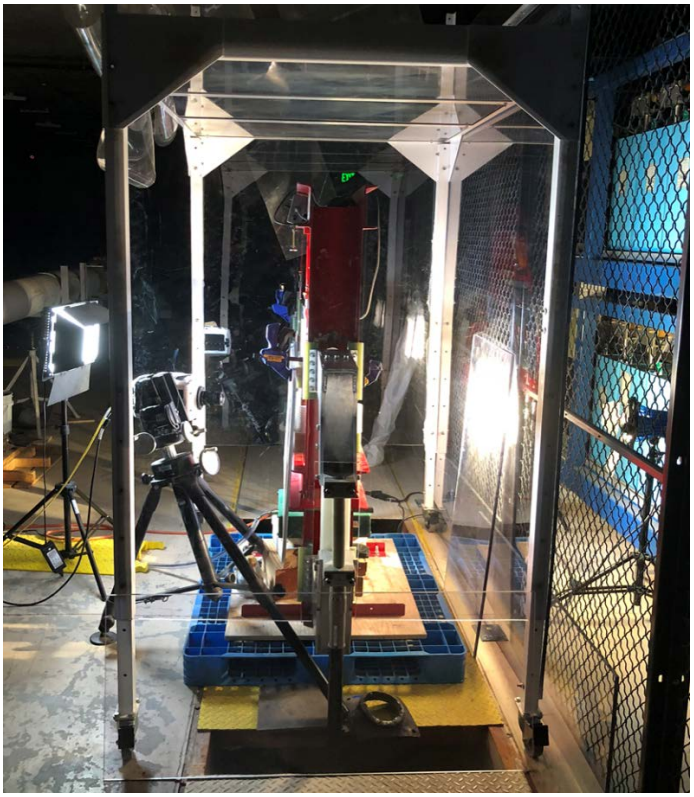

Figure 29. Lighting of the first two experiment setups

Three different video settings were used during the shots, as follows: the first one with resolution of 256x128 pixels, sample rate of 380,000 fps, and exposure time of 1 µs, from now on called the “first configuration.” The second one had 128x64 pixels with 600,000 fps and 1.8 µs exposure time, from now on called the “second configuration.” Finally, the third one had a 256x256 pixel resolution, with 200,000 fps and 3.6 µs exposure

time, from now on called the “third configuration.” After the video was recorded, we used DICT software to get information using a digital image correlation procedure. This kind of software allows the user to measure mainly strain and displacement by comparing consecutive frames on a video and tracking blocks of pixels (McCormick & Lord, 2010). As McCormick and Lord (2010) describe, “the system can measure surface displacement and build up full field 2D and 3D deformation vector fields and strain maps” (p. 52).

3. Experiment Design

In our case, the experiment design was based on the computer models used by Molokov and Allen (1997), Lukyanov and Molokov (2001), and Allen, Molokov, and Wall (2003). The objective of the experiment is to obtain enough empirical evidence of the causes and consequences of thermal stress waves on wires subject to high pulsed currents. The causes and consequences studied in the models are explained in Chapter III, and are be emphasized on Chapter V. To meet this objective, it is necessary to replicate the conditions and parameters used in the models. For that reason, we used aluminum wire of two lengths and two different diameters, while varying the current amplitude discharged through the wires and the “clamped” or “free end” condition of the experiment. The statistical design of this experiment can be expressed as a 2-by-2 matrix array as shown in Figure 30.

The rows determine the length of the wire, while the columns determine the diameter. As depicted in Figure 30, the diameters employed for the experiment were 1.25 mm and 19 mm, while the lengths used were 70 mm and 230 mm. Also, the element A_{11} experiment was chosen to replicate Molokov and Allen’s model. The other three are variations of that model. From now on, each element of the matrix represents one of the wires used in the experimentation process. Also, as the process was conducted on the cited models, we tried to vary between clamped and free ends, current intensity, and digital camera setup for each of the four elements. Finally, we tried different combinations for each matrix element as follows.

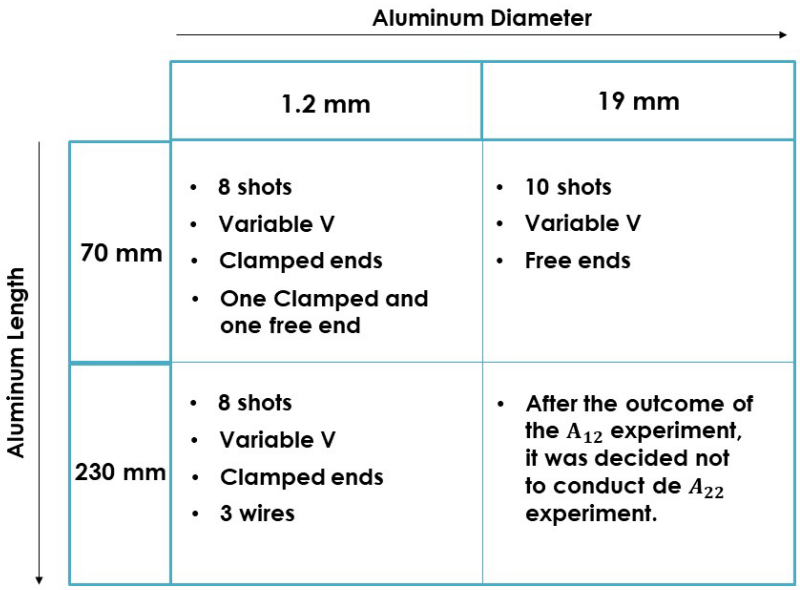

Figure 30. 2-by-2 experiment matrix

For the A_{11} element wire, eight shots were made. As shown in Table 2, almost all the shots were made in clamped ends conditions and with a voltage discharge between 100 V and 400 V, yielding currents of several kA. It is important to say that these shots were significant not only for the experiment's objectives, but also because the first five shots were used to calculate how much current was actually going through the wire using the oscilloscope data, and also to calibrate how good the camera image was in order to be processed by the DICT software. Different techniques were used in order to obtain a good image resolution and the best possible reference points from the wire. During the first four shots, the wire was marked with a permanent marker and lights were pointing directly at the sample. The fifth and sixth shots were done under backlit conditions. The sample was filled with different possible references points and after the shots were made, we were able to determine the best technique to use. As shown in Figure 31, the methods went from white paint with permanent marker graduations, sand particles attached with spray adhesive, fishing wire glued with super glue product, and others. A downselect was made based on how well the reference point survived the current pulse and how well the DICT software was able to analyze the data.

Figure 31. Test shot to verify camera resolution

Table 2. A_{11} element wire shots description

	Voltage (V)	Camera configuration	Wire ends
1st shot	100	1st configuration	Clamped ends
2nd shot	200	1st configuration	Clamped ends
3th shot	300	1st configuration	Clamped ends
4th shot	400	1st configuration	Clamped ends
5th shot	300	1st configuration	Clamped ends
6th shot	400	1st configuration	Clamped ends
7th shot	200	1st configuration	One free end
8th shot	350	2nd configuration	One free end

For the A_{12} element wire, a total of nine shots were made. The process to test the A_{12} element was faster and easier compared to the thin wires. This was mainly because the thicker wire did not explode, and therefore, it was not changed at any time. The rod was free to move in the z direction, and it was discharged with voltages from 200 V to 1 kV, as can be seen in Table 3. A fishing wire was glued all around the rod in a spiral, in order to

have a reference point on the video images. A picture of the experiment setup is shown in Figure 32.

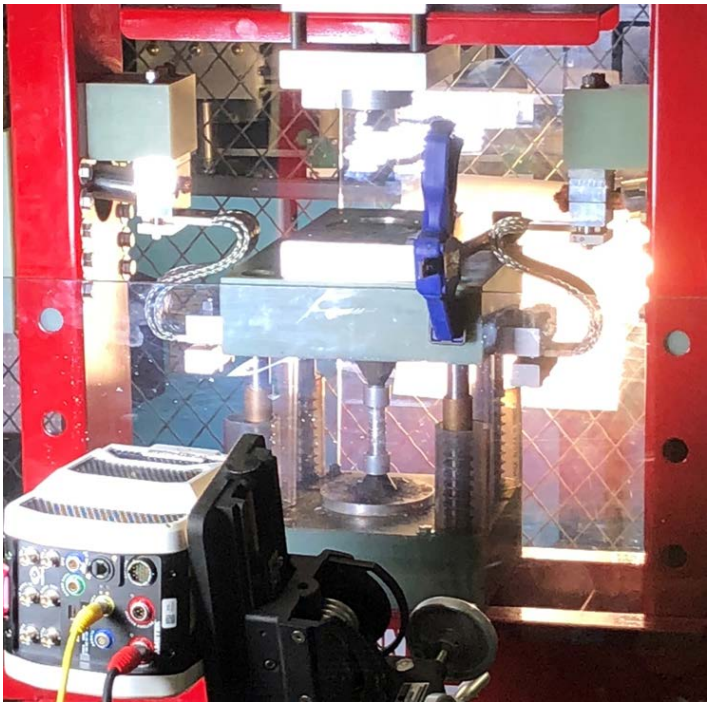

Figure 32. A_{12} wire element test setup

Table 3. A_{12} element wire shots description

	Voltage (V)	Camera configuration	Wire ends
1st shot	200	1st configuration	free ends
2nd shot	300	1st configuration	free ends
3th shot	400	1st configuration	free ends
4th shot	500	1st configuration	free ends
5th shot	600	1st configuration	free ends
6th shot	700	1st configuration	free ends
7th shot	800	1st configuration	free ends
8th shot	900	1st configuration	free ends
9th shot	1,000	1st configuration	free ends

For the A_{21} element wire a total of eight shots were made, as described in Table 4. This time three wires were tested. The first wire got tested four times, the second wire was tested three times, and the last wire got tested one time. The voltage discharge values varied

between 100 V and 400 V. At this point in the experimentation process, the decision of fill the sample with any kind of reference point was abandoned, and therefore, all the shots were made under direct light. This decision was made for two main reasons. First, because the sample was too big to allow the camera to record with less than 256x256 pixel resolution. As a consequence, the frames-per-second rate was too low to allow any kind of effective DICT analysis. Second, we considered that having any kind of extra weight attached to the wire could possibly cause a damping effect on any possible stress wave. The sample setup for the A_{21} element is shown in Figure 33.

Figure 33. A_{21} wire element test setup

Table 4. A_{21} element wire shots description

	Voltage (V)	Camera configuration	Wire ends
1st shot	100	3th configuration	Clamped ends
2nd shot	200	3th configuration	Clamped ends
3th shot	300	3th configuration	Clamped ends
4th shot	380	3th configuration	Clamped ends
5th shot	200	3th configuration	Clamped ends

6th shot	300	3th configuration	Clamped ends
7th shot	400	3th configuration	Clamped ends
8th shot	390	3th configuration	Clamped ends

B. NUMERICAL COMSOL STUDY

The numerical analysis was conducted using COMSOL Multiphysics. This software allows the construction of a computational model to study the behavior of a system with precise accuracy. The idea behind the COMSOL model was to reproduce the conditions that were applied on the wire fragmentation experiments. The main objective was to generate evidence that could be correlated to one of the causes for the fragmentation phenomenon to occur.

The model was able to explore and identify the behavior of the wire by correlating the mechanical structure physics, heat transfer in solids, and magnetic fields contribution at the same time. All of this happening in a wire subject to a 5-millisecond pulse of 306,900 A peak current, called Cur_pulse, as shown in Figure 34. It is important to underline that these current values were used purposely to exaggerate the results on the model, but they are much higher than the real values obtained with the HiCTF experiment. The results analyzed temperature changes along the wire, as well as forces, Von Mises stresses, magnetic fields, and current densities. This simulation was based on the COMSOL model elaborated by LT Paul Cross in a previous NPS research thesis.

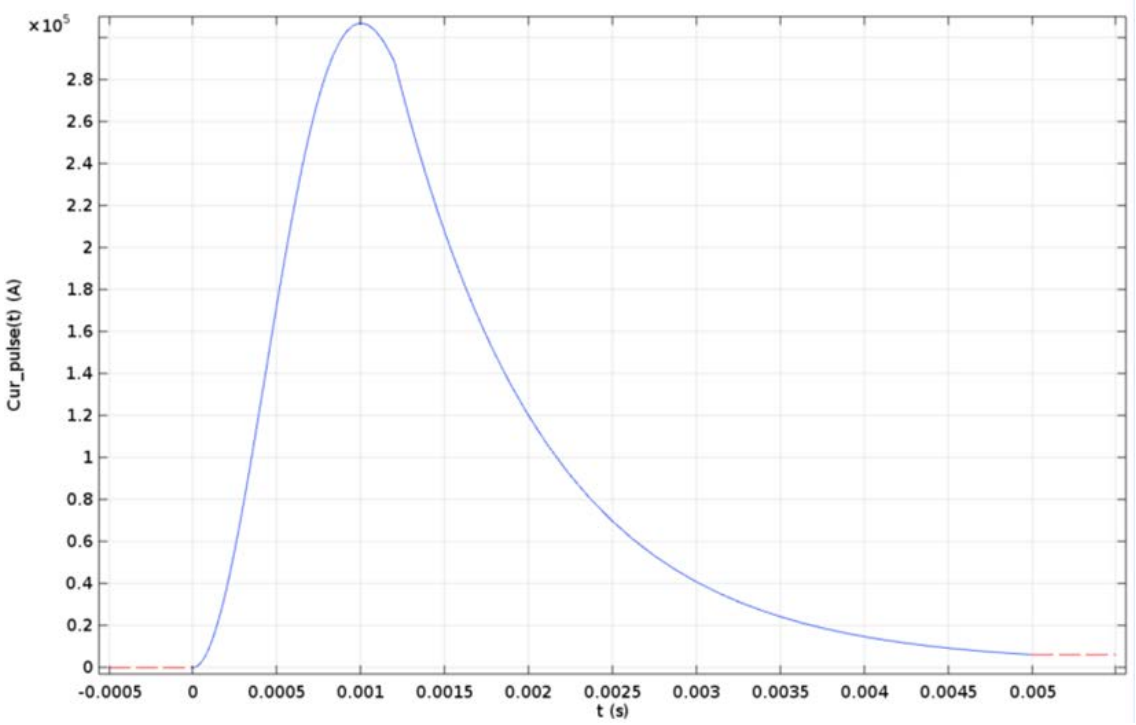

Figure 34. Current pulse function used on the model

1. COMSOL Model Description

The COMSOL 5.3a version was used to create this model. The base model geometry components are described as follows: one copper/aluminum wire of 90 cm length and 1.25 cm diameter. The wire is inside of an air cubic box with 100 cm side length as shown in Figure 35. The temperature inside the model is 293.15 degrees Kelvin, and the pressure is 1 atm. The current pulse was divided into 50 time steps, from 0 to 5 milliseconds. Additionally, three different structure modifications were added to the base model. The first one was the inclusion of an air bubble inside the wire, the second one was the presence of a crack perpendicular to the wire axis, and finally, a variable force along the wire.

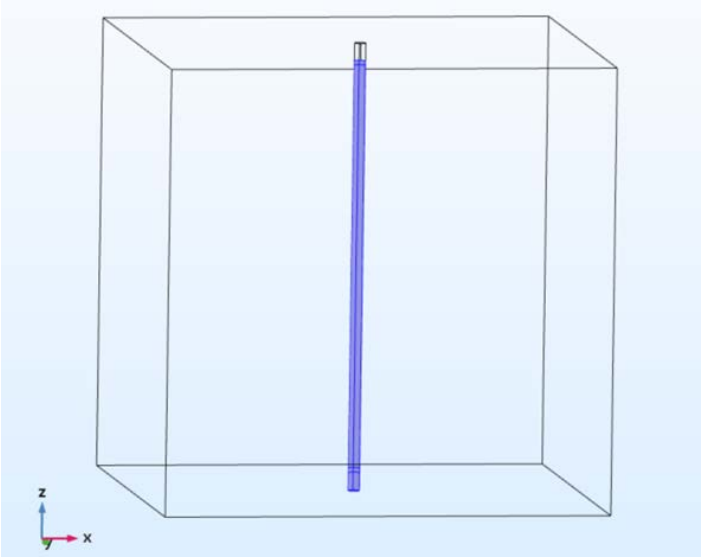

Figure 35. COMSOL Geometry representation

As described before, this model uses three different physics modules plus one equation-based modeling interface and the multiphysics module to correlate them all.

2. Solid Mechanics Component

This component is part of the Structural Mechanics module and it was used to elaborate a three dimensional (3D) structural analysis on the metal wire. It calculates the resultant force generated across the wire due to the thermal expansion and the Lorentz forces created by the current (COMSOL, 2015d). Additionally, gravity conditions were altered in order to produce different results. The submodules added by default inside of the solid mechanics component were “Linear elastic material,” “Free,” and “Initial values.” These three submodules were applied to the whole structure except on the “Lumped port” from where the current would flow to the wire. As COMSOL (2015d) explains, the first one allows the user to define the linear elastic material properties. An isotropic model was selected, and the temperature and absolute pressure were defined as previously described in this thesis: 293.15 K and 1 atm. On the other hand, Young’s modulus, Poisson’s ratio, and density values were taken from the material properties inside of the COMSOL Multiphysics database. The second one (“Free”) shows which components have no constraints or loads acting on them, identifying which of them can move and react to the

stress forces. The third submodel ("Initial values") allows the user to define a predetermined initial displacement field or structural velocity field, which in this case was set to zero. Also, a "Fixed constraint" boundary condition was added to the wire's ends, which implies that the displacements are zero in all directions, making the geometric entity fixed. Finally, in order to simulate a volumetric force to the selected domains, a "Body Load" was added to the component. The load type was defined as "Force per unit volume" and the "Lorentz force contribution," previously defined on the "Magnetic Field" component, was selected.

3. Heat Transfer in Solids Component

This component is part of the Heat Transfer module and it is used to model heat transfer in solids by conduction, convection, and radiation (COMSOL, 2015c). Because of the electricity conduction along the wire, there will be a joule heat increase along the material. The ambient variables were maintained at 293.15 K for the ambient temperature and 1 atm for the ambient absolute pressure. Again, this component adds three submodules by default: "Solid," "Initial Values," and "Thermal insulation." In its handbook, COMSOL (2015c) clarifies that the first one allows the users to state which components will be subject to heat transfer and define the different variables that contribute to the heat transfer equation, such as thermal conductivity (k), density (ρ), and heat capacity at constant pressure (C_p). All of these variables where taken from the material properties of COMSOL'S database. The second, "Initial values," allows the program to set the initial conditions of the temperature on the model, which was set to 293.15 K on every component. The "Thermal insulation" submodule allows the software to set the heat flux across any boundary to be equal to zero, specifying where the domain is totally insulated. In this case, none of the boundaries was selected. Finally, the "Convective Heat Flux" submodule was added to the component in order to add convective heat flux across one end of the wire.

4. Magnetic Fields Component

This component is part of the AC/DC module and it is used to compute the magnetic field distribution along a conductor (COMSOL, 2015a). Three predetermined submodels

were added to the module: “Ampere’s Law,” “Magnetic Insulation,” and “Initial Values.” The first one was defined along the conductive wire and it allows the program to take in count of the magnetic and electric fields produced by the current. On this submodel it is possible to determine the three material constants that contribute to the magnetic and electric fields equations. In this case, the constants were taken from the materials database from the COMSOL software. The “Magnetic Insulation module” node sets the tangential component of the magnetic potential to zero. It was applied to the wire’s ends. The third submodule is the “Initial values,” which adds an initial value for the magnetic vector potential on the selected domains. In this case, the predetermined initial values were set to zero. Finally, a “lumped port” submodule was included to the model. This feature allows the software to apply a uniform electric field to the wire. Cur_pulse was applied to the wire.

5. Multiphysics Coupling

This COMSOL Multiphysics section allows the software to take different components' equations and solve them as a coupled system. It is a powerful tool that allows the user to solve problems with multiple physics on it.

- In this particular model, three different multiphysics couplings were used: “Electromagnetic Heat Source,” “Temperature Coupling,” and “Thermal Expansion.”

- The “Electromagnetic Heat Source” coupling was used to take into consideration the electromagnetic losses (COMSOL, 2015b). In order to do so, the “Magnetic fields” and “Heat transfer in Solids” physics were coupled.

- The “Thermal Coupling” is used to grab the temperature from a source and use it as the predetermined model input for a separate physics interface. This feature uses always the “Heat transfer interface” as a source and evaluates material properties in a destination, which in this case is the “magnetic fields” feature (COMSOL, 2015b).

The “Thermal Expansion” coupling produces an internal thermal force (strain) caused by temperature changes inside the material. It is necessary to choose where the heat is coming from (“Heat transfer in solids) and what the interface will be affected (“Solid Mechanics”). In this case, it is possible to input some constant and properties values such as temperature and pressure.

6. Structural Defects Modeled in COMSOL

Starting from the base model presented earlier, one structural defect has been modeled as shown in Figure 36. The defect is a bubble inside the wire. For this case, a spherical structure was created and located inside of the cylinder at a random position along the wire but centered on the wire's longitudinal axis. This sphere was selected to be made of air, and the only physics applied to it was the “Magnetic Fields” physics. All the other features remained equal.

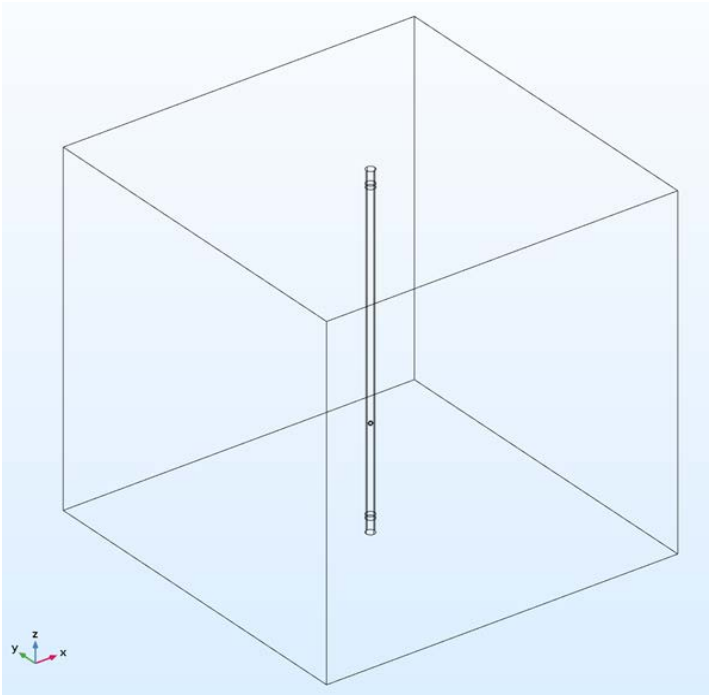

Figure 36. Bubble inside the wire, COMSOL model

V. RESULTS AND ANALYSIS

One of the experiments used to assert the existence of Ampere's longitudinal force is Nasilowski's wire fragmentation. Among the alternative explanations to his observations, thermal stress wave theory has gained acceptance among the scientific community. As we discussed in the previous chapters, numerical models seem to confirm this explanation. Nevertheless, other than the computational evidence, no experimental confirmation of the theory has been found among the literature. The purpose of this thesis has been to address this gap by analyzing results of wire fragmentation experiments with fast video capturing. We approach this task by determining the maximum displacement of the wire and analyzing, where possible, the deflection and buckling waves during and after the shot. Finally, we will present microscope images of the wire's fragmentation pieces in order to determine possible causes.

As we explained in Chapter IV, Section A, the experiment was divided into three phases using the 2-by-2 matrix shown in Figure 30. Each phase takes the name of its respective position on the matrix table A_{11}, A_{12}, and A_{21}. The experiments were conducted using aluminum wire with 1.25 mm and 18 mm diameter. Our analysis incorporated the following aluminum characteristics: density ρ=2700 kg m^{-3}, electrical conductivity σ=3.745 × $10^{7}\ \Omega^{-1}m^{-1}$, electrical resistivity at room temperature ρ_{eo}=2.67 × $10^{-8}\ \Omega$ m, temperature coefficient of resistance α_T=3.8 × $10^{-3}\ C^{-1}$, linear thermal expansion coefficient α_e=2.35 × $10^{-5}\ K^{-1}$, specific heat c_v=938 $J\ kg^{-1}K^{-1}$, and initial temperature $T_0 = 293\ K$, corresponding to room temperature.

For every shot we obtained current pulse data, which allowed us to determine the maximum temperature reached on every shot, according to the relation

$$\mathrm{E} = mc_v\Delta\mathrm{T} = \int_0^t I^2\,R dt. \tag{20}$$

with I being the current, R the resistance, m the mass of the wire, and ΔT the temperature difference ($T - T_0$), with the resistance determined in terms of the electrical resistivity as

$$R = \rho_e \frac{l}{A}, \tag{21}$$

where l is the length and A is the cross sectional area of the wire, and

$$\rho_e = \rho_{eo}(1 + \alpha_T \, \Delta T). \tag{22}$$

Combining Equations (20), (21), and (22) we obtain

$$mc_v \, \Delta T = \int_0^t I^2 \, \rho_e dt, \tag{23}$$

$$\Delta T = \int_0^t I^2 \, Rdt \Big/ mc_{v.} \tag{24}$$

Finally, it is possible to derive the linear thermal expansion of the wire using,

$$\Delta L = L_0 \alpha_e \Delta T, \tag{25}$$

where L_0 is the initial length of the wire and α_e the linear thermal expansion coefficient of aluminum. Furthermore, the third wire for the A_{11} element gave us empirical evidence of Equation (25).

To develop the temperature analysis of the results, α_T was fixed at a constant value instead of considering its real variable value with respect to temperature. This assumption allows us to predict temperature values above their real estimates, especially for the high current shots. Setting the resistivity to a constant value, underestimates the temperature. The actual value is between these two estimates.

A. ELEMENT A_{12}

For this configuration, we obtained no relevant information. As shown in Table 3, the test was repeated nine times; however, only seven shots were recorded due to challenges in collecting data. Only one test sample was used. The wire's length was $l = 70\,mm$, and diameter $d = 18\,mm$. The aspect ratio (l/d) of the wire was of 3.8. Because of the aspect ratio of this sample, the R value was much smaller than that of the other wires, with aspect ratios ten times or more due to their diameter being 1.25 mm. Also because of the larger mass of the sample, the ΔT (Eq. 21) and ΔL (Eq. 22) values were much lower.

Figure 37 and Table 5 show the numerical results for each of the seven recorded shots. The first eight shots were conducted regularly, and the second shot caused the burning of the conductor that covered the O-rings (see description in Chapter IV, Figure

28). The kinks in the current pulse curve, past the peak value, starting around 500 V, are indicative of damage to the conductor of the O-rings and possible arcing at the coupling points. No further analysis is made on this part of the experiment.

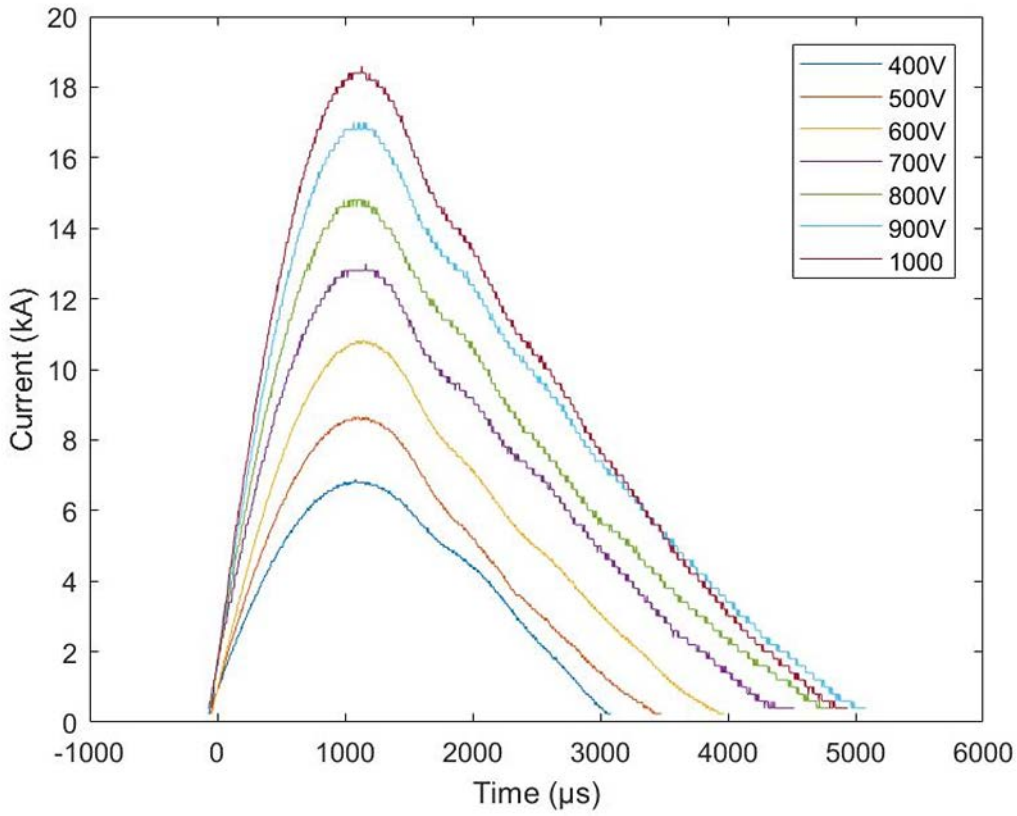

Figure 37. A_{12} element Current vs. Time

Table 5. A_{12} element results

1st wire	Voltage (V)	Peak Current (A)	ΔT (K)	Tmax (K)	ΔL (mm)
3rd shot	400	6,880	0.01	293	1e-5
4th shot	500	8,640	0.01	293	3e-5
5th shot	600	10,800	0.02	293	5e-5
6th shot	700	13,000	0.04	293	7e-5
7th shot	800	14,800	0.05	293	9e-5

B. ELEMENT A_{11}

As shown in Chapter IV, Table 2, the test was repeated eight times, using three different wires. The first two wires had “clamped ends” while the last one is considered as a “one clamped and one free end.” They all had a length of $l = 71\ mm$ and diameter $d = 1.25\ mm$. The aspect ratio (l/d) of the wires was of 56.8.

1. A_{11} First Wire

Figure 38 and Table 6 show the current pulse and numerical results, respectively, for each shot. The first three shots were conducted regularly and the fourth shot caused the explosion of the wire. From Figure 38, we can see the change on the fourth shot curve profile past the peak; this is evidence of the wire disintegrating and arcing, resulting in a higher impedance plasma conduction path. The time of the arcing happened around 1700 μs after the peak of the discharge. This phenomenon can be seen also from Figure 40. In this case the temperature plot shows an unbounded growth beginning around the same time. On the other hand, Figure 39 shows the temperature plot for the first three shots. There is an important temperature difference between the first and second shot and the third shot. This is because, as shown in Equation (22), resistivity increases as a function of temperature. Thus, the slope of the curve depends on $\Delta T/\ \Delta\tau$. Also, the exact temperature values for the fourth shot were not predictable, as can be seen from Figure 40.

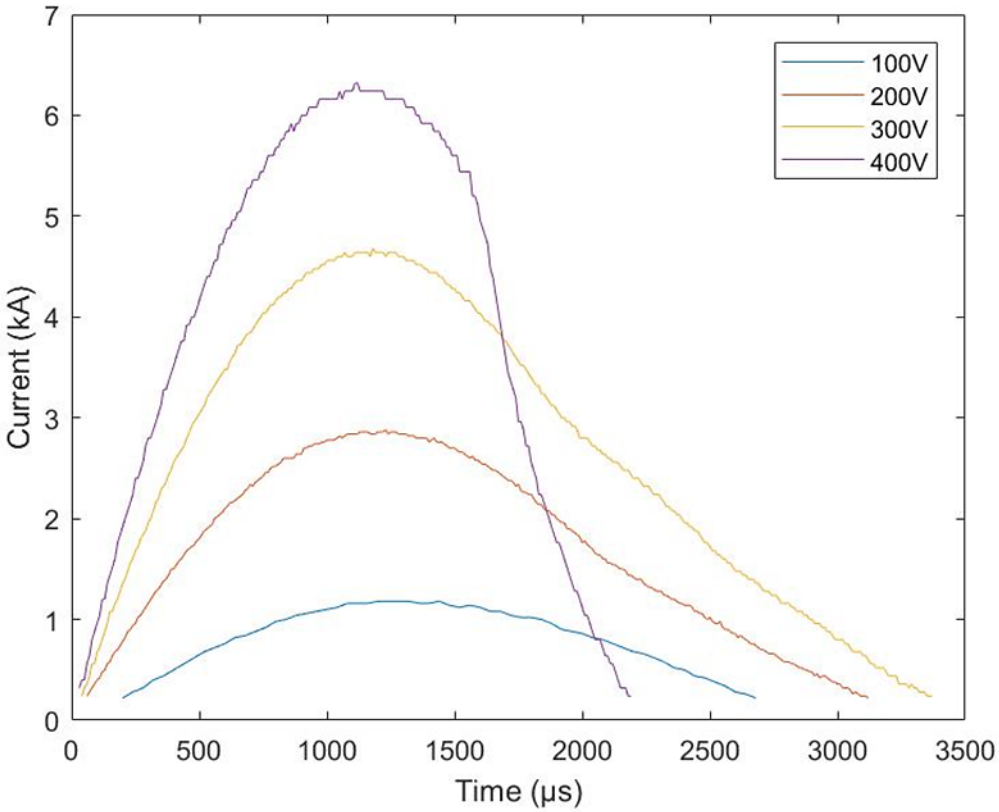

Figure 38. A_{11} element, first wire. Current vs. Time

Table 6. A_{11} element, first wire results

1st wire	Voltage (V)	Peak Current (A)	ΔT (K)	Tmax (K)	ΔL (mm)
1st shot	100	1180	14	307	0.02
2nd shot	200	2880	112	405	0.18
3rd shot	300	4680	1033	1326	1.7
4th shot	400	6320	-	-	-

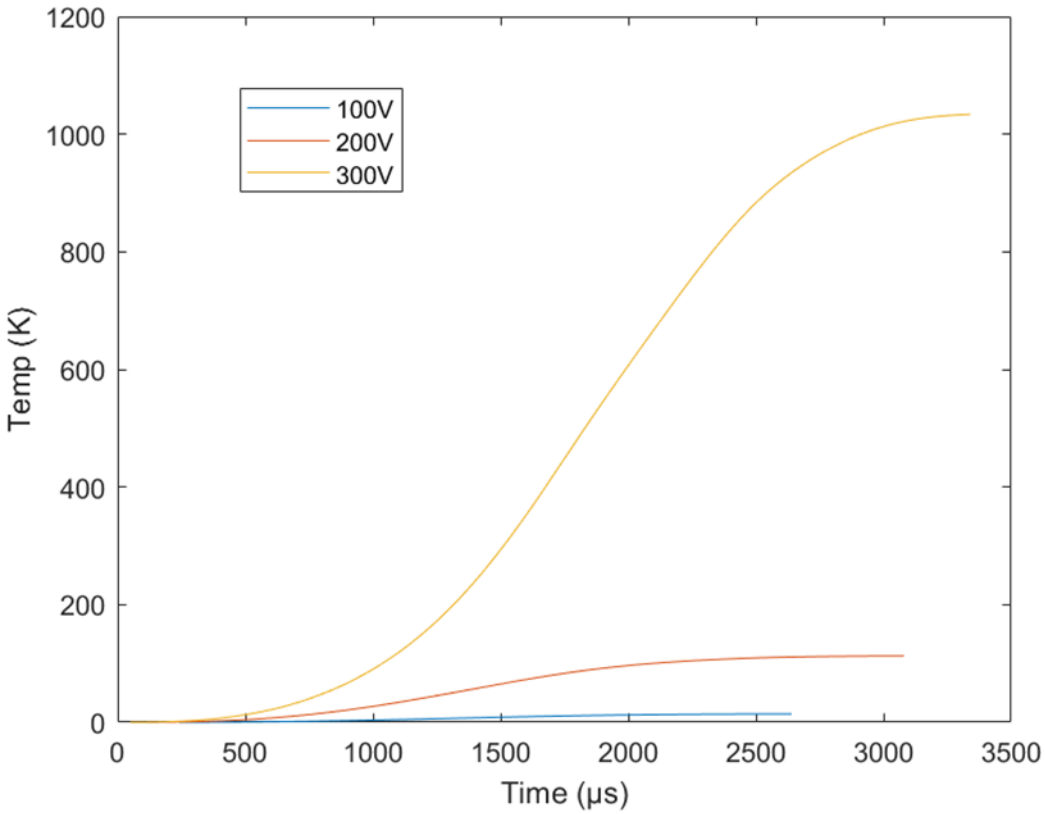

Figure 39. A_{11} element, first wire, first three shots. Temperature vs. Time

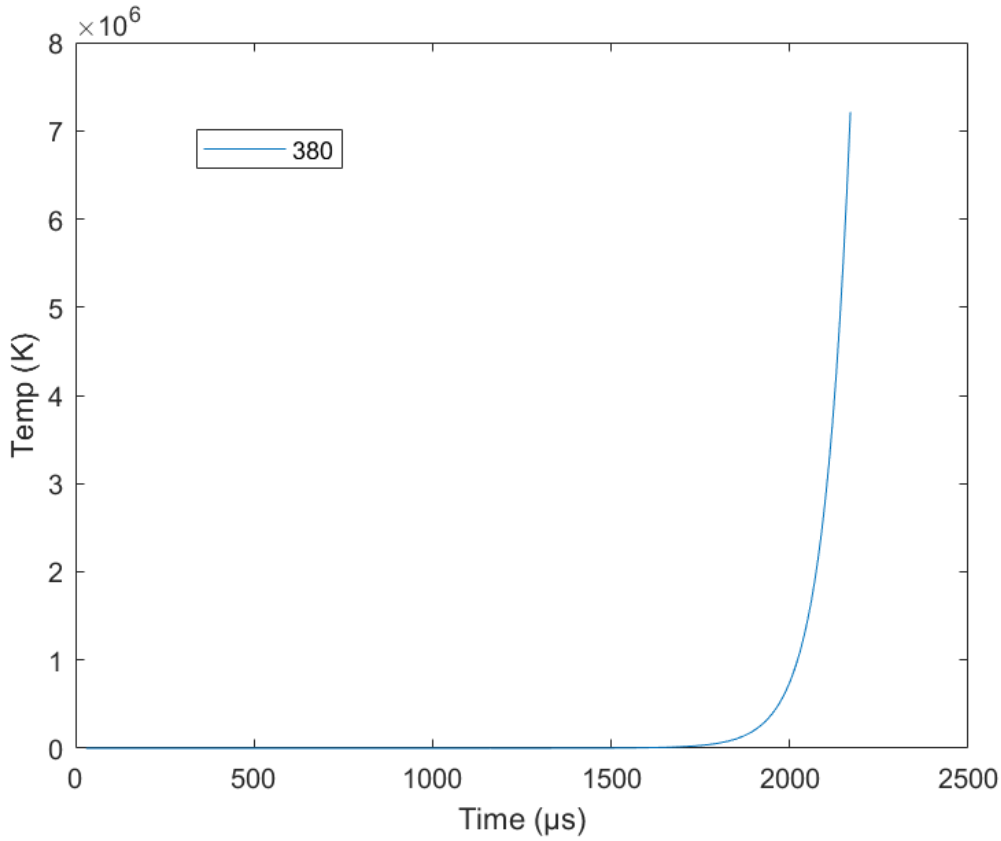

Figure 40. A_{11} element, first wire, last shot. Temperature vs. Time

In Table 7, we present data taken from the video analysis software. The analysis was done during the first 6,000 μs after the wire started to oscillate, which implies the first 1200 frames for a 200,000 fps. Max X is the maximum deflection in millimeters during this period, τ is the time at which the deflection was measured, wave cycles is the number of cycles counted at that position during the first 6,000 μs. Finally, X/L is the deflection normalized with respect to the length, and z/L is the position of the deflection along the wire's axis. All these variables are important parameters for the comparison of this work to the work of Molokov and Allen (2001).

Table 7. A_{11} element, first wire results, video analysis

1st wire	Voltage (V)	Max X (mm)	τ (μs)	X/L	z/L	Wave Cycles
1st shot	100	~0.2	-	0.002	0.5	-
2nd shot	200	~0.4	1,000	0.005	0.5	-
3rd shot	300	3	1,200	0.04	0.5	-
4th shot	380	13	1,270	0.18	0.5	-

The first and second shots did not cause any major variations in the wire. We were able to observe a small displacement X at the middle of the wire for both of them. The movement was back-and-forth, and it was slightly bigger in the second shot. Nothing else happened. This occurred most likely because of the buckling produced by the small thermal expansion generated by the currents. However, a small bend in the wire could also drive a deflection due to the magnetic field of non-aligned current elements of the wire, or an asymmetry in the current paths in the HiCTF.

The third shot suffered the same mechanism of deformation as the other two. As shown in Figure 41, the wire buckled because of the thermal expansion, which in this case is high enough to bend the wire. On the other hand, no flexural waves were seen. Another interesting phenomenon was observed toward the end of this pulse. The black permanent marker graduations were “vaporized” from the surface of the wire. Notice that they are no longer visible in the first frame of the fourth shot.

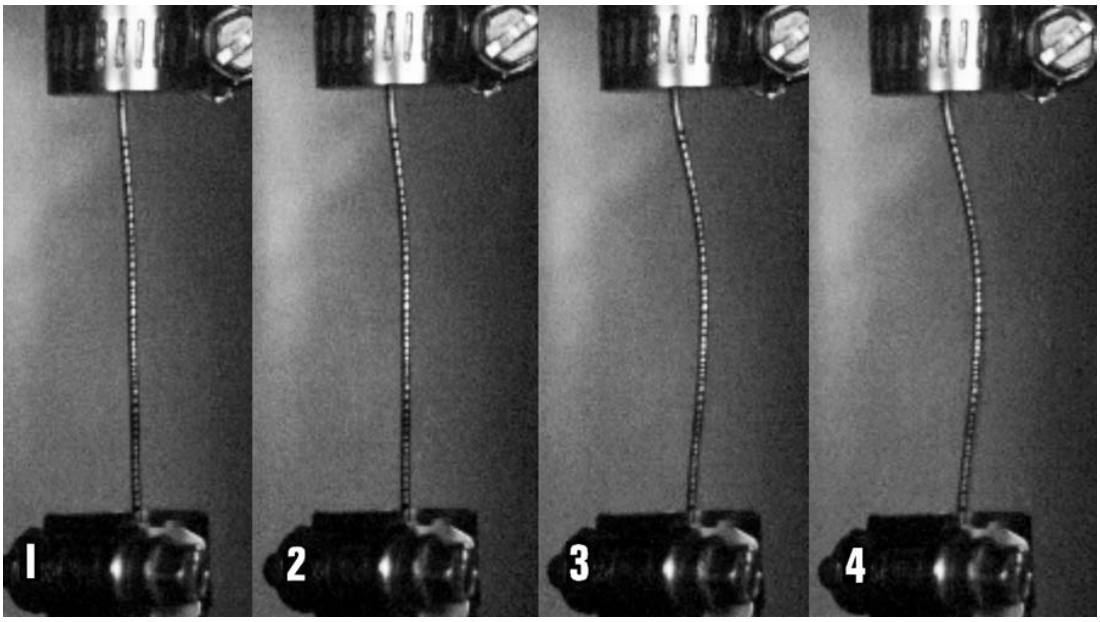

(B) (1) Shows the wire at τ = 0s. (4) Shows the wire at τ = 1200 μs

Figure 41. A_{11} element, first wire, third shot

Finally, as shown in Figure 42, the fourth wire did explode after an initial deformation. We have to take into account that this wire was initially bent from the previous shot. Also, as we calculated before, its temperature was close to aluminum's melting point. The discharge and the first spark occurred at 1350 μs. This case shows an initial buckling with a maximum X displacement of 13 mm due to thermal expansion, which occurs at the middle of the wire as expected. Moreover, in the following 80 μs, another buckling event appears near the upper end of the wire, which finally causes the wire to break. This second instability could have been influenced by the thermal expansion ongoing at the moment, but also by the magnetic force due to the bent wire, which at this point becomes a factor to take into account. Another interesting fact shown in the video images is that almost at the time when the highest temperature is predicted to occur, the wire starts to deform in a really strange way. It is in fact very similar to Figure 18 of this thesis, which shows Nasilowski's results of one of his experiments. Yet, as Lukyanov and Molokov (2001) have said, it can also be explained by the dominance of the higher mode waves, which shape the wire in a "rather intricate form" (p. 1547).

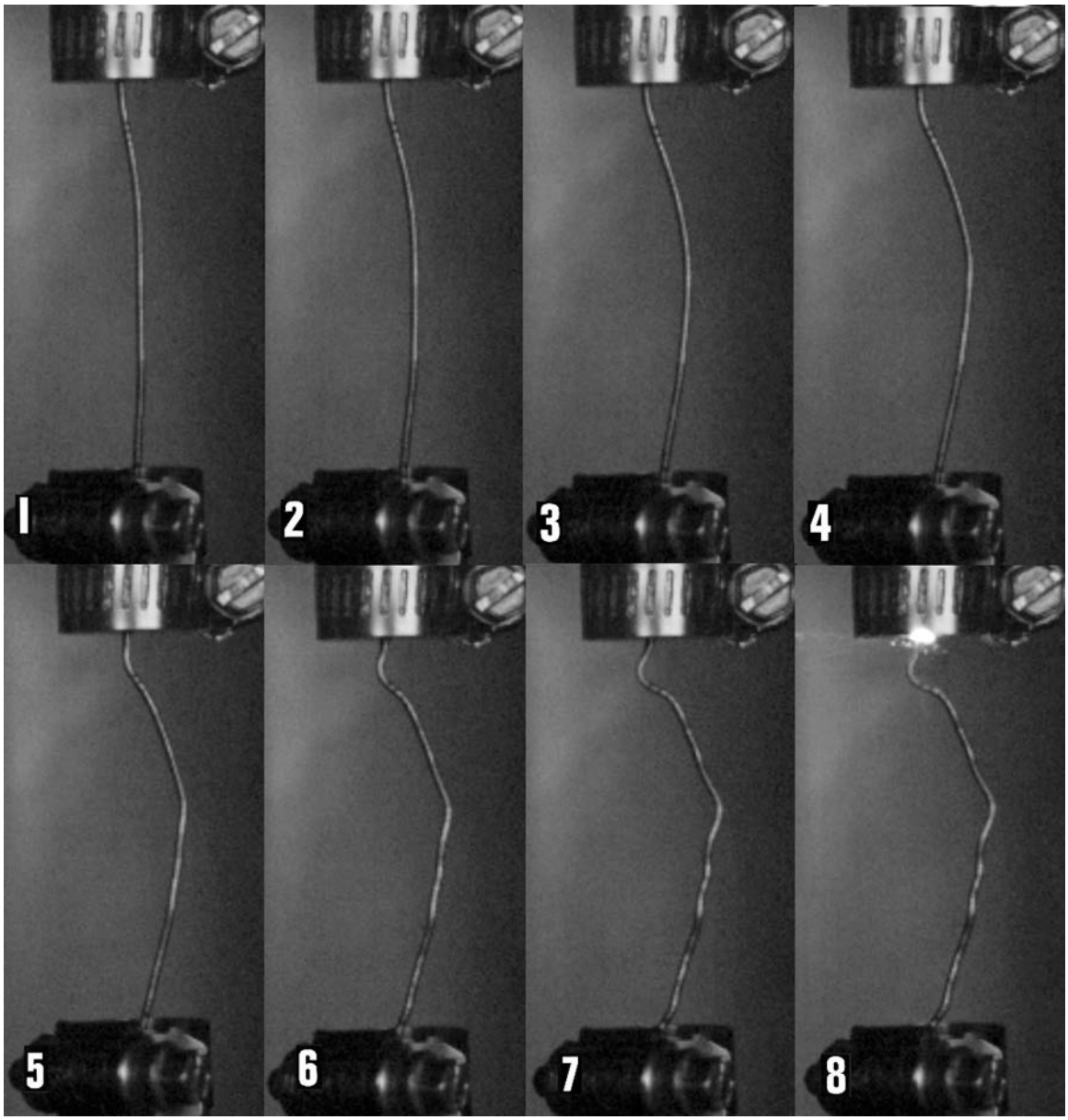

(C) (1) Shows the wire at τ = 0s. (8) Shows the wire at τ = 1350 μs

Figure 42. A_{11} element, first wire, fourth shot

2. A_{11} Second Wire

Figures 43 and 44 and Table 8 show the current pulse, calculated temperature, and numerical results for each shot, respectively. The current pulse and temperature profile for the second shot are evidence of contact loss, arcing, and the explosion of the wire. This event occurred at about 1800 μs after the beginning of the discharge.

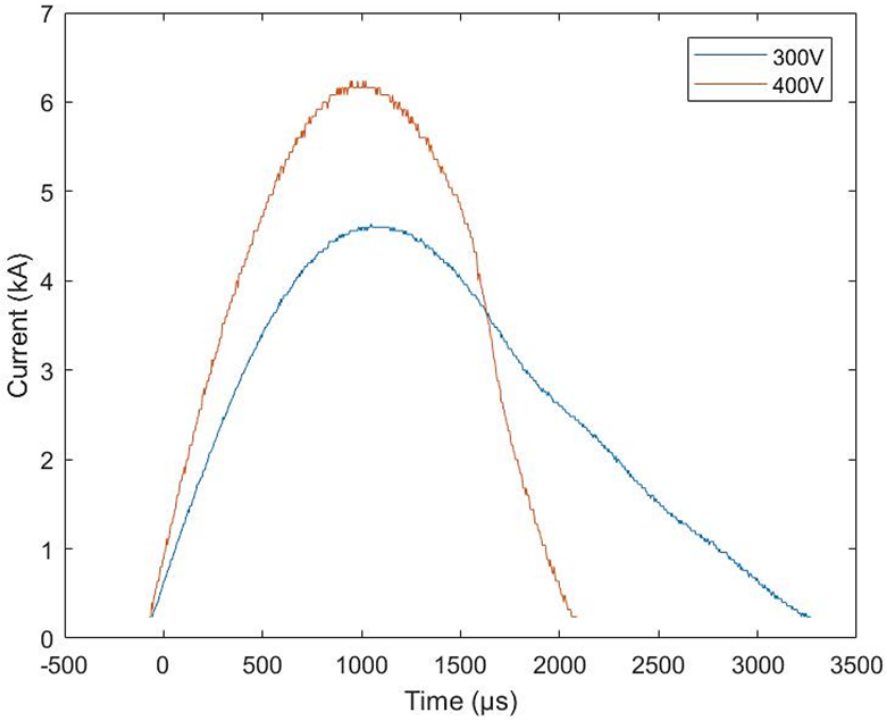

Figure 43. A_{11} element, second wire, Current vs. Time

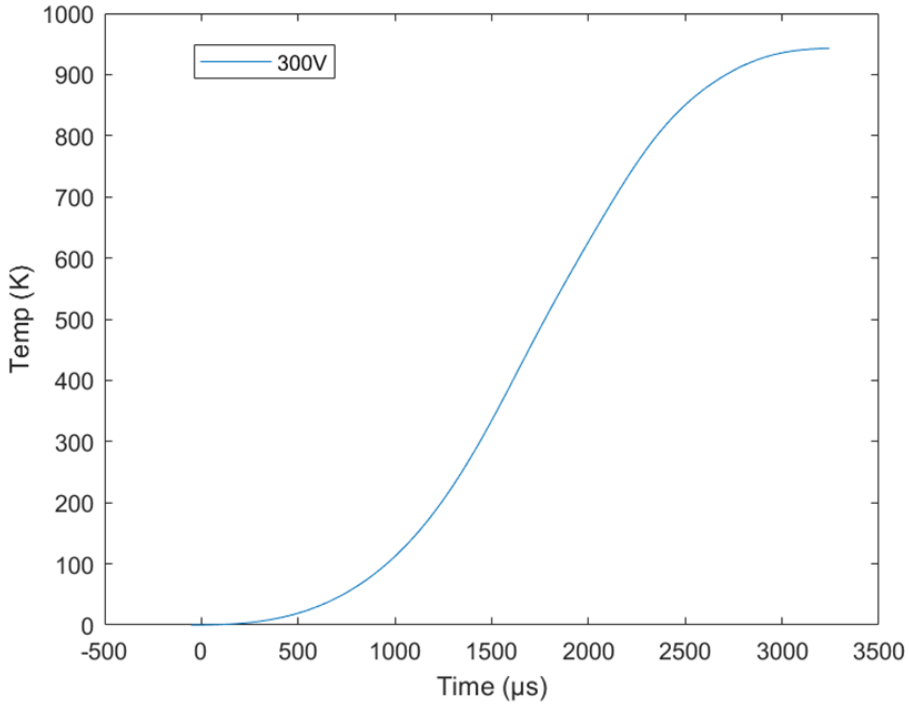

Figure 44. A_{11} element, second wire, 1st shot. Temperature vs. Time

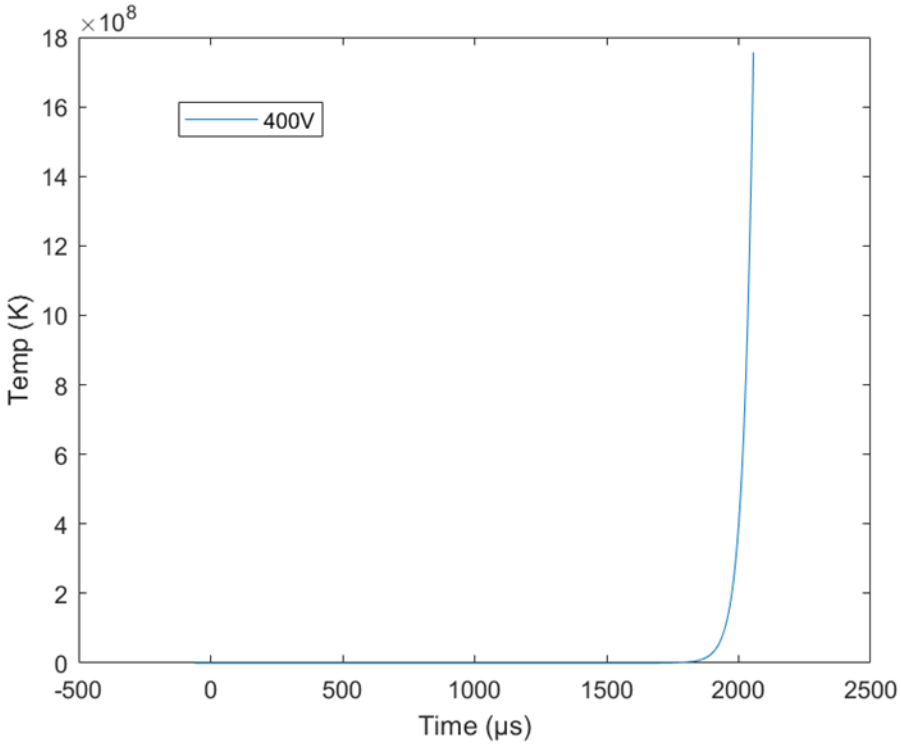

Figure 45. A_{11} element, second wire, 2nd shot. Temperature vs. Time

Table 8. A_{11} element, second wire results

1st wire	Voltage (V)	Peak Current (A)	ΔT (K)	Tmax (K)	ΔL (mm)
1st shot	300	4,640	942	1,235	1.57
2nd shot	400	6,240	-	-	-

In this case, we do not present any analysis of the wave development along the wire. As can be seen from Figures 46 and 47, there were no waves detected. This happened most likely because of the presence of different markers that we placed on the wire in order to test the camera resolution. For example, the plastic bead could be heavy enough to prevent the flexural waves from developing. Even so, we were able to observe a displacement in the z-axis on the first shot, which allowed us to calculate the wire's thermal expansion using the DICT software. The result was 0.95 mm, which is close to what the theory predicted. (However, since α_e depends on temperature, our estimates are larger than

the observed value.) The second shot created a big explosion, disintegrating the aluminum, which was later found melted all over the surfaces around the test area.

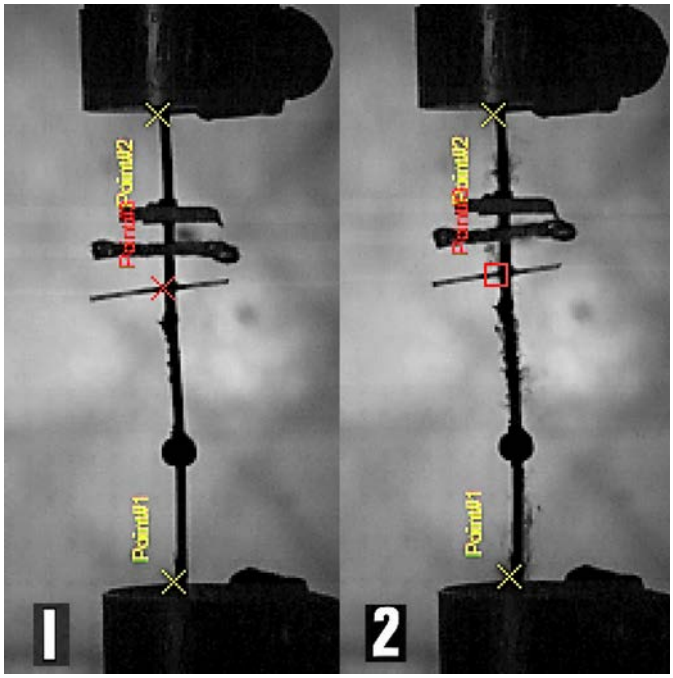

Figure 46. A_{11} element, second wire, first shot

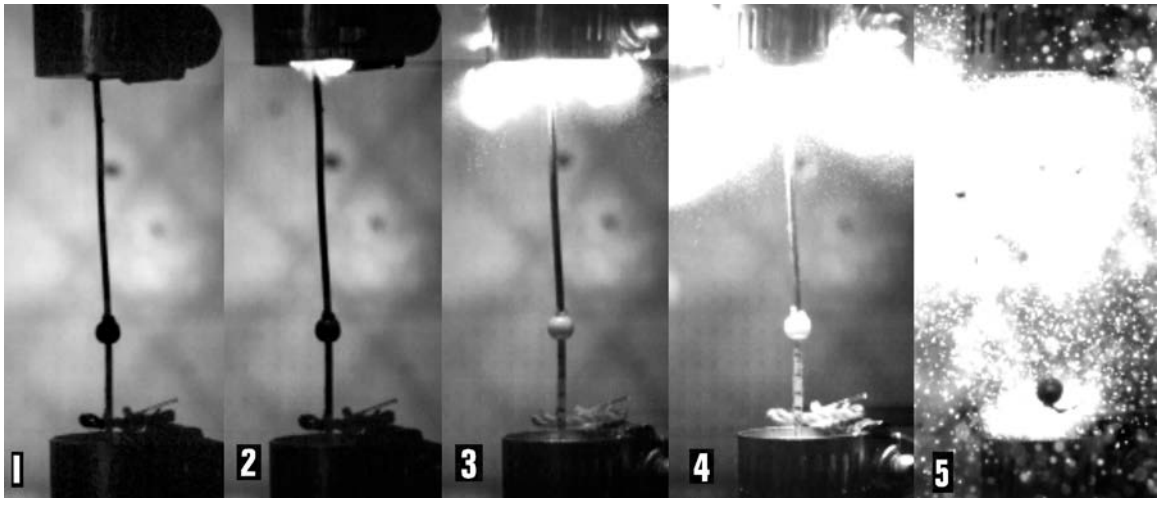

Figure 47. A_{11} element, second wire, second shot

3. A_{11} Third Wire

Figure 48 and Table 9 show the current pulse and numerical results, respectively, for each shot. These shots are considered to be under the condition of "one clamped and one free end" because after the second wire explosion, one of the terminals became seriously deteriorated and could not clamp the wire. Both shots were conducted regularly without explosions but with the presence of electric arcs on the free ends. From Figure 48 we can see the shape of the current pulse, which indicates a smooth discharge along the wire. The most interesting analysis of the plot is the comparison that can be made between the 200 V discharge of the first wire with "clamped ends" and the 200 V shot of this wire. We can see that the current in this wire was 200 A less. This happened because a "free end" causes plasma, for which impedance is much higher.

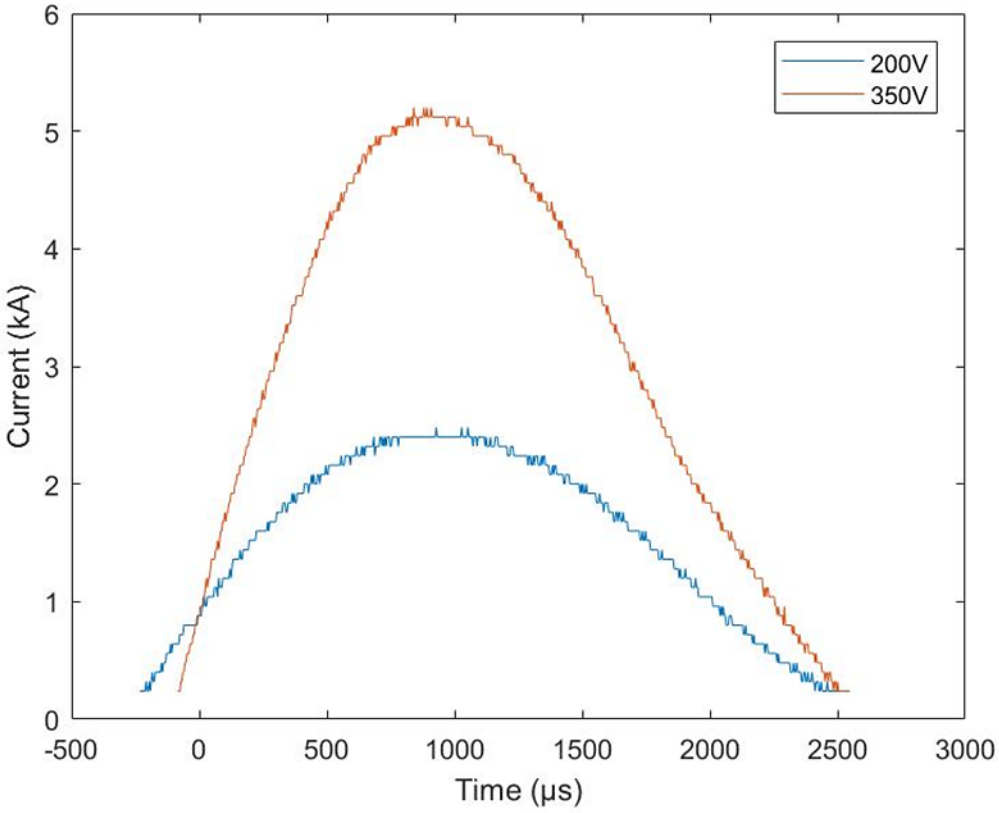

Figure 48. A_{11} element, third wire. Current vs. Time

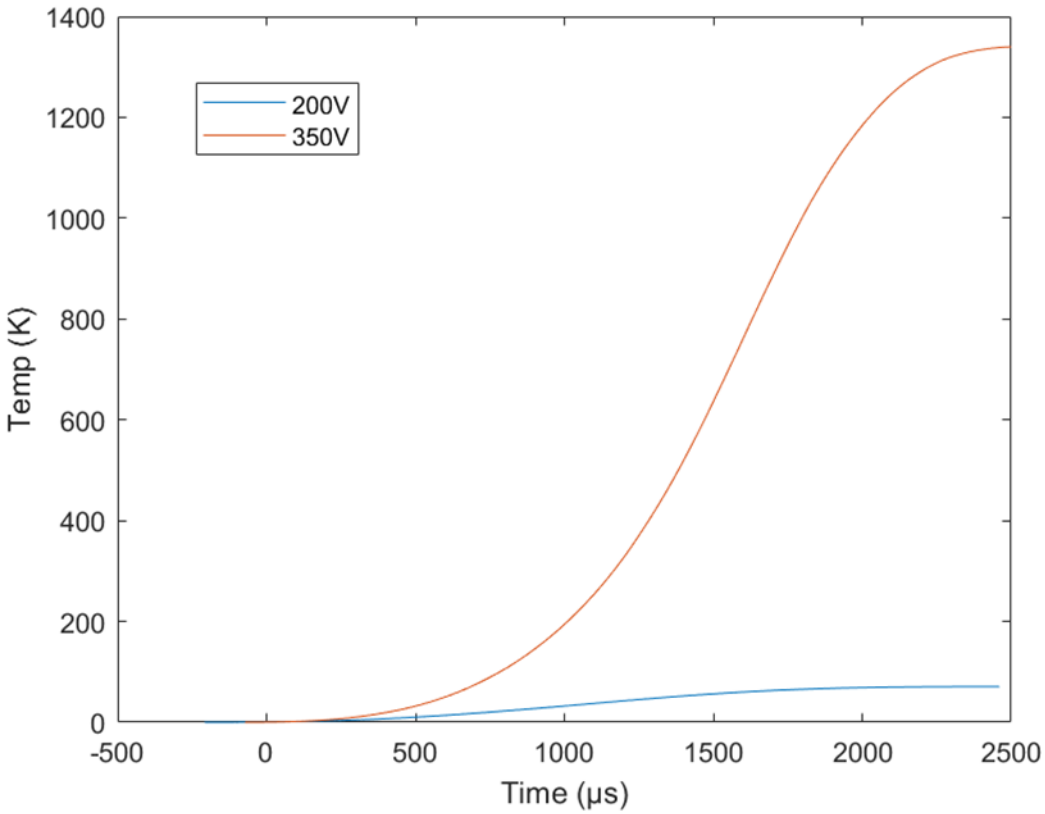

Figure 49. A_{11} element, third wire. Temperature vs. Time

Table 9. A_{11} element, third wire results

3rd wire	Voltage (V)	Peak Current (A)	ΔT (K)	Tmax (K)	ΔL (mm)
1st shot	200	2480	70	363	0.11
2nd shot	350	5200	1339	1632	2.23

In this case, we do not present any analysis on the wave development along the wire either, because no waves were detected. The possible explanation is the fact that this case was considered as a “one clamped, one free end” wire. As we said before, the explosion during the last shot of the A_{11} second wire opened a big hole in the upper holding piece.

C. ELEMENT A_{21}

As shown in Table 4, the test was repeated eight times. Three different wires were used.

1. A_{21} First Wire

The first wire's length was $l = 233\ mm$, diameter $d = 1.25\ mm$. The aspect ratio (l/d) of the wires was of 186.4. Figure 50 and Table 10 show the current pulse and numerical results, respectively, for each shot. The fourth shot caused the rupture of the wire on its bottom end. The lack of an abrupt current drop in Figure 50, however, may be evidence that the wire broke after the discharge was over. As we will see later, the 400 V, 2400 µs long shot caused the fragmentation of the wire, while the 390 V, 2,800 µs long shot did not. Therefore, the fact that the 380 V shot pulse duration is around the 3,000 µs is evidence that the wire resisted the current discharge before it broke. Further evidence of this phenomenon is presented with the video and microscope images.

In Figures 51 and 52 we can see the temperature profile of the wires. Also in this case, it can be seen how the fourth shot profile increases rapidly with respect to the other three shots. On the other hand, it does not have the unbounded growth seen in the previous temperature profiles of some of the wires that actually explode. As stated before, even if the temperature values are overestimated, the qualitative analysis provides the correct temperature rate trends.

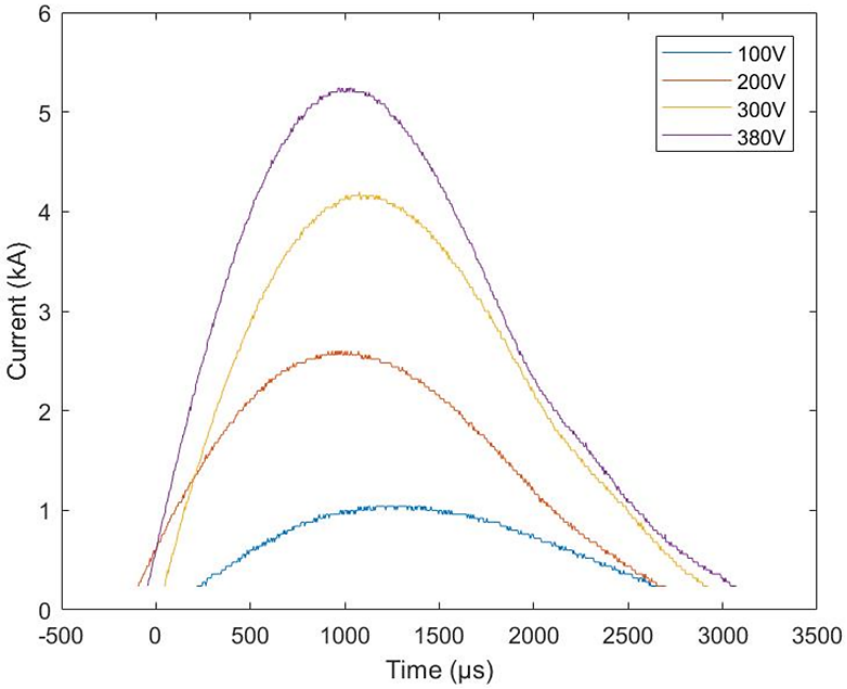

Figure 50. A_{21} element, first wire. Current vs. Time

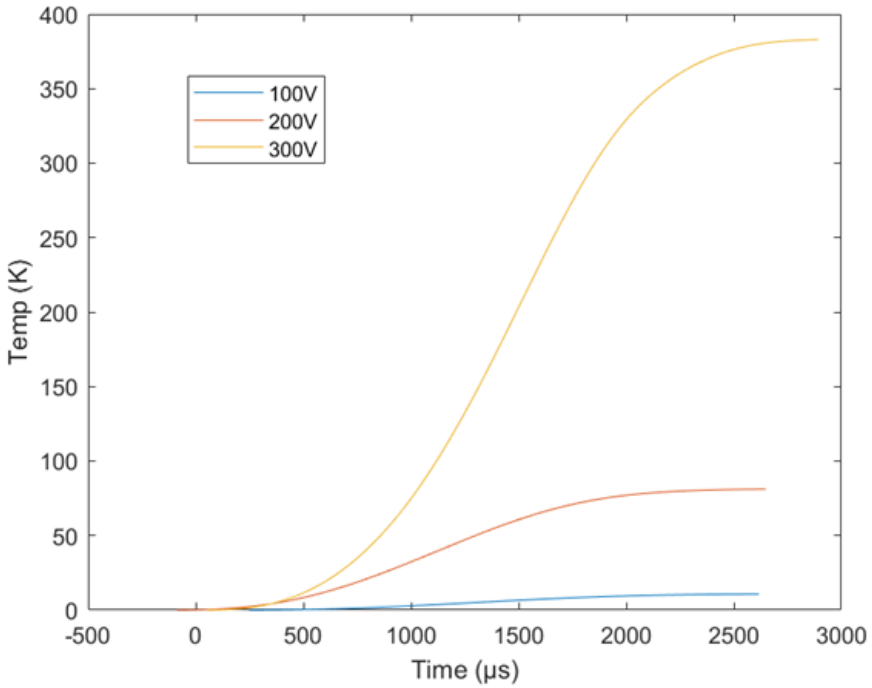

Figure 51. A_{21} element, first wire, first three shots. Temperature vs. Time

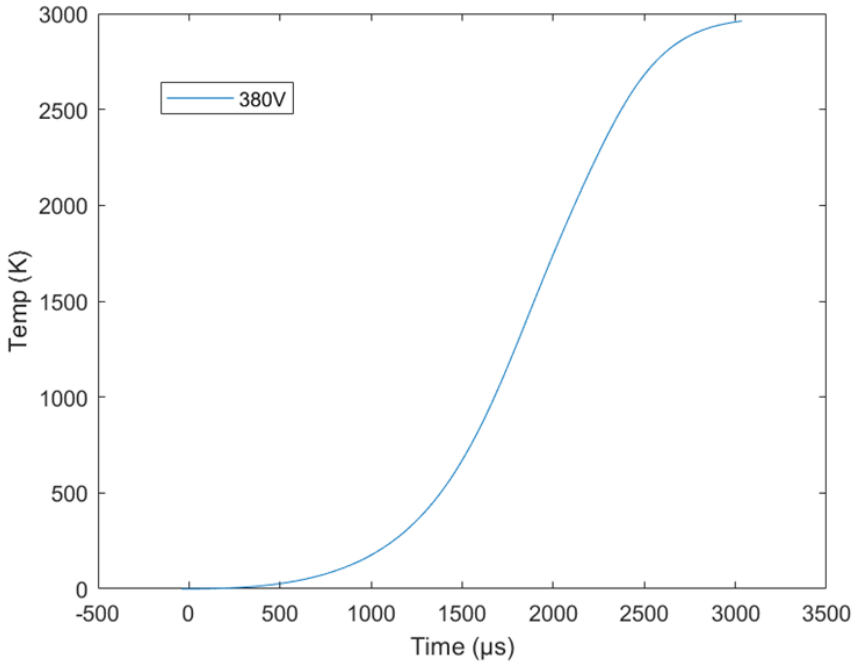

Figure 52. A_{21} element, first wire, last shot. Temperature vs. Time

Table 10. A_{21} element, first wire results, current profile analysis

1st wire	Voltage (V)	Peak Current (A)	ΔT (K)	Tmax (K)	ΔL (mm)
1st shot	100	1,040	11	304	0.06
2nd shot	200	2,600	81	374	0.44
3rd shot	300	4,200	382	675	2.07
4th shot	380	5,240	2,961	3,254	16

In Tables 11, 13, and 15, we present data taken from the video analysis software. The analysis was done during the first 25,000 μs after the wire started to oscillate, which implies the first 1,200 frames for a 200,000 fps. Max X is the maximum deflection in millimeters during this period, τ max is the time at which the deflection was measured, wave cycles is the number of cycles counted at that position during the first 25,000 μs (in this case we are counting the peaks of the predominant modes). Finally, X/L is the deflection normalized with respect to the length, and z/L is the position of the deflection along the wire's axis. These two parameters will be important to compare our experimental results to those of Lukyanov and Molokov (2001).

Table 11. A_{21} element, first wire results, video analysis

1st wire	Voltage (V)	Max X (mm)	τ max (μs)	X/L	z/L	Wave Cycles
1st shot	100	1	17,130	0.005	0.51	7
2nd shot	200	1.8	3,900	0.008	0.5	30
3 rd shot	300	2.8	3,000	0.013	0.53	4
4th shot	380	2.8	25,000	0.013	0.5	1

In Figure 53, we show two screenshots of the high-speed video from the A_{21} element's first shot. The image shows the maximum displacement X of the wire, which occurs 17,130 μs after the wire starts to show movement, measured from almost the center of the wire. In the video it is possible to observe what looks like the first flexural mode along the wire. The wave has a period of approximately 4,000 μs (as observed in the video images and is consistent with the number of cycles counted on a 25,000 μs period).

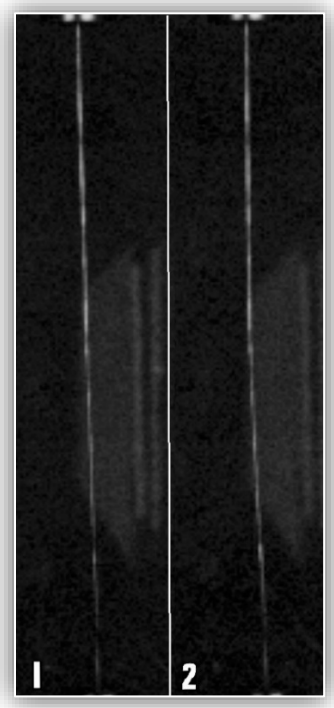

(D) (1) Shows the wire at τ = 0s. (2) Shows the wire at τ = 17130 μs

Figure 53. A_{21} element, first wire, first shot. Maximum X displacement

Figure 54 shows eight snapshots of the high-speed video for the 200 V A_{21} element shot. In this case, we observed high frequency vibration during the first 10,000 μs (the amplitudes were very low as shown in Figure 54, [2]). After this, a second flexural mode acquired predominance in the wire and continued for as much as 0.3 s. The 30 Wave cycles shown in Table 11 were counted from when the second mode became predominant. Once again, the highest X displacement occurred at the center of the wire during the second period of vibration.

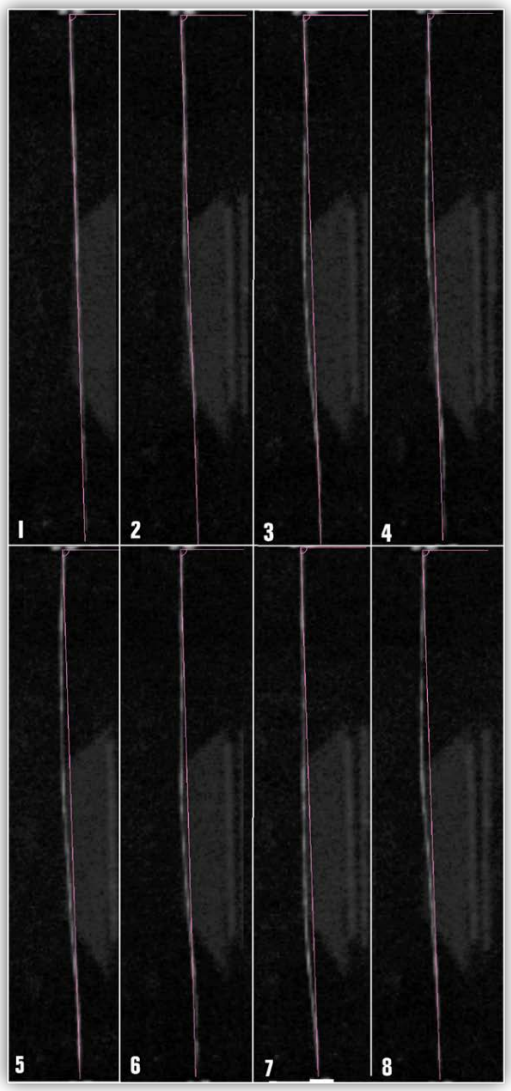

(E) The red line was placed as reference on the DICT program. (1) Shows the wire at τ = 0s. (3) Shows the wire at its maximum displacement. (2–8) Show the wire the higher X displacements.

Figure 54. A_{21} element, first wire, second shot. Maximum X displacement

The third shot is shown in Figure 55. We observed a predominant first flexural mode. Furthermore, it was possible to observe other very high frequency modes that decayed quickly after the first 5,000 μs, approximately. Only four cycles of the first mode occurred with a duration of no more than 45,000 μs. This time the higher X displacement was of 2.8 mm, once again at the center of the wire.

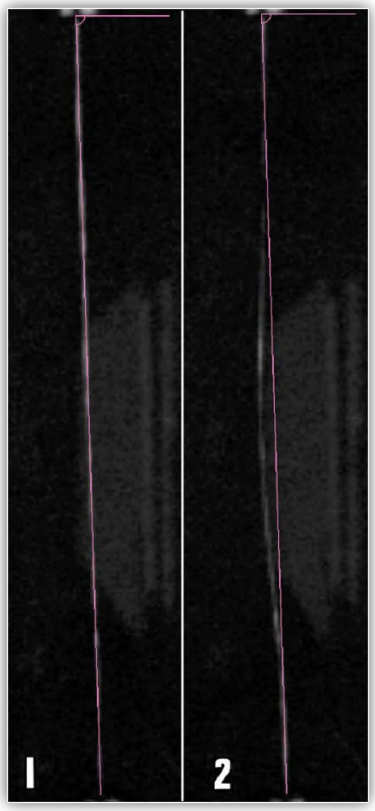

The red line was placed as reference on the DICT program. (1) Shows the wire at τ = 0s. (2) Shows the wire at τ = 3000 μs.

Figure 55. A_{21} element, first wire, third shot. Maximum X displacement

Figure 56 shows the last shot of the first wire. This shot is relevant because the wire actually broke at one of its ends. At the time of the wire rupture, and after, there was no blow off or arcing. This may be evidence of a rupture that took place after the discharge was over. The wave movement was similar to the second shot. It had a short period of high frequency modes from which only small vibrations could be appreciated, followed by a

low frequency first mode that broke the wire during its first period. The wire's rupture caused a whiplash, which can be appreciated in Figure 56, [6, 7, 8]. This happened after 45,000 μs.

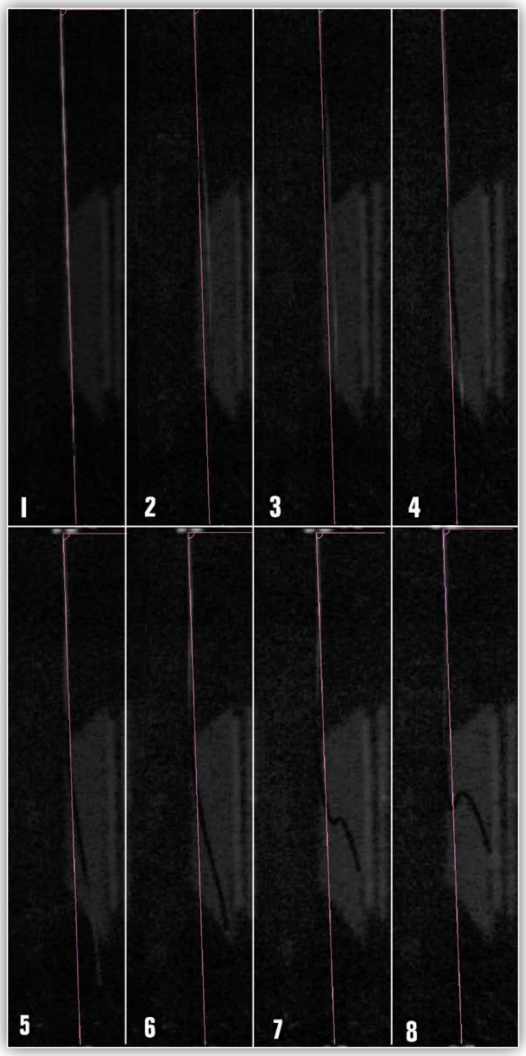

(F) The red line was placed as reference on the DICT program. (1) Shows the wire at τ = 0s. (2) Shows the wire at its maximum displacement. (4–8) Show the wire after the break on its lower end.

Figure 56. A_{21} element, first wire, fourth shot. Maximum X displacement

The two remaining pieces were taken to the laboratory and observed with an optical microscope. Figure 57 shows that there was a mechanical stress rupture. There are no signs

of plasma arcing in the video and the lack of melted surfaces confirm that this rupture happened after the current pulse.

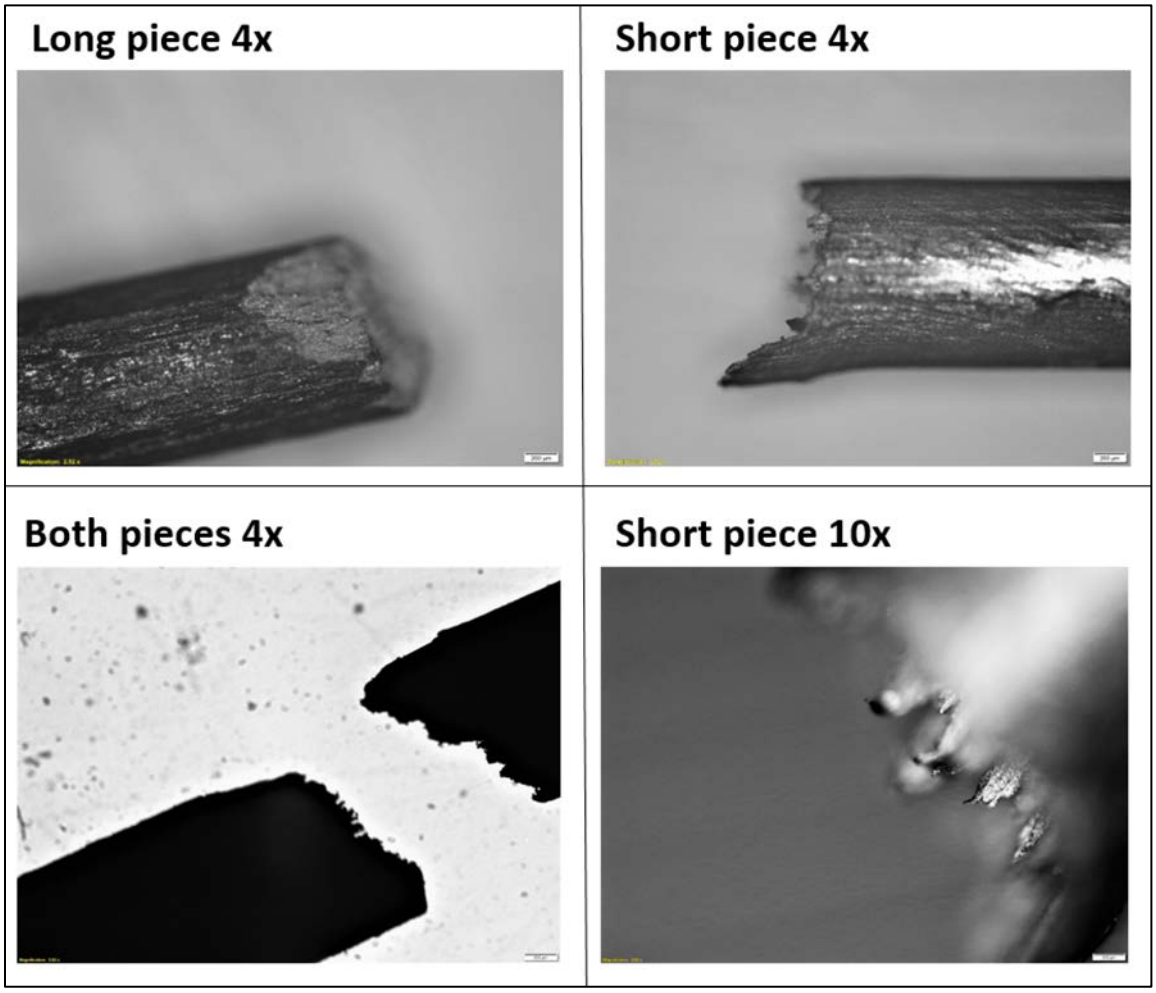

Figure 57. A_{21} element, first wire, fourth shot. Microscope analysis

2. A_{21} Second Wire

The second wire's length was $l = 229.3\,mm$ and diameter $d = 1.25\,mm$. The aspect ratio (l/d) of the wires was of 183.4. Figure 58 and Tables 12 and 13 show the current pulse and numerical results, respectively, for each shot. The third shot caused the wire to explode, generating multiple fragmentation of the wire. This is indicated by the fast drop in current in Figure 58, corresponding to 400 V. The time of the loss of contact

occurred around 1,700 µs after the beginning of the discharge. Figures 59 and 60 show the temperature profile of the shots. It can be seen that for the last shot, the temperature rises steeply. This is different if compared to other temperature plots of exploding wires. This can be connected to the fact that, in theory, multiple fragmentation happens sequentially. Therefore, impedance increases rapidly but not immediately as it does with an abrupt rupture.

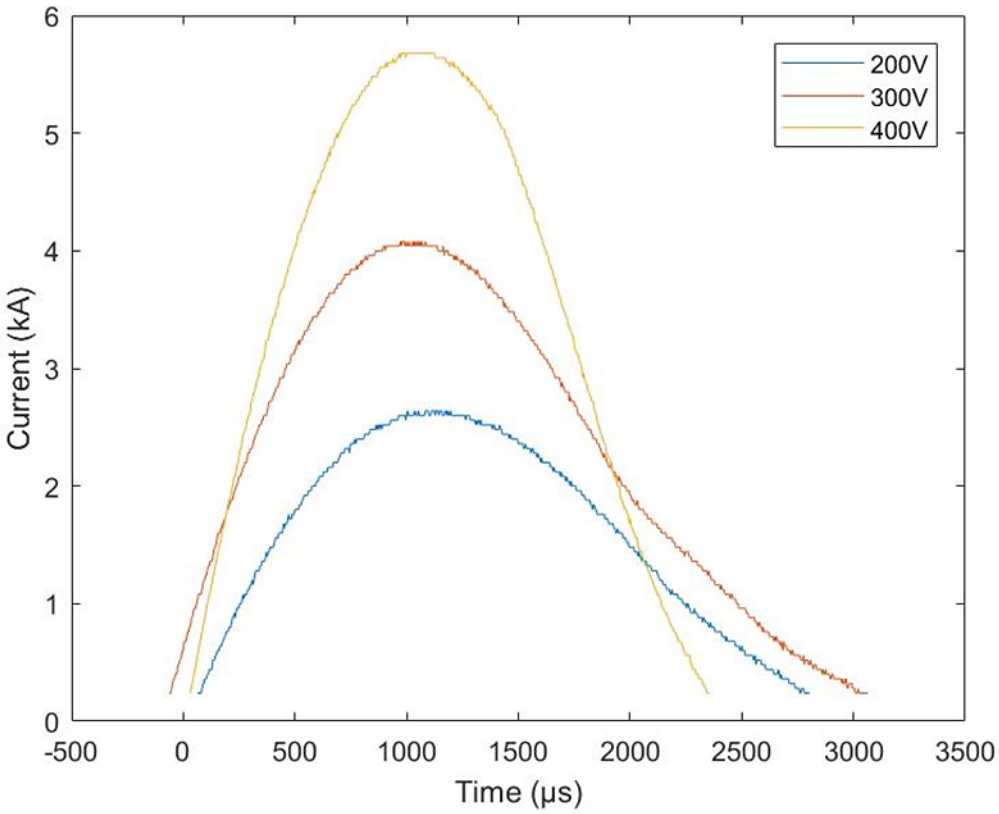

Figure 58. A_{21} element, second wire. Current vs. Time

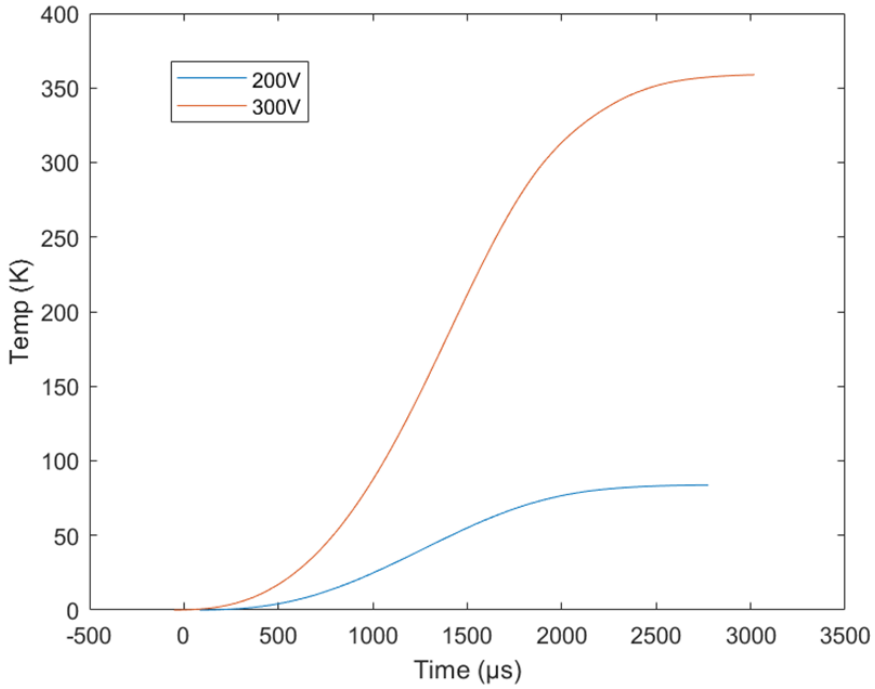

Figure 59. A_{21} element, second wire, first two shots. Temperature vs. Time

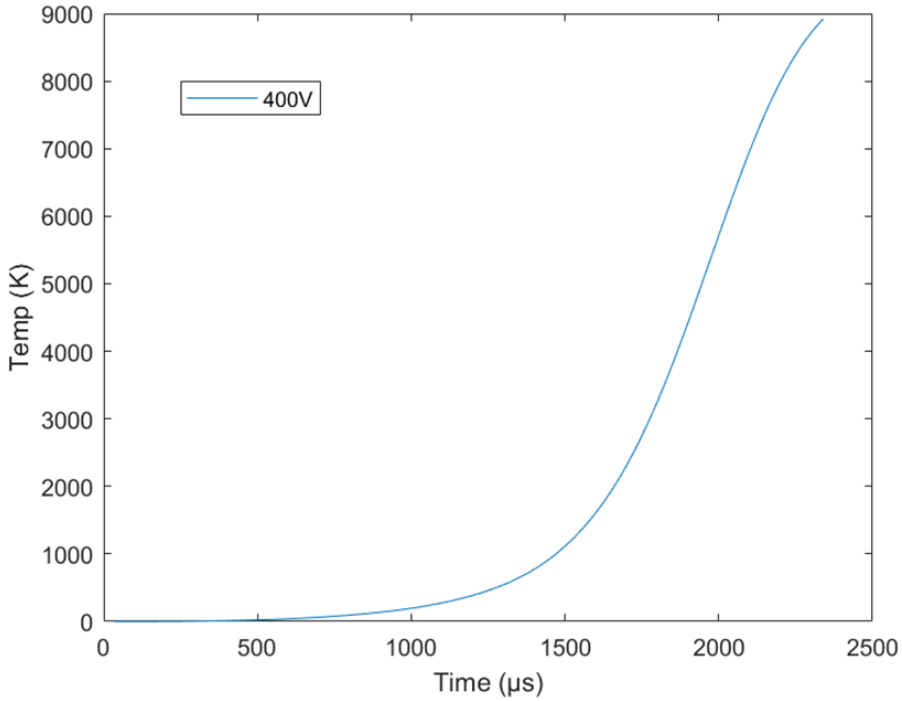

Figure 60. A_{21} element, second wire, last shot. Temperature vs. Time

Table 12. A_{21} element, second wire results

2nd wire	Voltage (V)	Peak Current (A)	ΔT (K)	Tmax (K)	ΔL (mm)
1st shot	200	2,640	83	376	0.45
2nd shot	300	4,080	358	651	1.94
3rd shot	400	5,680	8918	9,211	48.4

Table 13. A_{21} element, second wire results, video analysis

2nd wire	Voltage (V)	Max X (mm)	τ (μs)	X/L	z/L	Wave Cycles
1st shot	200	4.1	4,000	0.02	0.5	35
2nd shot	300	9	4,000	0.043	0.5	3
3rd shot	400	8	1,200	0.038	0.5	0

Figure 61 shows eight snapshots from the high-speed video recording of the A_{21} element, second wire, first shot. Note the shape of the wire before the shot. Unlike the previous shots, where the wire was overall straight along its axis, this wire was bent 1 mm to the left as seen in Figure 61, snapshot 1. This is an important fact to take into account for the instability study on this wire. The flexural waves observed were only low frequency, mostly the first flexural mode. No higher frequency waves or vibrations were identified. The maximum displacement X was detected after 4,000 μs, and while the deformation and associated temperature were large, the wire returns to its initial form. This phenomenon can be observed also between the second and third shots. Once more, the z/L value was 0.5, which is expected on a “clamped ends” wire.

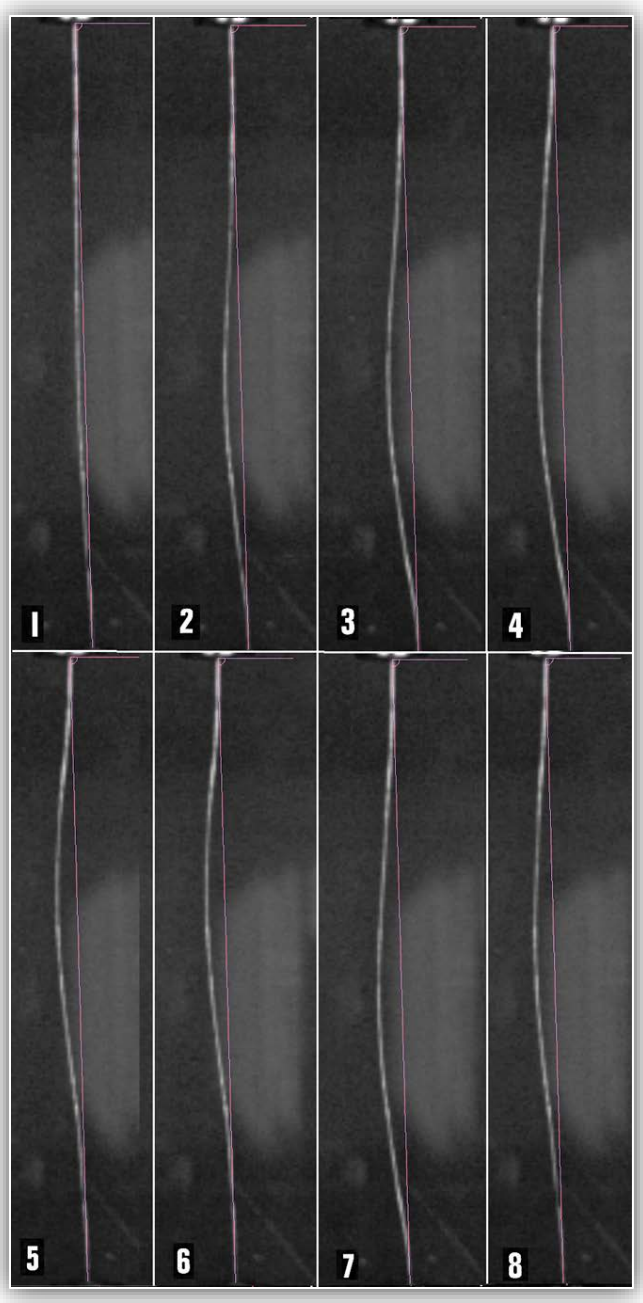

(G) The red line was placed as reference on the DICT program. (1) Shows the wire at $\tau = 0$s. (3) Shows the wire at its maximum displacement.

Figure 61. A_{21} element, second wire, first shot. Maximum X displacement

As shown in Figure 62, four snapshots of the high-speed video were taken for the A_{21} element, second wire, second shot. These images show three cycles of the first flexural

mode at less than 40,000 μs. No higher modes were observed. It is important to note that the wire was initially bent as it was for the first shot. The maximum deflection was off 9 mm and it occurred at the center of the wire.

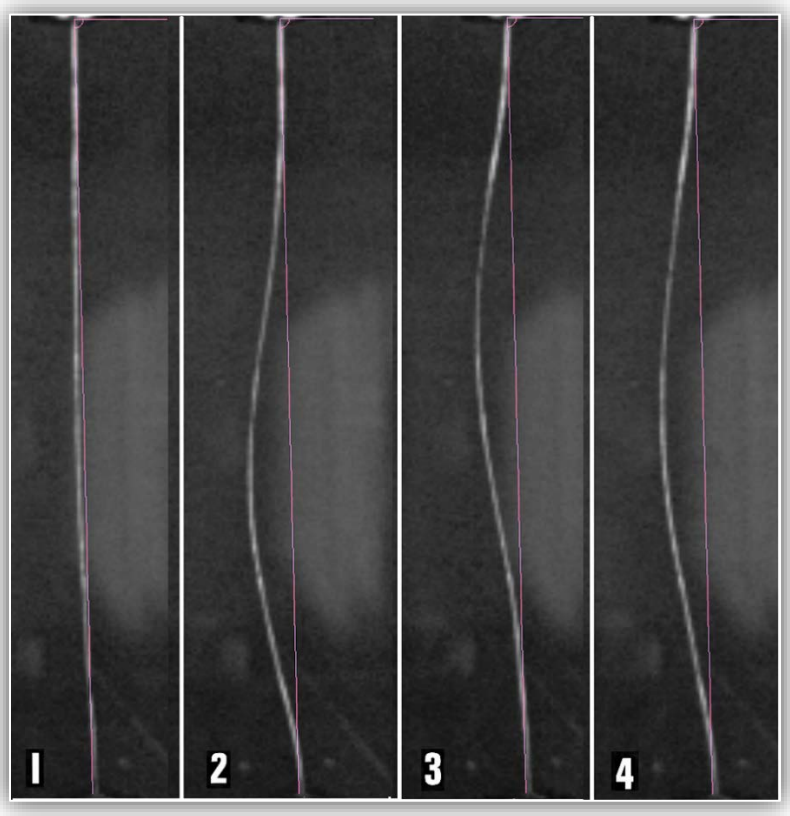

(H) The red line was placed as reference on the DICT program. (1) Shows the wire at τ = 0s. (1–3) Show first mode wave cycle.

Figure 62. A_{21} element, second wire, second shot. Maximum X displacement

Finally, the last shot of the second wire is shown in Figure 63. The third snapshot image from Figure 63 shows the exact moment of the rupture, which happened 1,200 μs after the current started to flow. This coincides with the time of the peak current. The first break happened at 37 mm from the bottom end of the wire (z/L = 0.18). On this test there was not enough time for the waves to develop. Instead, we could see the original instability revealing as an initial buckle, which finally caused the wire rupture. As Lukyanov and

Molokov (2001) describe in their work, “the maximal stress energy can be accumulated if the temperature rises sufficiently quickly” (p. 1548). They also state that fracture is most likely if the temperature gets slightly below the melting point. In this case, both conditions were satisfied.

After the first spark and successive arcing developed, the image saturated white for a time spanning 2,660 μs. After that, the image started to clear and some of the pieces can be seen flying around.

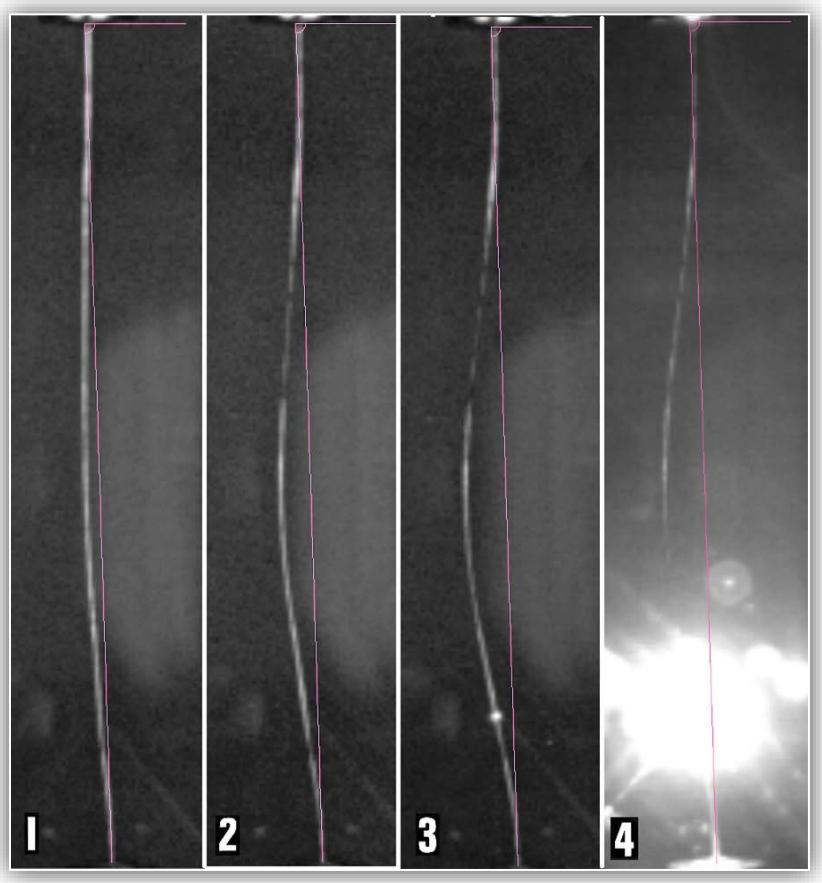

(I) The red line was placed as reference on the DICT program. (1) Shows the wire at $\tau = 0$s. (3) Shows the wire at its maximum displacement.

Figure 63. A_{21} element, second wire, third shot. Maximum X displacement

This shot caused the fragmentation of the wire in several pieces as shown in Figure 64. This is a confirmation that fragmentation occurs in successive steps, which has been cited by many authors. In Figure 65, we show the microscope images of the fragments' ends. As is evident, the first images correspond to the fragments that were involved in the initial arcing, which caused the wire to melt at those points. It seems, however, that even if some of the fragments' ends indicate plasma presence, some others are more likely to indicate purely mechanical fragmentation.

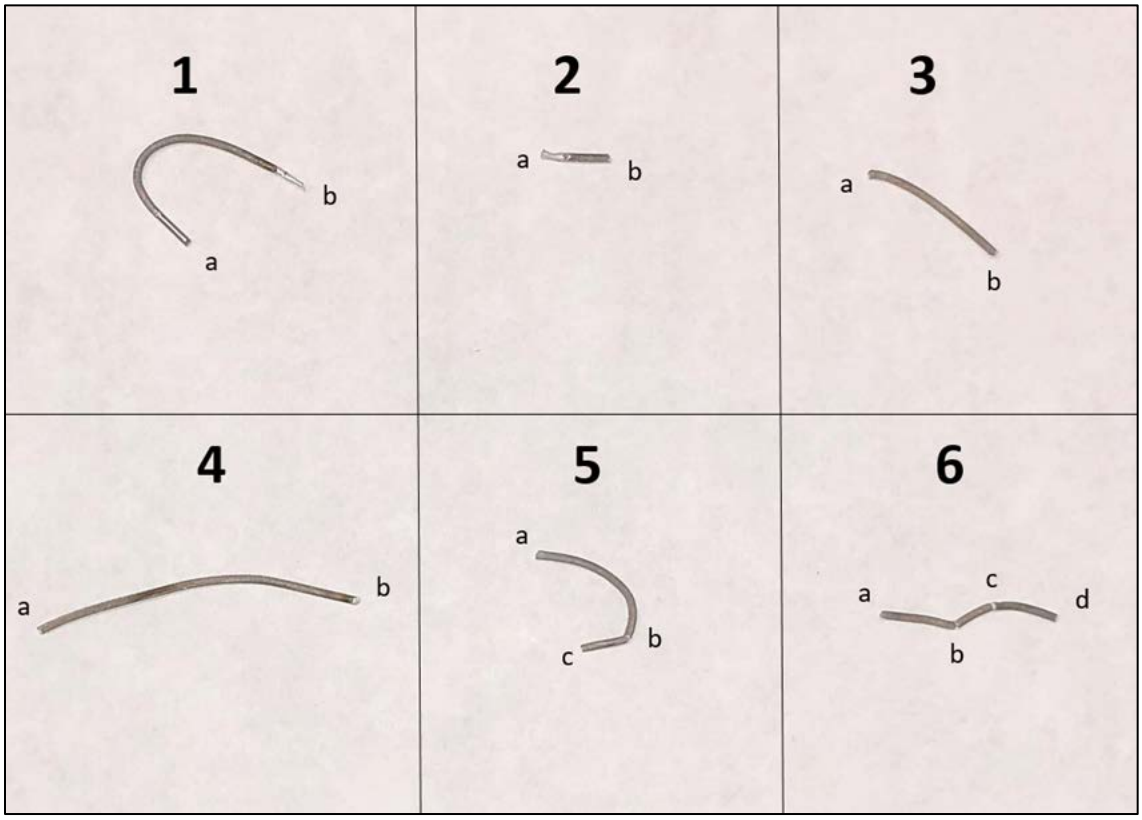

Figure 64. Wire fragments after A_{21} element, second wire, third shot explosion. Refer to Figure 65 for microscope views

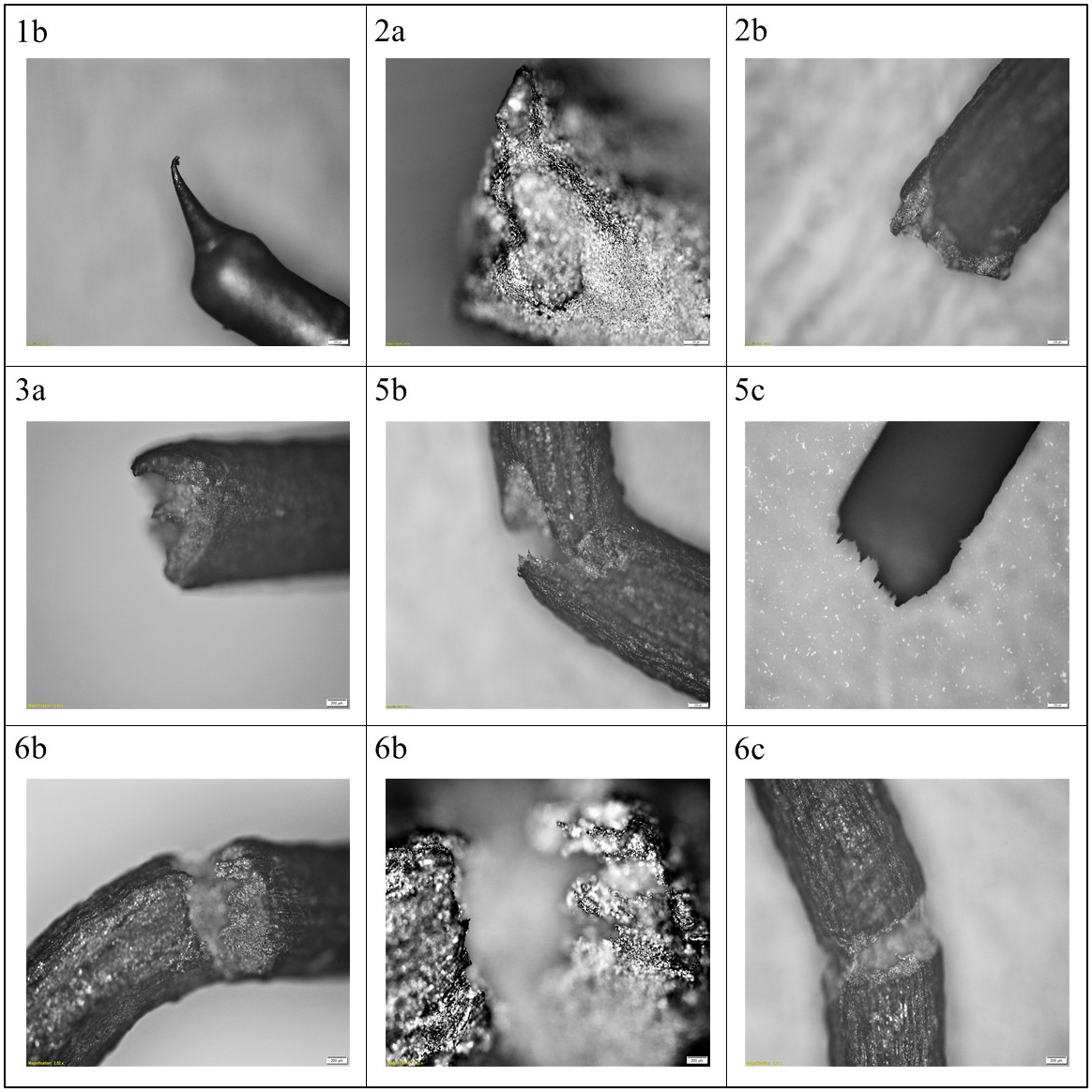

(J) [1b, 2b, 3a, 5b, 5c, 6b, 6c] Objective lens magnification 4x. [2a, 6b] Objective lens magnification 10x.

Figure 65. Optical microscope pictures of the wire fragments

3. A_{21} Third Wire

The third wire's length was $l = 231.7mm$ and diameter $d = 1.25\ mm$. The aspect ratio (l/d) of the wires was of 185.3. Figures 66 and 67, and Table 14, show the current pulse, the temperature profile, and the numerical results, respectively, for this shot. The wire did not explode or fracture. Special attention should be given to the fact that this wire

received a bigger electrical discharge than the 380 V shot of the first wire, without breaking. The causes of this phenomena can be diverse. The fact that the first wire was stressed with previous discharges is a very plausible reason. The other possible cause is related to the stress waves, which are discussed in the following paragraphs. In any event, the current pulse and temperature profile are important in the evaluation of the behavior of the exploding and non-exploding wire.

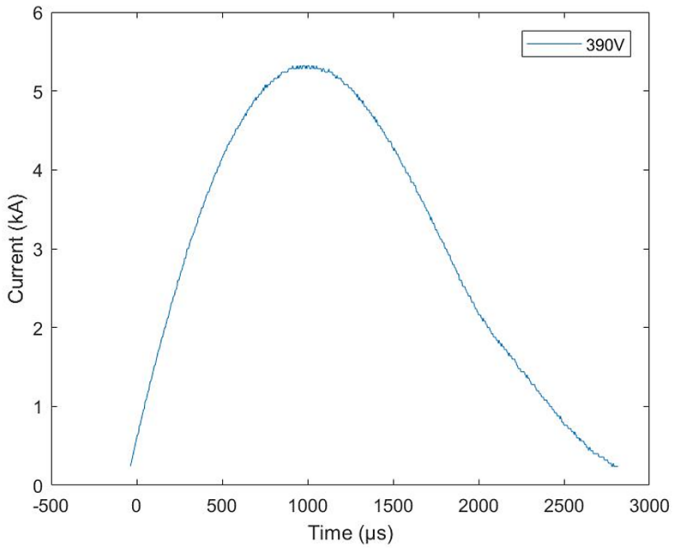

Figure 66. A_{21} element, third wire. Current vs. Time

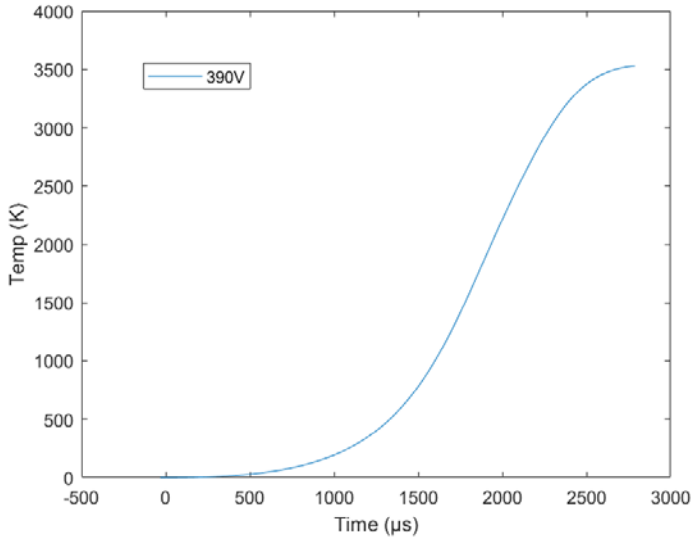

Figure 67. A_{21} element, third wire. Temperature vs. Time

Table 14. A_{21} element, third wire results

3rd wire	Voltage (V)	Peak Current (A)	ΔT (K)	Tmax (K)	ΔL (mm)
1st shot	390	5320	3530	3823	19.33

Table 15. A_{21} element, third wire results, video analysis

3rd wire	Voltage (V)	Max X (mm)	τ (μs)	X/L	z/L	Wave Cyc
1st shot	390	10	240-800	0.057	0.32-0.66	2

The third wire shot is shown in Figure 68. In this case the wire was not bent initially. We observed a second mode without the presence of other higher frequency modes. During this process, we counted two cycles. The maximum displacement was as much as 10 mm and it happened, as it was expected for a second mode, at z/L = 0.32 and 0.66. This wire did not break but got deformed from the high thermal expansion. After the test was over, the sample was recovered and measured again in the laboratory. The final length of wire was 233 mm, 2 mm longer than the initial 231 mm. Once again, the values shown in Table 14 overestimate the real values because of the assumptions of constant temperature coefficient of resistivity and constant coefficient of thermal expansion.

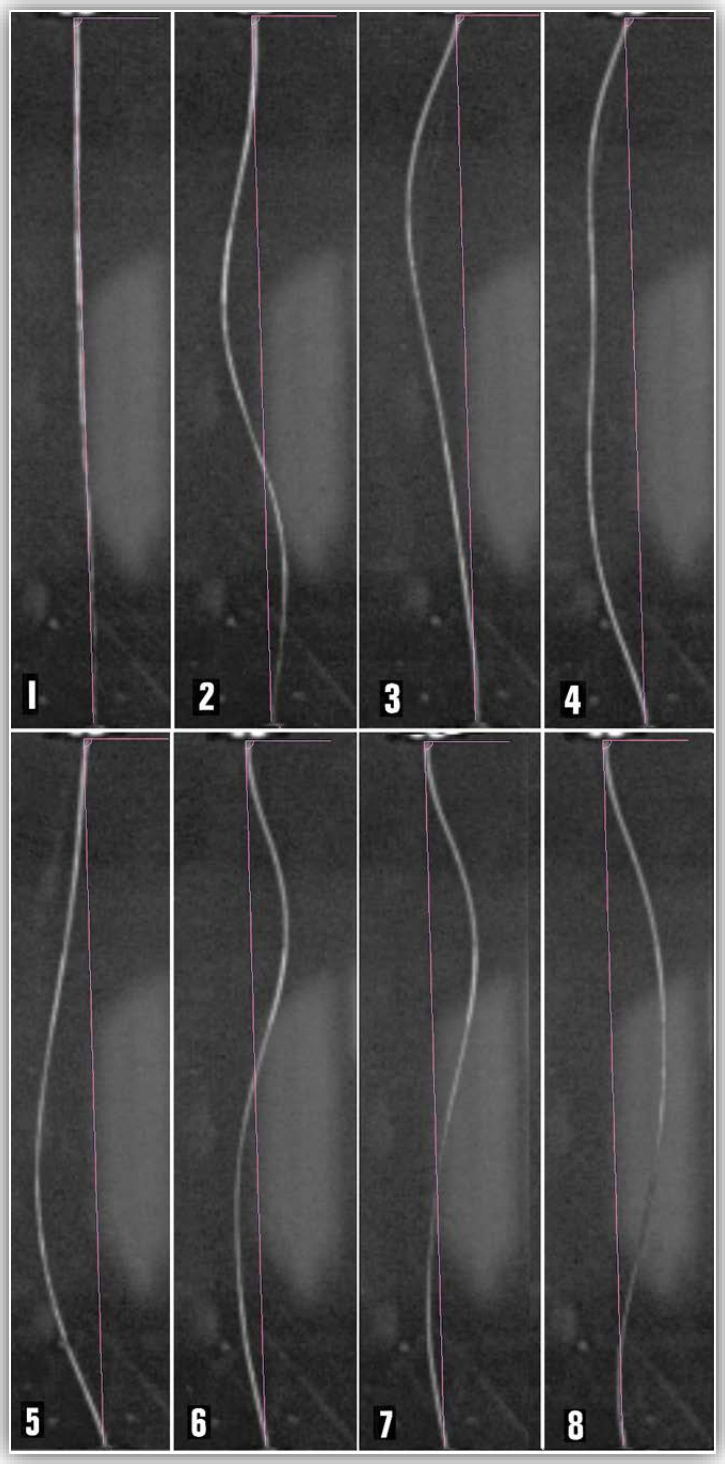

(K) The red line was placed as reference on the DICT program. (1) Shows the wire at $\tau = 0$s. (2–8) Flexural wave movement, second mode.

Figure 68. A_{21} element, third wire. Current vs. Time

D. COMPARISON WITH LUKYANOV AND MOLOKOV (2001)

In their study, Lukyanov and Molokov (2001) present qualitative and numerical analyses of their model. Several aspects of our results have been qualitatively compared with theirs. Lukyanov and Molokov's (2001) numerical analysis uses five different wires, all of them aluminum wires with a diameter of 1.2 mm. In what follows, we compare our results to the first two, which were 50 mm and 1,000 mm long. In each case, a current value of 5 kA was simulated.

Lukyanov and Molokov's (2001) numerical model yields a plot of the flexural displacement X, normalized to the length of the wire L as a function of position z, also normalized to the wire's length. Figure 69 shows this plot at the melting point temperature T_{Melt}. For the 50 mm wire, the graph shows the first mode with maximum displacement of 3 mm at z/L = 0.42, which they compare to "the form of being close to a simple arc, showing that the first mode dominates during the nonlinear stage" (p. 1550). Actually, their model predicted six modes, where only the first one was recognizable. If we compare this result to the A_{11} element, first wire, and third and fourth shots results of this thesis, they are very similar at both the X values and the shape of the wire at the maximum temperature. Also, they show the longitudinal and transverse stresses with respect to time. For this case, the major stresses appeared after 900 μs. In our case the time was around 1,200 μs.

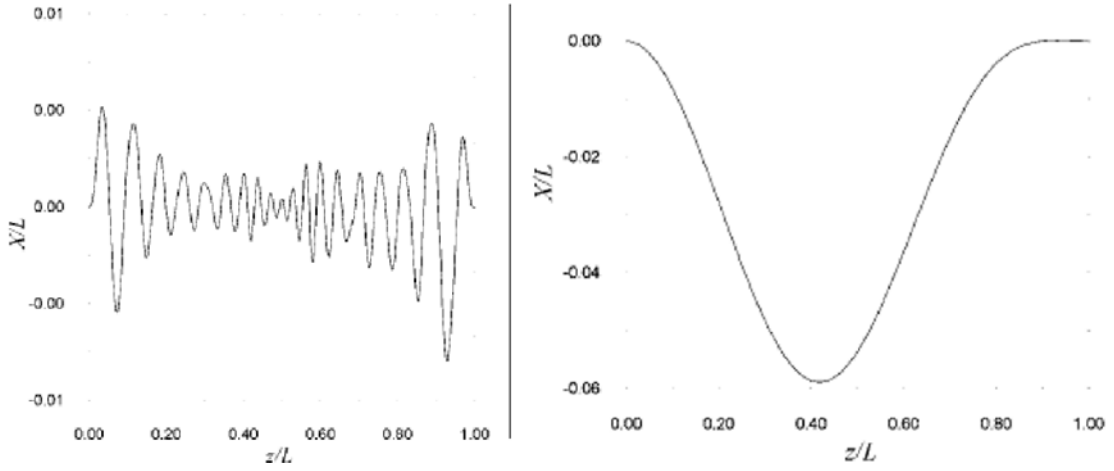

Figure 69. X/L vs. z/L for a 1 m and 50 mm long wire.
Source: Lukyanov and Molokov (2001)

On the other hand, the authors started their analysis of the 1 meter long wire by saying that the instability spectrum of the wave motion would have more modes than the previous one. In fact, we were able to see higher frequency modes developing, though our wire length was only one-fourth of theirs. This is why it was so difficult for us to spot other modes different from the first and second. Their model predicted X displacements of X/L = 0.007, while our higher result gave X displacements of 0.057 for a wire that did not break. They also predicted that the fragmentation would begin no further than 1 millisecond after the discharge, but what we got was multiple fragmentation beginning after 1.2 milliseconds. Furthermore, we also observed single fragmentation after more than 40 milliseconds.

From Lukyanov and Molokov's (2001) conclusions, we can comment on the following:

- They proposed the idea that flexural vibrations on a wire could be excited as a consequence of buckling instability. These buckling instabilities are directly related to thermal expansion due to joule heating and, to a small degree, due to electromagnetic forces that appear because of the wire's deformations. As we saw in our results, thermal expansion can increase significantly depending on the current and can lead to strong buckling phenomenon. Yet, even if the current is not high enough, buckling can still take place. On the other hand, we have not enough evidence to make any affirmation with regard to the electromagnetic forces contribution. Nevertheless, it has been seen that the wire's shape with respect to the z-axis can cause significant changes in the wave modes developed.

- Lukyanov and Molokov (2001) mention that "the energy accumulated in the wire during the initial stage [before the buckling] in the form of a compressive stress is suddenly released" (p. 1551). After this, high tensile stresses would appear in the wire causing it to break. In this thesis, we have seen repeatedly how the energy accumulated in the wires was released in the form of waves. Also, during the fourth shot of the A_{21}

element, it was possible to observe how the rupture of the wire caused a whiplash, which may be evidence of high stresses accumulated along the wire.

- Another point underlined by the authors is the fact that bending in the wires before the shot would cause the amplification of the modes that are already present on the wire's curvature. This effect could be the reason why the third wire, which was very straight along its axis, did not break, even if the discharge was higher than that of the first wire, fourth shot, and almost equal to the second wire's third shot.

THIS PAGE INTENTIONALLY LEFT BLANK

VI. CONCLUSIONS AND RECOMMENDATIONS

A. SUMMARY

The main objective of this thesis was to contribute to the ongoing debate about the existence of Ampère's longitudinal forces. To accomplish our objective, we developed an experimental approach to search for empirical evidence to explain the phenomena of wire fragmentation and explosion.

Our results seem to match, in many aspects, Lukyanov and Molokov's (2001) numerical model, which proposed an explanation for wire fragmentation and explosions apart from Ampere's longitudinal forces. Through mainly thermal expansion effects, those authors simulate the formation of the flexural deformations. From our data, we were able to calculate the values of thermal expansion they used in their model, and match them with the samples obtained in the laboratory.

The recent developments in high-speed digital videography enabled us to observe the evolution of the wire mechanical response as a result of large pulsed currents. In addition to the latest high-speed video camera technology of the Phantom model 2511, this experiment was only made possible by the unique apparatus known as the High Current Test Fixture and its symmetric electromagnetic design.

In what appears to be the first use of high-speed video capturing, we observed flexural modes predicted by Lukyanov and Molokov (2001). The study also predicted, depending on the wire's length and current, the number of modes and the tendency of predominance of the modes. Also, it predicted the shape that the wire would adopt and the time for the first rupture. Overall, not only the values obtained during the experimentation were comparable in many aspects to those of the model, but also the qualitative analysis of the number of modes, and behavior of the flexural deformation was consistent with Lukyanov and Molokov (2001). Therefore, the results of this thesis can be used as the first empirical evidence of the wire fragmentation phenomenon due to flexural waves on a wire with "clamped ends."

Another interesting result was the observation of a wire fragmenting after the current pulse ended. This seems to indicate that only the flexural waves, along with the joule heating, would be responsible for the rupture. The same fact was observed after the first rupture on a wire explosion with subsequent multiple fragments. In this case, some of the pieces had melting and plasma evidence on them, while others presented mostly mechanical rupture signatures. This may indicate that, at a certain point during the fragmentation process, some of the pieces broke in the absence of current.

B. FUTURE WORK

The relatively sparse data results of this thesis invite further experimentation in order to develop a large statistical sample from which more robust quantitative comparison with theory can be made. For example, additional experimental designs could investigate various metal alloys with different thermal expansion coefficients and resistivities. Wire diameter could be another important variable to study for further insight into the possible effects of current diffusion or mechanical tensile strength. Also, the temperature analysis can be improved by including the variable temperature coefficient of resistance values of the metal, which in our case was assumed constant, in order to predict the exact resistivity and temperature profiles.

An important aspect to pursue is that of varying boundary conditions of having free ends or mixed free-clamped boundaries. This is a challenging experimental setup since any arcing could result in high plasma pressure, affecting the resulting mechanical response of the wire.

Besides the novel use of high-speed video camera to capture and process the mechanical displacement data, the use of other sensors needs to be considered. These may include high-speed infrared camera technology, strain gauges to measure thermally induced stresses, magnetometers to probe the magnetic field around the wire and determine magnetic forces due to bending and deformation, and thermocouples or similar sensors to determine the temperature profile along the wire. The main challenge here is finding transducers that are insensitive to the electromagnetic interference of pulsed current testing.

Further analysis using COMSOL Multiphysics can augment the exploration. In particular, modifying the partial differential equations (PDE) to include Ampère's longitudinal force should be explored.

THIS PAGE INTENTIONALLY LEFT BLANK

APPENDIX A. AMPÈRE'S LAW DERIVATION

In this appendix, two topics related to Ampère's Law are discussed. The first one is the transformation of the Ampère's Law equation (originally written in electrodynamic system of units), recalling Equation (1) from this work, into the International System of Units form that is in use nowadays. Then, some trigonometrical relations associated with Ampère's force law are derived.

A. AMPÈRE'S LAW FROM ELECTRODYNAMIC SYSTEM TO SI SYSTEM

Consider two point charges, q and q' separated by a distance r from each other. Also, following Ampère's convention, consider attractive forces as positive and repulsive forces as negative. The electrostatic force between the previously mentioned particles is proportional to (Assis & Chaib, 2015):

$$-\frac{qq\prime}{r^2}. \tag{26}$$

Assis and Chaib explain that it is possible to write this equation in terms of equalities by representing it using a dimensionless constant. In this case

$$f = -\frac{qq\prime}{r^2}. \tag{27}$$

Using the International System of Units and vector notation, Equation (4) can be written as

$$\vec{F} = k_e \frac{QQ\prime}{r^2}\hat{r}, \tag{28}$$

where

$$k_e = \frac{1}{4\pi\epsilon_0}. \tag{29}$$

In Equation (28), $\vec{F}$ is the value of the Coulomb force that Q' exerts on Q. Otherwise, the value of $\vec{F}$ would be negative. Also, $\epsilon_0 = 8.85 \times 10^{-12}\ A^2 s^2 N^{-1} m^{-2}$ is a constant called vacuum permittivity.

At this point, applying the same method, it is possible to use an arbitrary dimensionless constant, in this case d^2f, to represent the original Ampère's force law (1) as

$$d^2f = \frac{ii\prime dsds\prime}{r^n}[\cos\varepsilon + h\cos\theta\cos\theta']. \tag{30}$$

On the other hand, as we saw in Equation (3), Ampère's law written in SI units and vector notation, where the current element $I_1\overrightarrow{dl_1}$ exerts the force on the current element $I_2\overrightarrow{dl_2}$, is given by

$$d^2\vec{F}_{Amp} = \frac{\mu_0 I_1 I_2}{4\pi r_{12}^2}[3\left(\overrightarrow{dl_1}.\hat{r}_{12}\right)\left(\overrightarrow{dl_2}.\hat{r}_{12}\right) - 2\left(\overrightarrow{dl_1}.\overrightarrow{dl_2}\right)]\hat{r}_{12}. \tag{31}$$

The following relations, described in Section B of this appendix, based on geometrical analysis, are given by

$$\overrightarrow{dl_1}.\overrightarrow{dl_2} = dsds'\cos\varepsilon, \tag{32}$$

$$\overrightarrow{dl_2}.\hat{r}_{12} = ds\cos\theta, \tag{33}$$

and

$$\overrightarrow{dl_1}.\hat{r}_{12} = ds'\cos\theta'. \tag{34}$$

Applying Equations (32), (33), and (34) into Equation (30):

$$d^2\vec{F}_{Amp} = -\frac{\mu_0 I_1 I_2 dsds\prime}{4\pi r_{12}^2}[2\cos\varepsilon - 3\cos\theta\cos\theta']\hat{r}_{12}. \tag{35}$$

At this point, it is possible to compare Equation (30) with Equation (35) just by remembering that $h = -\frac{3}{2}$.

After this analysis, it is possible to say that Ampère's force as he articulated it in his early work, can be expressed in terms of the International System of Units just by applying the following relation:

$$ii' \leftrightarrow \frac{\mu_0}{2\pi} I_1 I_2. \tag{36}$$

B. AMPÈRE'S LAW RELATIONS

Assis (1994) shows that in order to obtain Equations (32) and (33), you can take two current elements, ds and ds', from two different closed circuits C and C', respectively, as shown in Figure 70. The distance between both current elements is called r. The distance between a fixed origin A on a circuit C and the current element ids is called s. While the distance between A' and $i'ds'$ is called s'.

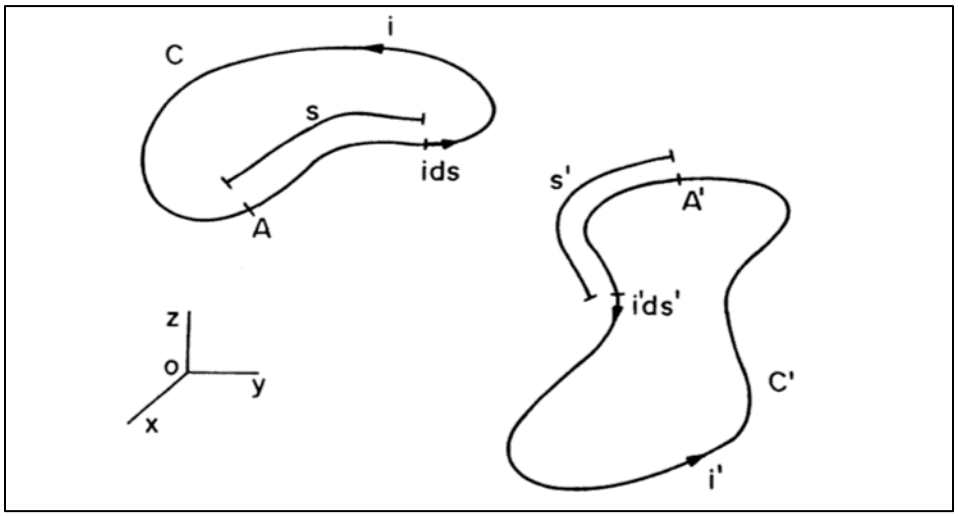

Figure 70. Two different current circuits. Source: Assis (1994).

Adopting a rectangular coordinate system, it is possible to locate both ids and $i'ds'$ with respect to the origin O, by giving them the coordinates x, y, z and x', y', z', respectively. From there it is possible to write that

$$\vec{r} = (x' - x)\hat{x} + (y' - y)\hat{y} + (z' - z)\hat{z}. \qquad (37)$$

It follows that assuming, as shown in Figure 71, he angle between $d\vec{s}$ and $\vec{r}$ is θ, the angle between $d\vec{s}\,'$ and $\vec{r}$ is $\pi - \theta'$, and the angle between $d\vec{s}$ and $d\vec{s}'$ is called ε. The scalar multiplication between vectors will be as shown in Equations (38), (39), and (40).

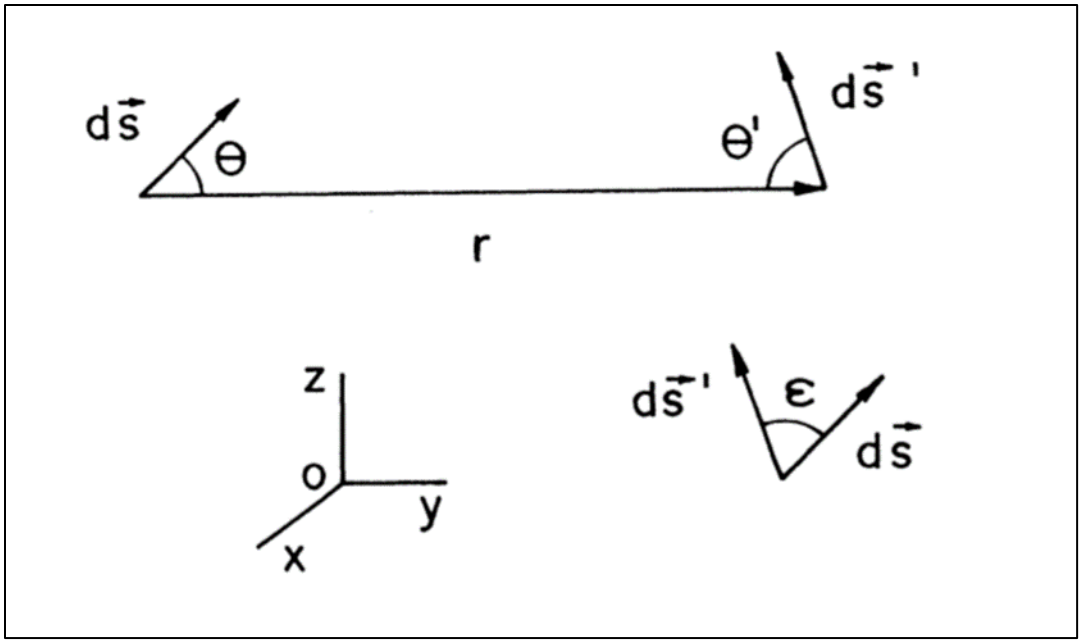

Figure 71. Angles between the current element $d\vec{s}$ and $d\vec{s}\,'$ and the vector $\vec{r}$, and the angle between both current elements. Source: Assis (1994).

$$\vec{r}.d\vec{s} = rds\cos\theta, \tag{38}$$

$$\vec{r}.d\vec{s}' = rds'\cos\theta', \tag{39}$$

and

$$d\vec{s}.d\vec{s}' = dsds'\cos\varepsilon. \tag{40}$$

In this way, the relations in Equations (11) to (13) are proven.

APPENDIX B. GRASSMANN'S FORCE LAW DERIVATION

It is possible to derive Grassmann's force law expressed in Equation (5) using two of the most important equations in electromagnetism: Lorentz's force equation (sometimes called Laplace force) and the law of Biot-Savart, given in Equations (41) and (42), respectively.

$$F = qE + qv \times B \tag{41}$$

$$dH = \frac{I_1}{4\pi}\frac{dl_1 \times \hat{r}_{12}}{r_{12}^2} \tag{42}$$

Equation (41) represents a charge q moving inside both, a magnetic field (B) and an electric field (E) with a velocity v. Lorentz used Grassmann's force law to derive the magnetic portion of his force formula, substituting qv for Idl in Equation (5) (Assis, 1994). It is then possible to, dropping the electric field part of the formula, rewrite Equation (41) as

$$F = Idl \times B. \tag{43}$$

On the other hand, Equation (42) describes the contribution that a current element (the infinitesimal part of a conductor carrying current I_1) has on a magnetic field at a certain point located at a distance r, being $\hat{r}$ the unit vector from the current element to the magnetic field point dH. This is a fundamental physics law in the field of the magnetostatics. Considering the following relationship from the magnetic field theory,

$$\mu_0 H = B, \tag{44}$$

and substituting Equations (42) and (44) into Equation (43), it will finally derive that

$$dF = Idl \times \frac{\mu_0 I_1}{4\pi}\frac{dl_1 \times \hat{r}_{12}}{r_{12}^2} = \frac{\mu_0 I_1 I_2}{4\pi r_{12}^2}\left[d\overrightarrow{l_2} \times \left(d\overrightarrow{l_1} \times \hat{r}_{12}\right)\right], \tag{45}$$

which is Grassmann's force law.

THIS PAGE INTENTIONALLY LEFT BLANK

LIST OF REFERENCES

Allen, J. E. (1990). The motionally induced back-EMF in railguns. *Physics Letters A, 150*(3), 151–152.

Allen, J. E., Wall, D., & Molokov, S. (2003). The fragmentation of wires by pulsed currents: Beyond the first fracture. *Journal of Physics Letters D,36, 2*757–2766. https://doi.org/10.1088/0022-3727/36/22/001

Ampère, A. (1826). *Theory of electrodynamic phenomena, uniquely deduced from experience*. Paris: Mequinon-Marvis.

Assis, A., & Chaib, J. (2015) *Ampère's electrodynamics: Analysis of the meaning and evolution of Ampère's force between current elements, together with a complete translation of his masterpiece: Theory of electrodynamic phenomena, uniquely deduced from experience.* Montreal: Apeiron Montreal.

Assis, A.K. (1994). *Weber's electrodynamics*. Campinas, Brazil: Kluwer Academic Publishers.

Blondel, C., & Wolff, B. (2009a, May). Ampère's force law: An obsolete formula? Retrieved from http://www.ampere.cnrs.fr/histoire/parcours-historique/lois-courants/force-obsolete/eng

Blondel, C., & Wolff, B. (2009b, May). In search of a Newtonian law of electrodynamics (1820–1826). Retrieved from http://www.ampere.cnrs.fr/parcourspedagogique/zoom/courant/formule/index-en.php

Brandes, E., & Brook, G. (1998). *Smithells light metals handbook*. Oxford: Reed Educational and Professional Publishing Ltd.

Cavalleri, G. (1996). The Ampère and Biot–Savart force laws. *European Journal of Physics, 17,* 205–207. https://doi.org/10.1088/0143-0807/17/4/010

Christodoulides, C. (1987). Are longitudinal forces predicted in magnetostatics by the Ampère force law in its line-current-element form? *Physics Letters A, 120*(3), 129–130.

COMSOL. (2015a). *The AC/DC module user's guide.* Stockholm, Sweden.

COMSOL. (2015b). *The COMSOL Multiphysics user's guide.* Stockholm, Sweden.

COMSOL. (2015c). *The heat transfer module user's guide.* Stockholm, Sweden.

COMSOL. (2015d). *The structural mechanics module user's guide.* Stockholm, Sweden.

Cornille, P. (1989). On the difference between the Lorentz and Ampère force laws in magnetostatics. *Journal of Physics A, 22,* 4075–4081. https://doi.org/10.1088/0305-4470/22/18/038

Graneau, P. (1984a). Ampère tension in electric conductors. *IEEE Transactions on Magnetics, 20,* 444–455.

Graneau, P. (1984b). Longitudinal magnet forces? *Journal of Applied Physics, 55*(3), 2598–2600. https://doi.org/10.1063/1.333247

Graneau, P. (1985). Comments on "Equivalence of the Lorentz and Ampere force laws in magnetostatics." *Journal of Applied Physics, 56*(9), 3638. https://doi.org/10.1063/1.335743

Graneau, P. (1987). Wire explosions. *Physics Letters A, 120*(2), 77–79.

Graneau, P. (1994) *Ampère-Neumann electrodynamics of metals.* Florida: Hadronic Press, Inc.

Graneau, N., & Graneau, P. (1996) *Newtonian electrodynamics.* Singapore: World Scientific Publishing Co. Pte. Ltd.

Hering, C. (1921). Revision of some of the electromagnetic laws. *J. Franklin Institute, 194,* 599–622.

Johansson, L. (1996). *Longitudinal electrodynamic forces and their possible technological applications* (Master's thesis). Retrieved from https://dflund.se/~snorkelf/LongitudinalMSc.pdf

Jonson, J. (2012). Ampère's law proved not to be compatible with Grassman's force law. In S.O. Bashir (Ed.), *Electromagnetic radiation* (pp. 53–78). https://www.intechopen.com/books/electromagnetic-radiation/amp-re-s-law-proved-not-to-be-compatible-with-grassmann-s-force-law

Lukyanov, A., & Molokov, S. (2001). Flexural vibrations induced in thin metal carrying high currents. *Journal of Physics D, 34,* 1543–1552. https://doi.org/10.1088/0022-3727/34/10/315

Maugin, G.A. (1988). *Non-Equilibrium thermodynamics of electromagnetic solids*. Berlin, Germany: Institute for Advanced Study.

McCormick, N. & Lord, J. (2010). Digital image correlation. *Material Today, 13*(12), 52–54. https://doi.org/10.1016/S1369-7021(10)70235-2

McDonald, K. (2016). *Ampère's hairpin spaceship*. New Jersey: Joseph Henry Laboratories, Princeton University.

Molokov, S., & Allen, J. (1997). The fragmentation of wires carrying electric current. *Journal of Physics D, 30,* 3131–3141. https://doi.org/10.1088/0022-3727/30/22/011

Moon, F.C. (1984). *Magneto-solid mechanics*. New York: Wiley.

Nasilowski, J. (1964). *Unduloids and striated disintegration of wires*. Exploding wires. New York: W. Chase.

Nicolaide, A. (2012). *Electromagnetics: General theory of the electromagnetic field. Classical and relativistic approaches.* Brasov, Romania: Transylvania University Press.

Papageorgiou, C., & Raptis, T. (2010). *Fragmentation of thin wires under high voltage pulses and bipolar fusion.* Athens, Greece: National Technical University of Athens.

Strnad, J. (1989a). On forms of the force law for current elements. *Physics Letters A, 137*(1, 2), 11–12. https://doi.org/10.1016/0375-9601(89)90960-2

Strnad, J. (1989b). Stefan's equations of electrodynamics. *European Journal of Physics, 10,* 276–280. https://doi.org/10.1088/0143-0807/10/4/006

Ternan, J. (1986). Stresses in rapidly heated wires. *Physics Letters A, 115*(5), 230–232. https://doi.org/10.1016/0375-9601(86)90472-X

Tricker, R. A. R. (1962). Ampère as a contemporary physicist. *Contemporary Physics*, 453–468, https://doi.org/10.1080/00107516208217501

Wall, D., Allen, J. E., Molokov, S., & Lukyanov, A. (2000, May). The fragmentation of wires due to pulsed currents: Influence of the skin effect. Paper presented at the IEEE Symposium on Pulsed Power 2000, London, UK.

Wesley, J. P. (1994). Pinch effect and Ampère tension to drive Hering's pump. *Foundation of Physics Letters, 7*(1), 95–104.

Whittaker, E. (1951). *History of the theories of aether and electricity, vol. II*. New York: Nelson.

THIS PAGE INTENTIONALLY LEFT BLANK

INITIAL DISTRIBUTION LIST

1. Defense Technical Information Center
   Ft. Belvoir, Virginia

2. Dudley Knox Library
   Naval Postgraduate School
   Monterey, California